NASA

Technical Memorandum 82013

On The Origin of Multiply-Impulsive Emission From Solar Flares

Judith Tobi Karpen

SEPTEMBER 1980

National Aeronautics and Space Administration

Goddard Space Flight Center
Greenbelt, Maryland 20771

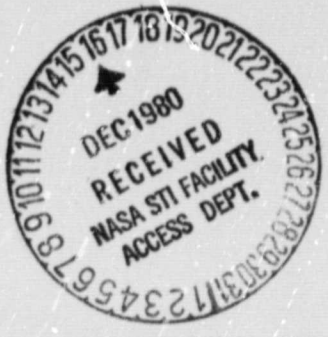

APPROVAL SHEET

Title of Thesis: On the Origin of Multiply-Impulsive Emission from Solar Flares

Name of Candidate: Judith Tobi Karpen
Doctor of Philosophy, 1980

Thesis and Abstract Approved: _____

Dr. Mukul R. Kundu
Professor and Acting Director
Astronomy Program

Date Approved: _____

CURRICULUM VITAE

Name: Judith Tobi Karpen

Permanent Address: 9 John Circle, Norwood, New Jersey

Degree and Date to be Conferred: Doctor of Philosophy, Astronomy, Fall 1980

Date of Birth: 1953 April 16

Place of Birth: New York City, New York

Secondary Education: Bright School for Girls, Englewood, N.J.

Collegiate Institutions Attended:	Dates	Degree	Date of Degree
University of Michigan	1970-1973	B.S.	12/73
University of Maryland	1974-1979	M.S.	5/79
University of Maryland	1979-1980	Ph.D.	12/80

Major: Solar Physics (Astronomy)

Positions Held:

Teaching Assistant	University of Maryland	1974-1975
Research Assistant	NASA/GSFC	1975-1980

Academic Honors: B.S. with Honors

Professional Societies: American Astronomical Society, Solar Physics Division

Publications:

"Coordinated X-ray, Optical, and Radio Observations of YZ Canis Minoris," J. T. Karpen et al., 1977, Astrophys. J., 216, 479. (26 co-authors not named). NASA TM X-682-76-287.

"Nucleosysthesis of Li7 in Flares on UV Ceti Stars," J. T. Karpen and S. P. Worden, 1979, Astron. Astrophys., 71, 92.

"Spectral Evolution of Multiply Impulsive Solar Bursts," J. T. Karpen, C. J. Crannell, and K. J. Frost, 1979, Ap. J., 234, 370.

"Dynamic Spectral Characteristics of Thermal Models for Solar Hard X-ray Bursts," J. C. Brown, I. J. D. Craig, and J. T. Karpen, 1980, Solar Phys., 67, 143..

"The Origin of Soft X-ray Emission in Impulsive Solar Flares," C. J. Crannell, J. T. Karpen, and R. J. Thomas, 1980, submitted to Solar Physics.

"The Role of Betatron Acceleration in Complex Solar Bursts," J. T. Karpen, 1980, submitted to Solar Physics.

ABSTRACTS:

"Coordinated X-ray, Optical and Radio Observations of YZ Canis Minoris," J. T. Karpen et al., 1976, Bull. Am. Phys. Soc., 21, 544.
Presented at the Spring Meeting of the American Physical Society, April 1976, Washington, D.C.

"Time Structures in Solar Hard X-ray and Microwave Spike Bursts," H. Wiehl, A. Magun, J. Karpen, C. Crannell, K. Frost, and C. Matzler, 1978, Bull. Am. Phys. Soc., 23, 508.
Presented by H. Wiehl at the Spring meeting of the American Physical Society, April 1978, Washington, D.C.

"Spectral Evolution of Multiply-Impulsive Solar Bursts," J. Karpen, C. Crannell, and K. Frost, 1978, Bull. A.A.S., 10, 455. Presented at the 152nd meeting of the American Astronomical Society, June 1978, Madison, WI.

"Applicability of Betatron Acceleration to Two-stage Hard X-ray Events," J. T. Karpen, K. J. Frost, and J. Brown, 1979, Bull. A.A.S., 11, 436. Presented at the 154th meeting of the American Astronomical Society, June 1979, Wellesley, MA.

"Origin of the Soft X-ray Emission from Impulsive Solar Flares," C. J. Crannell, J. T. Karpen, and R. J. Thomas, 1980, Bull. A.A.S., 12, 527. Presented at the 156th meeting of the American Astronomical Society, June 1980, College Park, MD.

TALKS

"Nucleosynthesis of Li^7 in Solar Flares," J. T. Karpen and S. P. Worden, presented at the Topical Conference on Solar and Interplanetary Physics, January 1977, Tucson, AZ.

"Hard X rays from Solar Flares," seminar given to solar physics group at the University of Maryland, April 1979.

ABSTRACT

Title of Thesis: On the Origin of Multiply-Impulsive Emission from Solar Flares

Judith Tobi Karpen, Doctor of Philosophy, 1980 (Astronomy)

Thesis directed by: Prof. Mukul R. Kundu, Acting Director, Astronomy Program; and Dr. Carol Jo Crannell, NASA-Goddard Space Flight Center.

Over the past twenty years, our understanding of solar flares has been augmented greatly by the advent of rocket-, balloon-, and satellite-borne instrumentation dedicated to observations of the Sun. In particular, the use of spacecraft-borne detectors has permitted long-term coverage of the shorter-wavelength regions of the electromagnetic spectrum, inaccessible to ground-based facilities. Hard X-ray emission from solar flares provides direct evidence of the role of energetic electrons in these powerful explosions. Analyses of flare-associated hard X rays, in conjunction with coincident coverage at other wavelengths, have contributed much of our current understanding of the fundamental energizing processes and resultant particle acceleration which characterize the flare phenomenon.

During the previous solar maximum, the hard X-ray burst spectrometer on board the OSO-5 satellite observed hundreds of hard X-ray events on the Sun, in the energy range 14 to 254 keV. The 1.8-second temporal resolution of the detector enabled detailed studies of the evolution of burst intensity with time, as well as the spectral evolution. Furthermore, the temporal resolution was comparable to that of most solar radio observatories

operating at that time, thus facilitating simultaneous intercomparisons of hard X-ray and radio data.

The analysis and interpretation of a set of complex hard X-ray bursts, selected from the OSO-5 data, are presented in this work. The multiply-impulsive events were chosen on the basis of morphological characteristics: each event appears to consist of a number of overlapping spikes, with no apparent gradual component of significance. The two-stage events were selected on the basis of both morphological characteristics and association with the appropriate phenomena at other wavelengths. Coincident microwave and meter-wave radio, soft X-ray, H-alpha, interplanetary particle, and magnetographic data were obtained from several observatories, to aid in developing a comprehensive and self-consistent picture of the physical processes underlying a complex burst.

The present research is focussed on three specific aspects of the multiple-spike and two-stage bursts:

1) To look for the causes of multiplicity in complex impulsive events;
2) To compare and contrast the physical mechanisms responsible for the multiple-spike bursts with those associated with their simple counterparts, the single-spike bursts (Crannell et al. 1978); and
3) To compare and contrast the impulsive emissions with associated gradual emissions, in order to pinpoint the basic processes which are applicable to the impulsive phase alone.

The investigation is concentrated on the hard X-ray and microwave emissions, with reference to associated meter-wave phenomena, where appropriate. The hard X-ray and microwave radiations are bremsstrahlung and gyrosynchrotron,

respectively, from the electrons accelerated in the relevant regions of the solar atmosphere. Together, they are used to deduce the characteristics of the source: electron density, temperature or spectral index of the electron distribution, magnetic-field strength, and area. The hard X-ray emissions alone are used to determine the parent electron spectrum and its evolution throughout an event, to search for correlated variations in spectral parameters which may indicate the underlying acceleration mechanism.

The main conclusions of this work are:

1) The multiplicity of the impulsive events studied requires at least two distinct causes. On the basis of derived source parameters, the bursts fall into two categories: events whose component spikes apparently originate in one location, and events in which groups of spikes appear to come from separate regions which flare sequentially.
2) The origin of multiplicity in the case of a single source region remains unidentified. Progress was made, however, in critical evaluation of postulated explanations. One hypothesis, which attributes intensity variations to betatron acceleration of electrons in a magnetic trap, was tested. It was found that purely impulsive emissions show no sign of betatron acceleration, thus ruling out this mechanism as a candidate for inducing multiply-spiked structure. The second-stage emissions of several complex bursts also were tested, with results differing markedly from the analysis of the impulsive bursts. The majority of the two-stage bursts exhibited spectral behaviour consistent with the betatron model, for the first few minutes of the second stage. Therefore, it appears that betatron acceleration not only is

conspicuously absent during the impulsive phase of solar bursts, but also may be an integral feature of the early stages of the second-stage acceleration, for many two-stage bursts.

ON THE ORIGIN OF MULTIPLY-IMPULSIVE EMISSION FROM SOLAR FLARES

by

Judith Tobi Karpen

Dissertation submitted to the Faculty of the Graduate School
of the University of Maryland
in partial fulfillment of the
requirements for the degree of
Doctor of Philosophy
in
Astronomy
1980

DEDICATION

To my ancestors:

אָמַר רַבִּי אֶלְעָזָר, אָמַר רַבִּי חֲנִינָא: תַּלְמִידֵי חֲכָמִים
מַרְבִּים שָׁלוֹם בָּעוֹלָם.

"Rabbi Elazar said, quoting Rabbi Ḫanina:
Scholars increase peace throughout the world..."

Babylonian Talmud,
Tractate Berakhot 64a

ACKNOWLEDGEMENTS

It is a great pleasure to thank Dr. Carol Jo Crannell for giving me the opportunity to enter the field of solar physics, and for helping to make that choice one which I have never regretted. The countless hours which she has devoted to discussing, verifying, pondering, debating, editing, and, last but not least, caring about my research, have been instrumental in my development as a solar physicist. I would also like to thank Dr. Mukul Kundu for accepting the unenviable task of being my main advisor at Maryland, and for providing pertinent guidance and valuable discussions on the complexities of solar physics, especially solar radio astronomy. The cogent comments and practical suggestions of Drs. Donat Wentzel and James Ionson have been invaluable in clarifying the theoretical aspects of this work, and in improving my understanding of the plasma processes fundamental to solar-flare phenomena. The time and effort expended by my entire committee in evaluating the physics and editing the text of this dissertation are greatly appreciated.

During my research, immense amounts of data were collected from many observatories throughout the world; I would like to thank those people who graciously complied with my sizeable requests for flare coverage, and provided the calibrations and explanations necessary for these data to be used correctly: A. Magun and H. Wiehl, Bern; R. Moore and H. Zirin, Big Bear; M. Beardon, Clark Lake; R. Stewart, Culgoora; A. Maxwell, Fort Davis; J. Harvey, Kitt Peak; R. Howard, Mt. Wilson; J. Castelli, D. Guidice, and G. Tarnstrom, Sagamore Hill (AFCRL); D. L. Croom and A. Wasik,

Slough; K. Ohki, Tokyo; S. Enome, Toyokawa; and H. Urbarz, Weissenau. G. Hurford, S. Kahler, and C. Matzler also are thanked for useful discussions on portions of the research presented in this thesis.

This research was supported by NASA grants NGL 21-002-033, NSG 7285, and NSG 033. I have also benefitted from participation in the Stanford SERF workshop, August 1980. A few examples of the observational results and theoretical suggestions which were discussed at that meeting have been mentioned in the final section (Coda) of this thesis, and are intended solely to serve as indications of "things to come".

The scientific advice and encouragement provided by the entire Solar Activity Branch at NASA-GSFC, especially by Kenneth Frost and Brian Dennis, have contributed greatly to my understanding of the OSO-5 satellite and hard X-ray analysis techniques, and of solar-flare research in general. I have benefitted also from the computer-programming expertise of Ed Cutler and Wendy Kennard (COMTECH), of Randy Barth (Code 603.2, GSFC), and of the relevant members of the Code 685 (GSFC) staff. I am grateful to the personnel of the Laboratory of Astronomy and Solar Physics at GSFC for welcoming me as a fledgling scientist and colleague. I also wish to thank the personnel of the Astronomy Program, especially Dr. John Trasco, for timely assistance when needed, and for enabling me to work at Goddard without major obstacles.

I salute my family and friends for tolerance, sympathy, and support throughout my seemingly-infinite career as a student. Most special thanks are due to Mikael Cameron Kevin Reardon (alias the Bear) for patience, encouragement, and more, on and off the courts.

CONTENTS

LIST OF TABLES

Chapter 1
INTRODUCTION

"He was allying himself to science, for what was science but the absence of prejudice backed by the presence of money?"
Henry James, The Golden Bowl

The Sun is the most powerful laboratory of astrophysics accessible to humankind. Physical processes within and on this nearest star are the subjects of fundamental fields of study, ranging from nuclear and elementary-particle physics to plasma physics. Although solar flares are mere perturbations in the total energy output of the Sun, affecting only a "skin-deep" layer of its surface, their complex and ill-understood nature encompasses a bewildering variety of physical mechanisms. Atomic interactions, hydrodynamic and magnetohydrodynamic effects, plasma- and electromagnetic-wave formation and propagation, and other basic processes all play crucial roles in the flare phenomenon.

In order to understand flare activity, a two-pronged approach is necessary. Flares must be observed over a wide range of the electromagnetic and particle-energy spectrum, to obtain the characteristic signatures of the underlying physical processes. This effort must be paralleled by theoretical research into those physical processes fundamental to the triggering and subsequent unfolding of flare activity, to provide models of flare phenomena which

consistently reproduce all the concurrently observed features.

It is difficult to define a "typical" flare, because some level of what could be denoted flare activity exists on the Sun at all times. Furthermore, individual solar flares differ enormously in their energy output and its detectable manifestations. The basic, common element is a rapid, transient heating of a confined portion of the solar chromosphere and corona. As much as 10^{16} g of highly-ionized plasma may be heated in less than a hundred seconds (Aust 1977). In many cases this disturbance extends downwards, to disrupt the photosphere, and upwards, to eject matter into interplanetary space. In all cases, however, it is clear that the primary explosion occurs in a magnetized, turbulent plasma, which evinces strong deviations from thermodynamic equilibrium. Flares essentially begin with reconnection among the magnetic-field lines found above sunspot groups. Through reconnection, the energy stored in the complex magnetic topology of the corona is liberated and transformed into bulk heating and mass motions of the local plasma. The sheared-field configuration in a coronal loop can result in a driven reconnection process, where multiple reconnections occur throughout the arch until saturation is reached (Spicer 1976,1977). The physics of the reconnection process and , in particular, the role of the plasma in which the interacting fields are imbedded are not fully understood at present. Laboratory experiments involving simulation of solar flare conditions have proven useful, but controversial, in this area (cf. Baum and Bratenahl 1976). The magnetic-field strengths and topologies, electron densities, and temperatures achieved during such experiments are not the same as those in solar flares, however, and it is unclear whether simple scaling laws are applicable. Intensive development also is in progress in the theory of

reconnection and related plasma interactions, with many exciting results. However, the dangers of oversimplification, often used to make a problem analytically or numerically tractable, must be recognized.

The energy imparted to the ambient medium through reconnection eventually manifests itself in a variety of detectable forms, including heating and mass ejections, visible in H-alpha and soft X rays; plasma waves, which can be transformed into radio waves; and particle acceleration, which is characterized by hard X-ray, EUV, microwave, and lower-frequency radio emission. The relative proportions of these flare products vary throughout each flare, as well as from flare to flare. Despite these differences, an idealized picture of a flare emerges from the myriad observations obtained over the century since the first identification of a solar flare (Carrington 1859; Hodgson 1859). On the basis of intensity profiles as a function of time, flare emissions can be classified as either "impulsive" or "gradual" (also "extended"). Impulsive emissions are characterized by rapid rise to, and fall from, maximum intensity, and often by spiky structure on even shorter time scales. Gradual/extended emissions, on the other hand, appear as they are named, with much slower rise and fall times and, usually, little or no internal structure on shorter time scales. Both or either of these kinds of emissions can be seen in a particular event. The distinctive features of both types of emission are illustrated by the hard X-ray burst of 1969 March 30, shown in Figure 1-1.

The significance of these two classes is more fundamental than mere morphology, however. The observed characteristics indicate basic differences between the physical circumstances resulting in impulsive radiations and

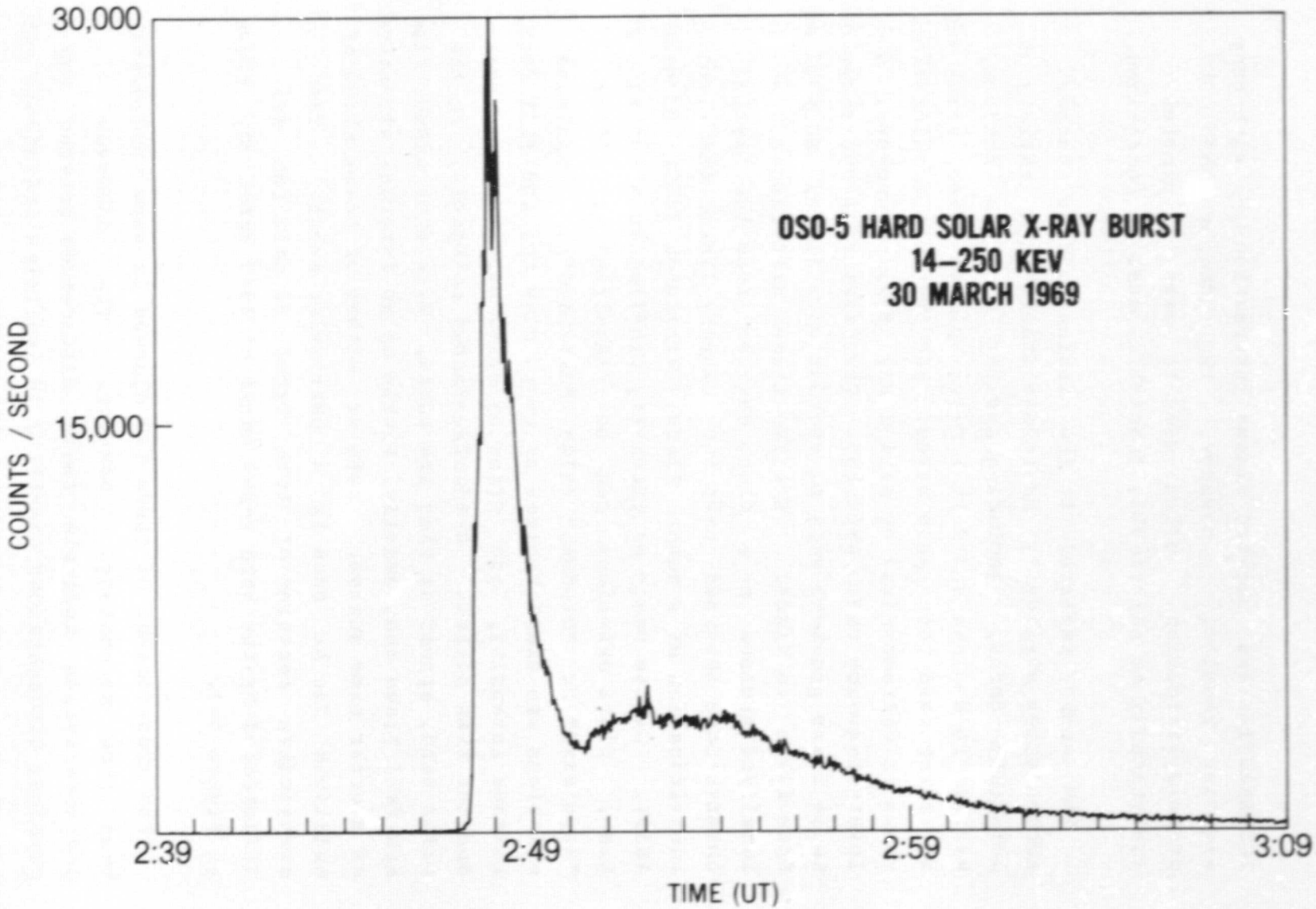

Figure 1-1. Hard X-ray time-intensity profile of the "classic" two-stage burst of 1969 March 30, summed over the energy range 14 - 254 keV.

those giving rise to gradual/extended emissions. Thus, flare activity often is classified into impulsive and gradual "phases". De Jager (1969) first identified impulsive emissions with a stage of rapid particle acceleration, and gradual emissions with a second stage of particle acceleration to even higher energies. The relationship between the observed radiation and the (inferred) particle energizing processes is discussed fully in Chapter 3 of this work. An introductory explanation is needed here, however: the association of hard X-ray and microwave radiation with flares strongly indicates the presence of energetic electrons, of energies greater than 10 keV, in flaring regions.

The short duration of the impulsive phase emissions implies a correspondingly rapid acceleration process, while the slower rise and fall of the gradual-phase emissions point to a physical mechanism of comparably longer duration. The rapid acceleration thus associated with the impulsive stage appears to affect mainly the electrons, raising their ambient energies from the order of 100 eV to between 10 and 100 keV. In some instances, the appearance of gradual emission after the impulsive stage merely indicates a simple heating of the post-flare plasma. This type of gradual phase usually is characterized by a microwave "gradual rise and fall" event, with no signs of associated particle acceleration. Other events, however, exhibit gradual emissions which are manifestations of second-stage acceleration processes. Observations of flare-associated interplanetary particle events indicate that, during the gradual phase of this type, protons and heavier ions are accelerated to energies in the MeV to GeV range, while the electrons achieve relativistic energies, of order 1 MeV. The identification and comprehensive theoretical modelling of the physics involved in these different particle-

acceleration processes are among the most outstanding challenges to solar physicists today.

The present work is devoted primarily to a study of the complex solar emissions, as observed in hard X rays, microwaves, and, to a lesser extent, other portions of the electromagnetic spectrum. These observations are used to construct a self-consistent picture of the physics of the impulsive and gradual stages. To avoid the dangers of overgeneralization and consequent vagueness, which can result easily from large-scale studies of the type described here, two specific approaches were chosen for in-depth investigation. These two topics are related by a common theme: the search for an explanation, or explanations, of the multiplicity in impulsive emissions, as manifested particularly in hard X-ray and associated microwave bursts. Hence, the first topic is concentrated directly on evaluating the evidence for separate flaring sites, within the same active region, being responsible for multiply-impulsive emissions. In the course of this research, it quickly became evident that, to comprehend the underlying processes affecting impulsive radiation, one must compare and contrast impulsive with non-impulsive emissions. The second study is focussed on other plausible explanations for multiplicity in impulsive bursts, and on the ramifications of these models of multiply-impulsive emissions for the non-impulsive phenomena closely associated with the impulsive stage. Brief summaries of the two major lines of attack on the questions posed above are incorporated into the following outline of the thesis organization.

This dissertation comprises six chapters: the Introduction; two chapters providing information on instrumental and data-analysis characteristics and relevant physical processes; two chapters wherein the research,

motivated as described above, is presented; and a final "Coda" which includes a summary of the results and new questions posed by the research presented here, together with suggestions for future investigations. Chapter 2 consists of a comprehensive description of the hard X-ray spectrometer flown on board the OSO-5 satellite, and a general outline of the methods by which the X-ray data were obtained from the spaceborne detector and the parameters were extracted for use in the present analyses. Those readers who are familiar with this information might wish to skip part or all of Chapter 2. The physics of the hard X-ray and microwave emission mechanisms which are relevant to solar flares is reviewed in Chapter 3, with particular emphasis on concepts and formulae which are used in the observational analyses and interpretations of the later chapters. The purpose of this chapter is to provide a comprehensive base for understanding the specific physical processes on which the present research is based, and to establish the scope of this work within the wider context of current solar-flare research. Chapter 3 may be read in full, selectively, or not at all, depending on one's familiarity with the material.

The analysis and interpretation of coincident hard X-ray and microwave evolution in a set of multiply-impulsive solar events is discussed in Chapter 4. This study resulted in the identification of two classes of multiple-spike bursts: events whose component spikes apparently originate in one location; and events in which groups of spikes appear to come from separate regions which flare sequentially. Thus, the multiplicity of impulsive emissions is explained for the latter type of events, but another mechanism is required to account for the multiply-spiked emissions which originate in a single source region. Chapter 5 is devoted to the critical evaluation of a promising candidate for explaining

burst multiplicity: the betatron acceleration of X-ray-emitting electrons in a magnetic trap, which was proposed originally by Brown and Hoyng (1975). The betatron model first was tested for consistency with the multiply-impulsive events; it was found that the betatron mechanism is conspicuously absent in the purely impulsive bursts, thus eliminating this process as a potential source of impulsive-phase multiplicity. However, the serendipitous inclusion of two two-stage events in the initially-selected set of multiply-impulsive bursts enabled the discovery that the betatron process apparently is associated, instead, with the second-stage emissions. The application of the betatron-acceleration model to several "classic" two-stage X-ray events, and related meter-wave emission, provided strong support for the identification of betatron acceleration as a common second-stage phenomenon. The final chapter is a summary of the cogent points of this thesis, and of the unsolved questions, raised by this work, which are in urgent need of further scrutiny, perhaps during the ongoing studies of the present solar maximum.

Chapter 2
THE INSTRUMENT

2.1 DESCRIPTION OF THE SATELLITE AND THE DETECTOR

The Fifth Orbiting Solar Observatory (OSO-5) was launched on 22 January 1969, at 16:48 GMT. The orbit was nearly circular (e = 0.002), with an apogee of 560 km, a perigee of 535 km, an inclination angle of 33°, and a period of 95.8 min. The satellite orbit was located well within the Earth's magnetosphere, and passed through portions of the inner trapped-particle belt.

The hard X-ray spectrometer on board OSO-5 occupied one of the nine experiment compartments in the rotating wheel of the spacecraft, as shown in Figure 2-1. The detector axis was perpendicular to the satellite spin axis, so that during each wheel rotation a strip of the sky in the plane of the wheel was scanned. Each of the three eyeblocks shown in Figure 2-1 contained 3 photodiodes, separated by 40°, which triggered upon viewing the Sun. This enabled each sky scan to be divided into 9 sectors of 40° each. Operations in the sector containing the Sun were denoted the solar mode, while data obtained in the remaining 8 sectors constituted the day sky scan. The observational format is discussed in detail in Section 2.2.

The detector has been described by Frost, Dennis, and Lencho (1971) and Dennis, Suri, and Frost (1973). It was designed to detect hard X rays from the full solar disk, with good time resolution and moderate energy resolution. Figure 2-2 shows a cross-sectional view of the instrument.

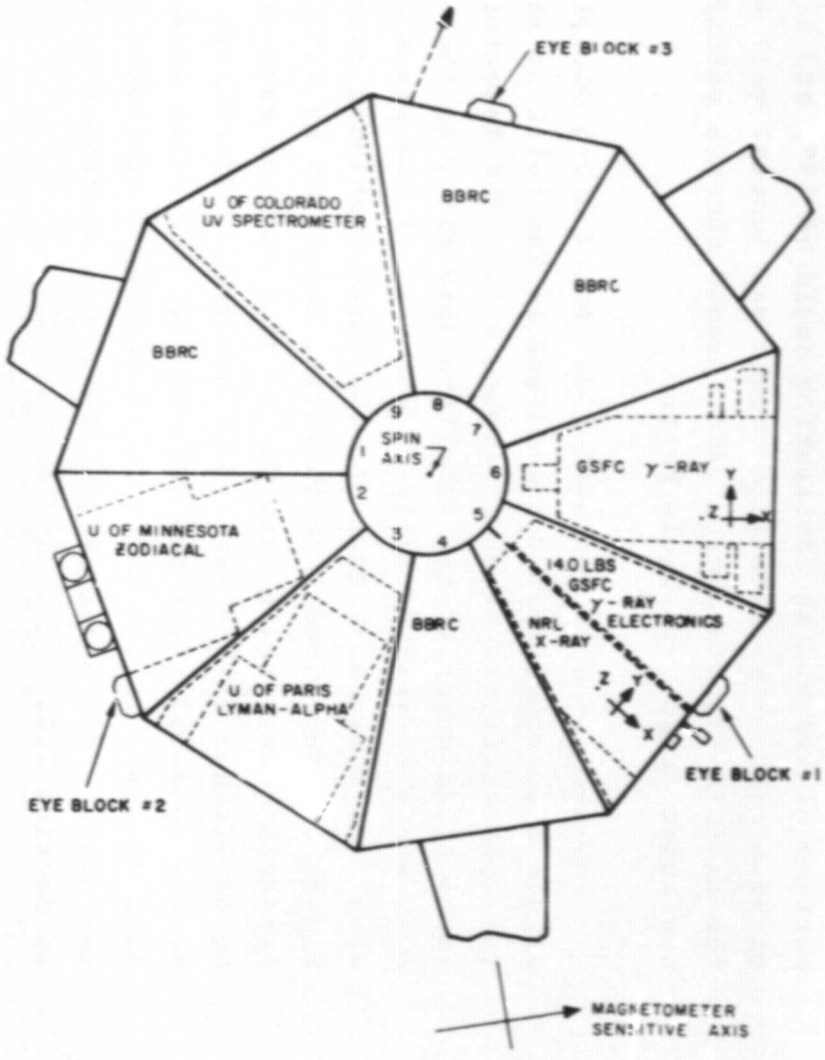

Figure 2-1. The configuration of the experiments located in the wheel compartment of the OSO-5 satellite.

OSO-5
15-250 KEV X-RAY DETECTOR

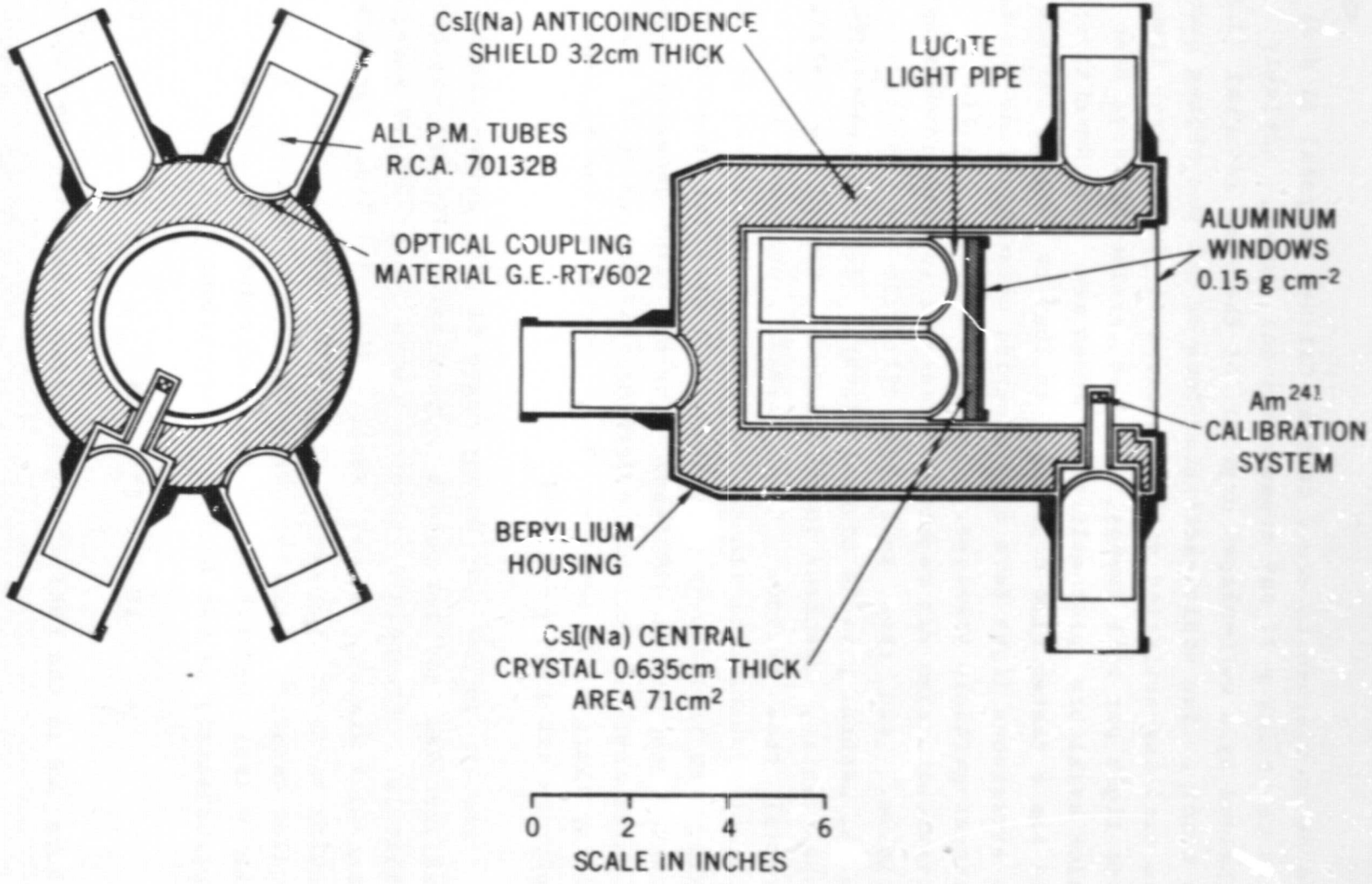

Figure 2-2. A cross-sectional view of the OSO-5 hard X-ray spectrometer.

The basic components are a central CsI(Na) crystal (a disk 0.64 cm thick x 71 cm² cross-sectional area), actively shielded by a well-shaped crystal of the same material (3.2 cm thick). The sodium-activated form of CsI was chosen over the thallium-activated variety because it yields three times more light per unit energy, in the wavelength range over which available photomultiplier tubes are most sensitive; and has a faster time constant, so that it is less subject to extraneous light from slow-decaying scintillations due to charged-particle passages. Sodium iodide (thallium-activated) also was rejected because it is deliquescent and brittle, and thus much more difficult to handle (B. R. Dennis, private communication). Two photomultiplier tubes (PMTs), operated in coincidence, viewed the central crystal from behind. The shield, operated in anticoincidence with the central element, was viewed by four PMTs, and included an aperture which gave the detector an angular response of 39° FWHM. The resultant geometric area x solid-angle factor ranged from 34 cm² sterad at the low-energy limit (~20 keV) to 47 cm² sterad at the highest energies attained (~250 keV).

The 14 to 254 keV energy range of the pulse-height analyzer was divided into 9 approximately linearly-spaced channels. Channels 2 through 9 were about 28 keV wide; Channel 1 was only 14 keV wide. Table 2-1 lists for each energy channel: the energy range, the mean energy, the scaler capacity, and the area-efficiency conversion factor. The energy resolution of the instrument is given approximately by the following expression:

$$\Delta E = 6\ E^{1/2}\ \text{keV} \quad , \qquad (1)$$

where ΔE is the FWHM of the Gaussian resolution function of

the detector for photons of energy E (Crannell et al. 1978).

TABLE 2-1

PARAMETERS FOR THE OSO-5 X-RAY SPECTROMETER

Channel Number	Energy Range (keV)	Mean Energy (keV)	Scaler Capacity	Conversion Factors* Pre	Post
1	14-28	22	4095	9.70E-02	3.71E-01
2	28-55	38	511	1.19E-03	1.31E-03
3	55-82	65	127	7.42E-04	7.42E-04
4	82-111	93	63	6.34E-04	6.34E-04
5	111-141	122	31	6.00E-04	6.00E-04
6	141-168	151	31	6.96E-04	6.96E-04
7	168-200	179	15	6.41E-04	6.41E-04
8	200-225	210	15	8.94E-04	8.94E-04
9	225-254	236	15	8.23E-04	8.23E-04

* These are the area-efficiency conversion factors for the periods pre- and post- 1969 October 26. They convert observed count rates per channel to incident flux in units of photons cm^{-2} s^{-1} keV^{-1}.

The idealized efficiency of the detector is plotted in Figure 2-3, after Frost, Dennis, and Lencho (1971). The sharp decrease in efficiency below 30 keV is due to absorption in the two aluminum windows, of total thickness 0.15 g cm^{-2}. The purpose of this relatively thick window was to attenuate the intense soft X-ray flux present during most solar bursts; without this attenuation, pulse pile-up could occur in the lowest channels during large flares, causing distortion of the measured hard X-ray spectrum. The actual efficiency is lower because of two additional effects: absorption in the dead layer which formed on the surface of the central CsI crystal (Crannell, Kurz, and Viehmann 1974; Goodman 1976); and the coincidence requirement on the two PMTs viewing the central crystal--photons below 30 keV do not necessarily produce a signal above threshold in both PMTs. The coincidence requirement reduced the background events produced by random

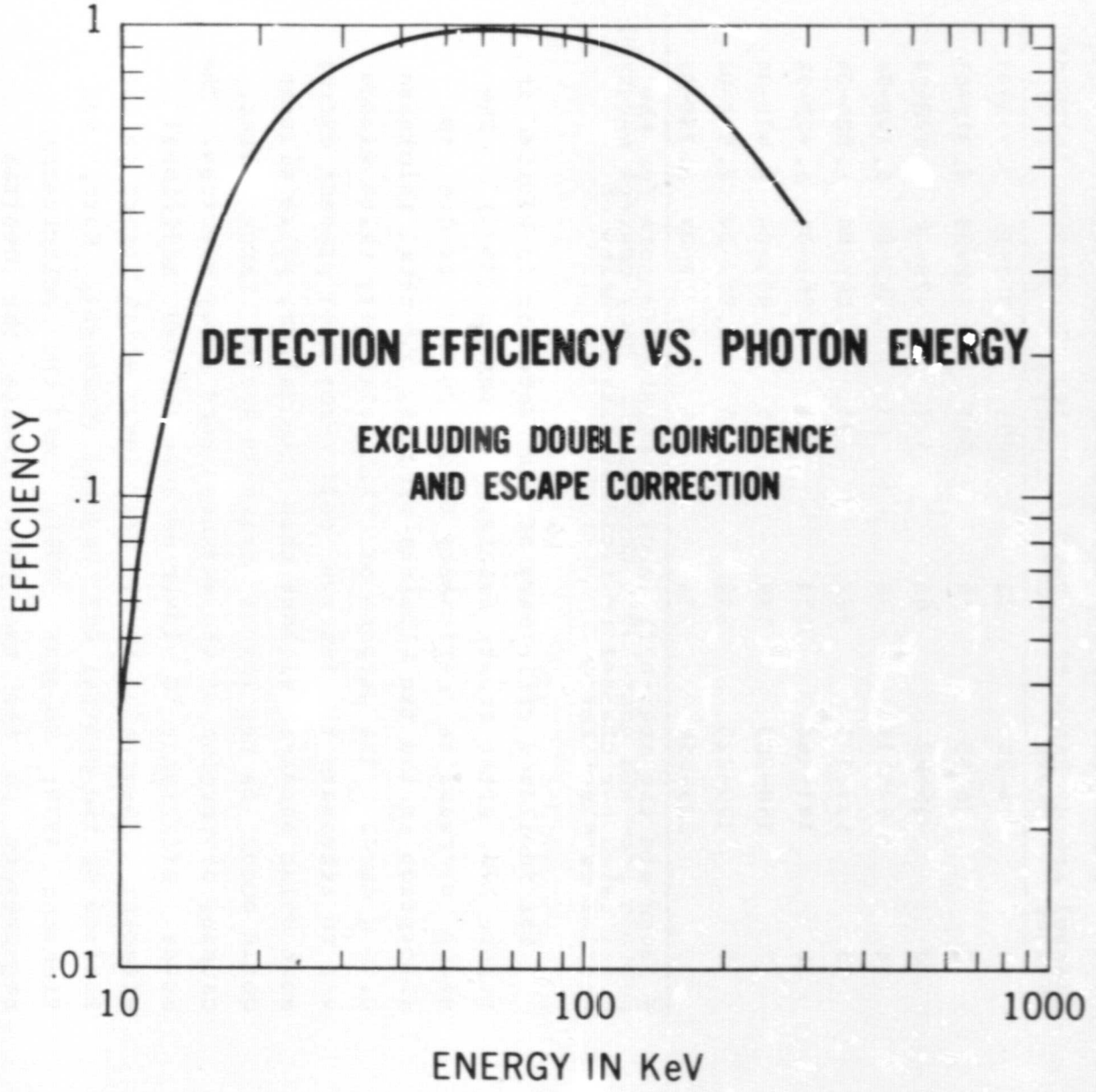

Figure 2-3. The efficiency of the OSO-5 hard X-ray detector, as a function of photon energy.

noise in the two PMTs, which generally is not in coincidence. Thus, X rays in channel 1 (14 to 28 keV) of the pulse-height analyzer were attenuated by a factor of approximately 15 (B. B. Dennis, private communication).

In-flight calibration of the energy scale of the instrument was achieved by using the decay products of an Am^{241} source, which was embedded in a piece of plastic scintillator and mounted in the aperture as shown in Figure 2-2. The Am^{241} decays by isotropic emission of 59.4-keV photons, some of which stop in the central crystal, in coincidence with 5.5-MeV alpha particles, which stop in the plastic scintillator and produce pulses in the PMT viewing the Am^{241}-activated scintillator. The calibration data thus obtained demonstrated that the gain decreased gradually by 20-30% between launch and 26 October 1969, requiring a one-increment change in the amplifier gain to maintain the constancy of the channel edges, and remained stable thereafter. The threshold level of the active shield was set at approximately 180 keV before launch and appeared to remain constant throughout the lifetime of the instrument, as indicated by the long-term stability of the shield counting rate and the total dead time.

The satellite passed through the South Atlantic Anomaly (SAA), a region of exceptionally high trapped-particle fluxes where the inner radiation belt intersects the satellite orbit, about 6 adjacent orbits per day. To prevent saturation and subsequent impairment of the PMTs, the high-voltage source was turned off during each passage through the SAA throughout the lifetime of the satellite. The background level of the detector was affected by passage through the South Atlantic Anomaly and by high-energy cosmic rays, both of which induced radioactivity in the central crystal and all the surrounding material, including the

shield. The background counting rate reached a peak immediately after each SAA passage and decayed exponentially, as the shorter-lived isotopes decayed, until the next passage through the SAA. The build-up of longer-lived isotopes, however, caused a gradual increase in the background rate superimposed on the regular orbital and daily variations. Over the lifetime of the satellite, the background rate changed by less than 10% in channels 2 and 3, and by less than a factor of 2 in channels 4 through 9 (B. R. Dennis, private communication).

The hard X-ray spectrometer operated continuously from launch until 1972 May. After this, data were collected sporadically, with partial coverage available for 1972 July. The instrument failed fatally sometime between 1974 August 9, 2319 UT, and August 10, 0549 UT. Because the failure occurred during a three-orbit gap in data coverage, the cause of failure could not be established firmly; failure of the high-voltage power supply was strongly suspected, however (B. R. Dennis and R. Thomas, internal GSFC memorandum).

2.2 DESCRIPTION OF DATA COLLECTION MODES

From launch until about 1969 January 28, the satellite operations were devoted to spacecraft checkout and no useful solar data were obtained.

The hard X-ray spectrometer viewed 360° strips of sky in each rotation of the wheel, approximately every 1.8 s. Each scan was divided into 9 sectors, as noted previously, one of which included the Sun. In the normal mode, the data comprised the number of counts in each channel, the elapsed time, and the instrument dead time; these times are defined below. Except during very intense flares, data were obtained in the solar sector for 0.17 to 0.19 s each

rotation, as determined by the photodiode pulses signalling the beginning and end of this sector. These pulses also determined the elapsed time of each solar observation, by starting and stopping a scaler which counted pulses from the 800-Hz telemetry clock. Thus, the elapsed time in seconds equalled the counted number of clock pulses divided by 800.

The true observing time, that is, the live time required to derive the rate of incident X rays from the observed counts, is the difference between the elapsed time, as defined above, and the total instrumental dead time. The dead time was measured during each solar observation with the aforementioned clock-pulse counter, which was gated by pulses in the shield and central crystal and by the busy signal of the pulse-height analyzer and related electronics.

During very intense flares, however, a different mode of data collection was utilized. If the counting rate were sufficiently intense to exceed the scaler capacity of any channel before the photodiode-signalled end of the solar observation period, then the accumulation of data and the clock-pulse counting were stopped when the scaler reached capacity (that is, earlier than the diode pulse). In this way the true count rate was recorded even during the largest events, instead of being lost due to scaler overflow.

Observations in the eight non-solar sectors differed from those in the solar mode only in that larger scaler limits and longer integration times were implemented, and the total count rates in both the shield and the central crystal were recorded. Data were accumulated for 6 wheel rotations in the sector immediately following the solar sector (denoted sector 1, in the clockwise direction when viewed along the positive spin axis of the wheel) and was followed by readout to a memory. This process was repeated

with data accumulation and readout for the next non-solar sector, while the previous sector's data were being transferred from the buffer memory to the spacecraft tape recorder. This sequence was implemented for the remaining non-solar sectors and repeated continuously throughout the day-time period of the satellite orbit. Each cycle also included a calibration procedure, in which the Am^{241} calibration data (cf. Section 2.1) were obtained for six rotations between sectors 6 and 7. A complete cycle lasted for 108 s, during which a total of 10.8 s of non-solar data were collected: 1.2 s for each of the 8 sectors and 1.2 s of calibration data.

During satellite night, when the spacecraft was in the Earth's shadow, yet another mode of data collection was used. The dead time and the nine-channel energy spectrum were accumulated for 0.28 s every 1.28 s, for whatever part of the sky happened to be in view. The region of the sky scanned during this period could be reconstructed from the spacecraft attitude, as determined from the magnetometer data obtained simultaneously.

2.3 TELEMETRY

The information stored in the spacecraft tape recorder was communicated to the Earth-based ground stations via the spacecraft telemetry system. Within the format of the telemetry data stream, each instrument on board OSO-5 was allotted specific words in the continuous data flow; the particulars of this arrangement relevant to the hard X-ray spectrometer are described in this section.

The transmission rate of the OSO-5 telemetry was 800 bits per second. The data were telemetered in 8-bit words and organized within main frames and major frames. A main frame consisted of data in a 32-word (320 ms) readout cycle; 128

main frames (40.96 s) comprised a major frame. Within each main frame, words 16,18, and 19 were devoted to the hard X-ray spectrometer. The order in which data were inserted into the 3 words per main frame is shown in Figure 2-4. Since 12 words were required to include all solar-sector data in each readout cycle, transmission of each observation (i.e., per wheel rotation) took 4 main frames (1.28 s). The information contained in these 12 words was commonly referred to as the "main frame data." The non-solar sector and shield data were transmitted at a slower rate: word 29 (in a main frame) was devoted to these data once every few main frames. This procedure was referred to as "submultiplexing" or "subcommutating" the data. The digital submultiplex word usage and locations within the major frame (DSM number) are shown schematically in Figure 2-5.

Figure 2-6 is a representation of the data organized within each major frame, showing the designated words filled by the hard X-ray spectrometer data. The data telemetered in this fashion were relayed by the various ground stations to the Information Processing Division (IPD) at Goddard Space Flight Center (GSFC). In the next section, the storage of this information on magnetic tape and subsequent data processing are discussed.

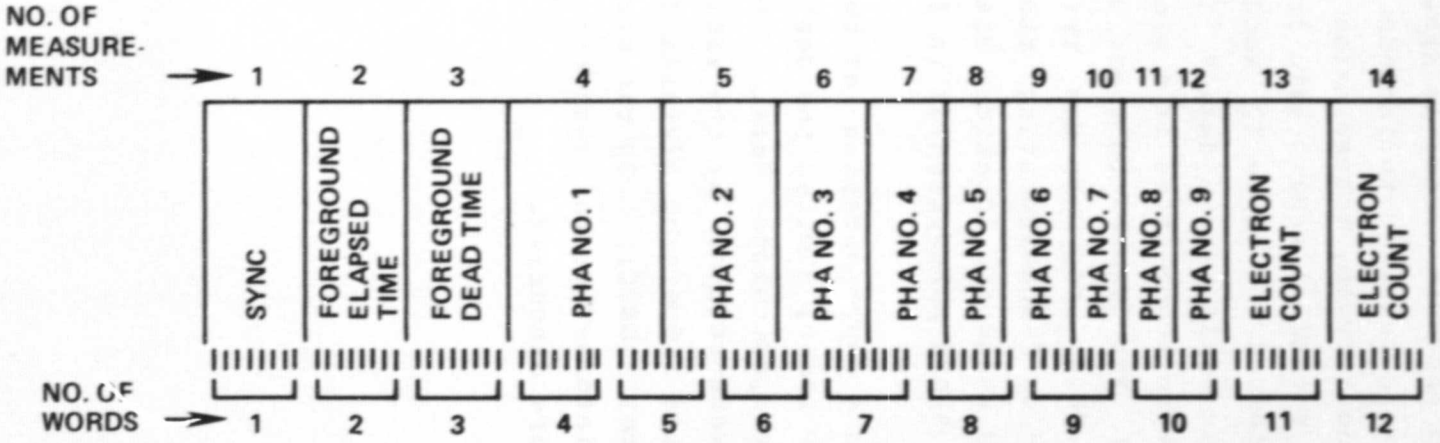

Figure 2-4. The components of a main frame of telemetered data.

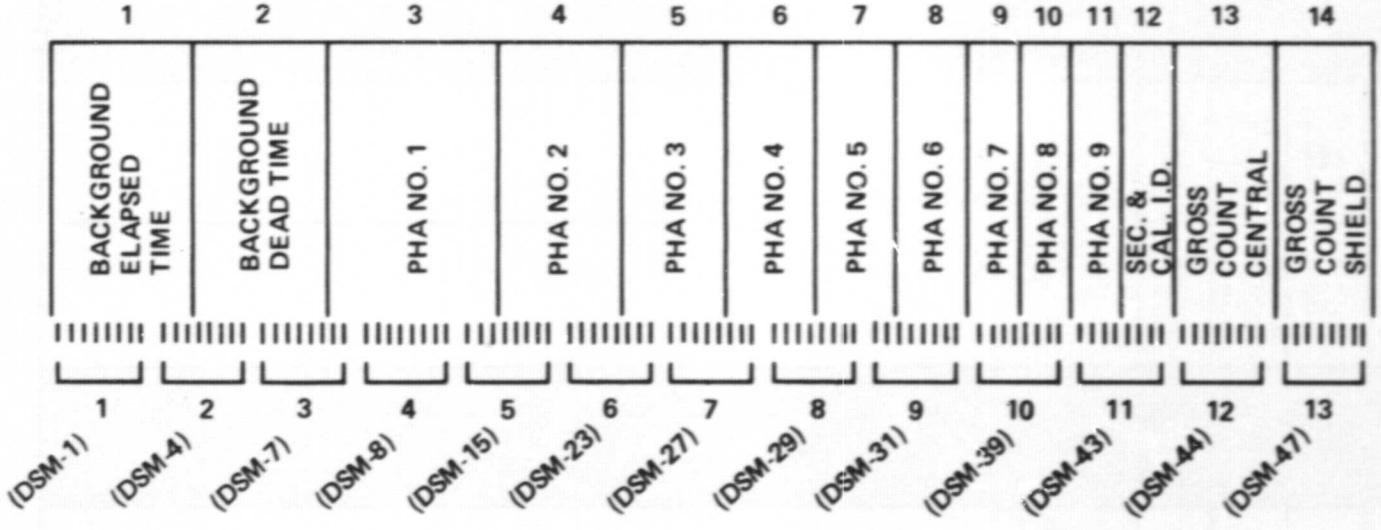

Figure 2-5. The word usage comprising the digital submultiplex (DSM) data. The DSM number denotes location within a major frame (see Fig.2-6).

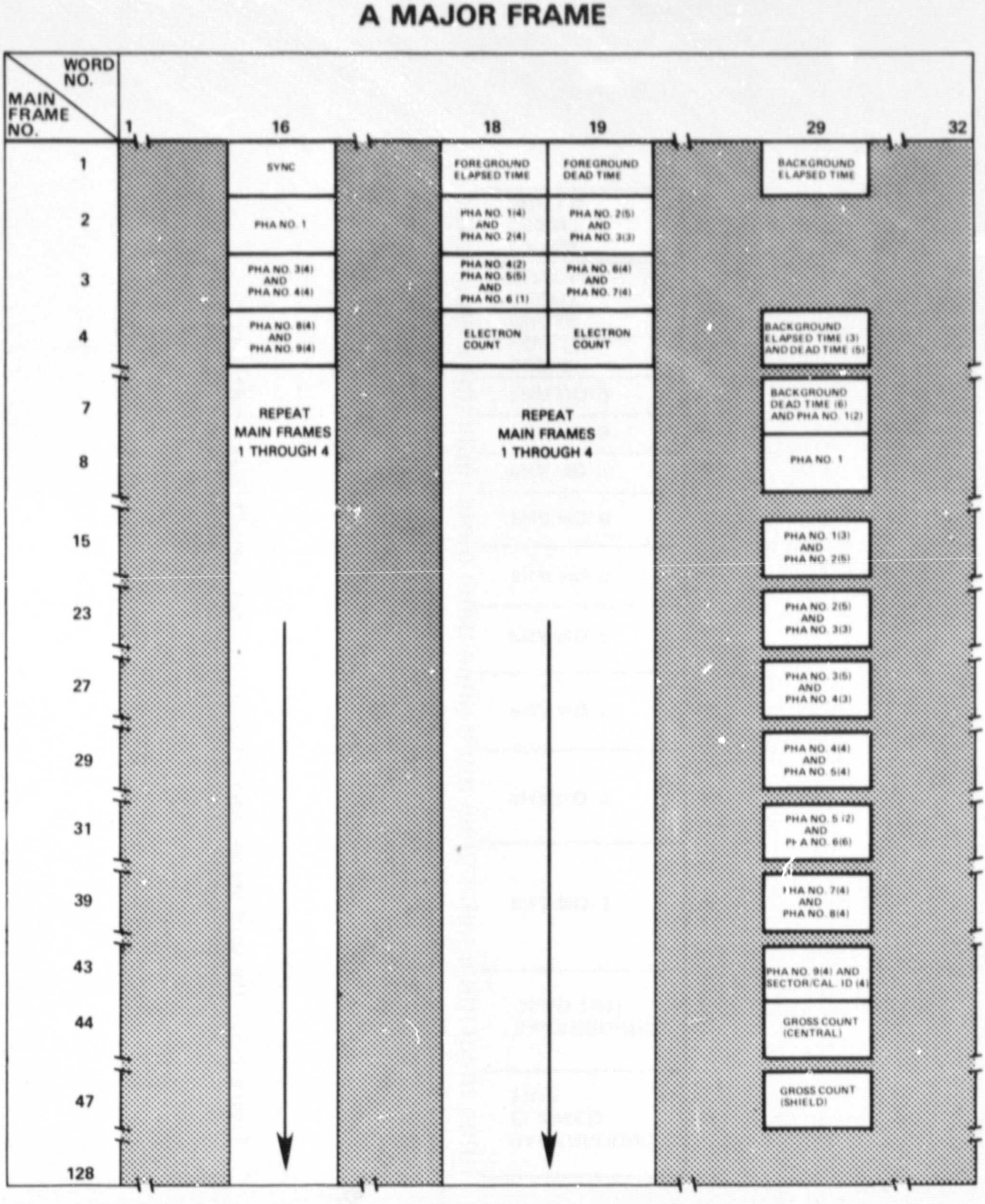

Figure 2-6. A representation of the locations of OSO-5 data words within a major frame of telemetered data.

2.4 DATA PROCESSING

The telemetered OSO-5 data were recorded on 7-track digital magnetic tapes in binary mode, with odd parity and at a density of 800 BPI. Two types of tapes were generated by IPD at GSFC, under the direction of Mr. John Schmidt, for distribution to the experimenters: Main Frame Data (MFD) and Correlated Data (CD) tapes. The MFD tapes contained main frame data, including the raw observed counts, elapsed time, and dead time. The corresponding CD tapes contained information on the satellite attitude, observed counts in the non-solar sectors (subcommutator data), and records of any commands issued to the instrument.

By means of software developed by Mrs. A. Andersen, GSFC, both sets of tapes were combined into a single set of 9-track tapes. Dr. Brian Dennis then processed the information on these intermediate tapes to construct "encylopedia" tapes, which contained all necessary instrument data plus the instrument orientation, as calculated from the satellite aspect data. A set of compressed encyclopedia tapes was made by COMTECH, Inc., in which the format of the original encyclopedia tapes was reorganized to reduce the total number of tapes required by about a factor of 4. Programs written by COMTECH, Inc. use the relevant satellite and instrument information on these tapes to obtain the flux observed in all 9 channels at a given time, in physically useful units (i.e., photons cm^{-2} s^{-1} kev^{-1}). Thus, spectra can be generated for time intervals as short as 0.18 s every 1.8 s, or averaged over longer times, to improve statistics or to obtain a measure of the hard X-ray background before or after a flare.

Chapter 3
PHYSICS OF HARD X-RAY AND MICROWAVE EMISSION

The first observation of hard X rays from the Sun was reported over twenty years ago by Peterson and Winckler (1958,1959). In these papers, the authors interpret the flare-associated X radiation as bremsstrahlung produced in the solar photosphere from electrons of energy 0.5 to 1 MeV. They also infer that the accompanying radio burst is gyrosynchrotron radiation from the same electrons, spiralling in a 1000-gauss magnetic field in the flaring region. Subsequent observations, obtained with rocket- and balloon-borne instruments, confirmed the association of hard X-ray emission with other manifestations of solar-flare activity, particularly type III and microwave bursts (Kundu 1961; Chubb, Friedman, and Kreplin 1960; Winckler, May, and Nasley 1961; Vette and Casal 1961; Anderson and Winckler 1962). Although the discussions of the nature of the hard X-ray source in these papers were qualitative, for the most part, they did present the differing viewpoints that still spark lively controversies among solar physicists.

The presence of high-energy electrons during solar flares had been deduced from observations of flare-associated interplanetary electrons, prior to any of the hard X-ray observations. The detection of photons at energies above 20 keV, simultaneous with other "flash-phase" flare phenomena (e.g., Moreton 1964), was the first indication of the existence of energetic electrons "in situ", within the flaring region itself. Most of the early observations lacked good temporal resolution or energy resolution, or both, and so could not provide precise information on the nature of the hard X-ray spectrum (and thus the electron

energy distribution) and its evolution throughout a flare. It was assumed by several authors, perhaps due to their familiarity with auroral X rays and solar cosmic rays, that the solar-flare X rays originated in a monoenergetic (Peterson and Winckler 1959) or a power-law (Vette and Casal 1960; Anderson and Winckler 1962) distribution of electrons. On the other hand, Chubb, Kreplin, and Friedman (1966) presented X-ray spectra for several flares, observed in 1959, which appeared to be consistent with a thermal plasma at temperatures of order 10^8 K. The non-thermal versus thermal argument has continued to rage throughout the past 20 years, despite progress in the quantity and quality of observations and in the theoretical calculations relating the physical conditions within the source and various plausible electron distributions to the resultant hard X-ray bremsstrahlung spectrum. It has become clear from these efforts that the question is far from being resolved, and that the choice of a thermal or non-thermal (*i.e.*, power-law) fit to a particular spectrum usually is dictated by personal preference rather than by actual knowledge of the "true" electron spectrum.

It is not the intention of this thesis to discuss the relative merits of all extant flare models; reviews, with various biases, are given by Kane (1974), Svestka (1976), Brown (1976), Melrose and Brown (1976), and Report UAG-72 (1979). The purpose of this chapter is to review those physical mechanisms which are relevant to the analyses presented in Chapters 4 and 5, with brief attention to alternate processes. The specific focus is on the interactions between energetic electrons and the ions of the magnetically-structured solar medium, and the resultant hard X-ray and microwave emission.

As first recognized by Peterson and Winckler (1958, 1959), the hard X-ray emission during flares is attributable to energetic electrons. The close association between hard X-ray bursts, meter-wave type III bursts, and microwave events was interpreted from the beginning (Peterson and Winckler 1958, 1959; Kundu 1961, 1965; Anderson and Winckler 1962) as strong evidence of a common origin for these impulsive phenomena: electrons significantly more energetic than the ambient thermalized particles of the solar atmosphere, most probably accelerated during the flash phase of a flare (Moreton 1964). These authors all suggested bremsstrahlung as the emission mechanism responsible for the hard X radiation. De Jager and Kundu (1963) pointed out that, although both type III bursts and hard X-ray/microwave bursts are impulsive phenomena, they probably originate in two different electron populations. As a result, the apparent "beamed" nature of the type-III-emitting electrons cannot be interpreted as support for non-thermal models of the impulsive hard X-ray/microwave source. Other mechanisms proposed to explain the hard X-ray bursts include synchrotron radiation from highly relativistic electrons (Guseinov 1963; Stein and Ney 1963) and inverse Compton radiation from interactions between flare-associated infrared photons and relativistic electrons in the flaring region (Gordon 1960; Shklovskii 1964, 1965; Zheleznyakov 1965). Careful analyses of coincident flare data at several wavelengths and theoretical investigation of the relative merits of these three competing emission processes soon eliminated all but bremsstrahlung as the most likely source of hard X rays during flares (Acton 1964; Korchak 1967; Brown 1976).

Bremsstrahlung, or "braking radiation", also is referred to as free-free radiation. This emission is produced by fast charged particles accelerated, or decelerated, in the

Coulomb fields of other charged particles. At the temperatures and densities typical of solar-flare plasmas, the observed bremsstrahlung emanates from electrons travelling past ions of various charge states; electron-electron bremsstrahlung is a second-order process (dipole radiation is forbidden), while the ions have relatively far lower velocities and so produce negligible ion-ion bremsstrahlung. In a single encounter, the electron is accelerated in the Coulomb field of the ion, and changes direction; the intensity of radiation resulting from an encounter depends on the scattering angle, the initial velocity of the electron, and the charge (Z) of the ion nucleus. In a plasma, of course, many electrons are travelling past a large number of ions, thereby modifying the process according to collective and statistical considerations. Thus, for bremsstrahlung emitted in solar flares, the intensity is a function of the ion density and the isotopic distribution in the emission region, as well as the electron density and energy distribution.

Several early attempts to analyze solar hard X-ray events assumed relativistic electron energies (Peterson and Winckler 1958,1959; Gordon 1960; Guseinov 1962; Shklovskii 1964,1965; Zheleznyakov 1965). Observations of solar flares covering the energy range 10 to 200 keV (Chubb, Friedman, and Kreplin 1960; Winckler, May, and Masley 1961; Anderson and Winckler 1962; Frost 1964; Chubb, Kreplin, and Friedman 1966; Arnoldy, Kane, and Winckler 1968) soon demonstrated that the X-ray-producing electrons must be primarily mildly relativistic, with energies in the range 10 to 100 keV. The discussions of bremsstrahlung in this chapter therefore are valid for mildly relativistic particles only.

The use of satellite-borne instruments (e.g., Frost 1964,1969; Arnoldy, Kane, and Winckler 1968) enabled

comprehensive studies of a large number of flares, observed over timespans of a few years (per satellite). The comparison of such extensive data bases with concident radio and particle observations resulted in the identification of two, fundamentally different, types of hard X-ray emission: impulsive and gradual (see Introduction). Because the characteristics of the hard X-ray and associated emission of these two classes are quite dissimilar, it was concluded that the underlying physical processes also must differ (de Jager 1969; Frost and Dennis 1971). Therefore, this chapter includes sections on several hard X-ray and microwave emission mechanisms, most of which are applicable primarily to the impulsive stage. These discussions are based on relevant material published by Jackson (1962), Bekefi (1966), Brown (1971, 1975, 1976), Brown and McClymont (1975), de Feiter (1975), Tucker (1975), and Crannell et al. (1978).

3.1 HARD X-RAY EMISSION MECHANISMS

Observations of hard X-rays from solar flares provide crucial insight, unattainable from other observations, into the role of energetic electrons in these complex events. With the establishment of bremsstrahlung as the emission mechanism responsible for the X radiation, the development of precise quantitative relationships between the source electrons and the resultant X-ray spectrum became the focus of numerous theoretical analyses (e.g., Holt and Ramaty 1969; Kane and Anderson 1970; Brown 1971). These endeavours proved of timely importance in conjunction with satellite-borne instrumentation, which enabled hard X-ray coverage of hundreds of solar events, over a wide range of intensities and energies. In order to interpret these data in terms of the physics of the source regions, it is necessary to know the shape of the photon spectrum emitted by a particular electron spectrum, as a function of the density and temperature of the relevant site in the solar atmosphere. This portion of Chapter 3 is devoted to analytical development of the relationship between specific electron energy distributions and the associated bremsstrahlung hard X-ray spectra, arriving at practical formulae which are applicable to quantitative analysis of solar-flare observations.

Because the emission of bremsstrahlung is the product of collisions, the basic formula for the emissivity is similar to that of any collisional process. The total bremsstrahlung emission from a volume V, in photons per second per unit energy, is given by the expression

$$J(E) = \int_E^\infty Q_E(W)\ v(W) \left\{ \int_V n_i\ f'(W)\ dV \right\} dW\ , \qquad (2)$$

where $Q_E(W)$ is the cross-section for electron-ion bremsstrahlung at photon energy E, as a function of electron

energy W; $v(W)$, the electron velocity corresponding to energy W; n_i, the ion density as a function of position in the source volume; and $f'(W)$, the differential electron number distribution as a function of energy in units of electrons per unit volume per unit energy (Brown 1971). For purposes of comparison with actual observations, it is more useful to obtain the predicted intensity as seen at Earth. Furthermore, because the hard X-ray coverage to date is not spatially resolved, the volume integral in Equation 2 must be solved approximately, with the terms replaced by quantities which are averaged over the source volume. Thus, the fundamental equation for the total bremsstrahlung emission from a solar source seen at Earth, in photons per second per unit area per unit energy, may be written as follows:

$$I(k) = (1/4\pi R^2)\ n_i \int_E^\infty Q_E(W)\ v(W)\ f(W)\ dW \quad , \qquad (3)$$

where R is the Earth-Sun distance (1 A.U.); and the quantities n_i and $f(W)$ are averaged over the source volume, so that $f(W)$ is in units of electrons per unit energy.

The bremsstrahlung cross section, $Q_E(W)$, has been evaluated analytically by several authors (e.g., Koch and Motz 1959, and refs. therein), for various ranges of the ratio k/W (photon energy to electron energy). The form of the electron distribution function, $f(W)$, is specified by the physical conditions of the assumed source: if the emission originates in a fully ionized, thermal plasma, a Maxwellian distribution is used; if the emission originates in a stationary non-thermal population of electrons, as in a trap (see Section 3.1.4), or in a non-thermal beam of electrons travelling through the ambient solar plasma, then the form of $f(W)$ is non-thermal in nature. A combination of thermal and non-thermal distributions also may be used, as described later in the last section of this chapter.

As mentioned previously, one of two forms for $f(W)$ generally is adopted in analyses of solar-flare X rays: a thermal Maxwellian distribution, or a non-thermal power law in energy (*i.e.*, $f(W) \propto W^{-\delta}$). For the thermal situation, there is no separate "background" plasma, because the electrons and ions constitute a single charge-neutral gas. In the case of an electron beam, the density of the ambient medium through which the beam of electrons travels dictates whether the electrons will lose all their energy in collisions with the ambient ions ("thick-target" case) or travel through the medium without significant energy loss ("thin-target" case). Thermal bremsstrahlung emission is discussed in Section 3.1.1; thick-target and thin-target non-thermal bremsstrahlung are considered in Sections 3.1.2 and 3.1.3, respectively. Bremsstrahlung in models which incorporate features of both thermal and non-thermal distributions is discussed in Section 3.1.4.

3.1.1 Thermal Bremsstrahlung

As originally noted by Chubb, Friedman, and Kreplin (1960), the X-ray spectra of many events are best fit by an exponential distribution function, suggesting a Maxwellian distribution of the energies of the electrons emitting the X radiation. Interpretation of observed X-ray spectra is complicated further by the fact that a power-law spectrum can be duplicated by emission from plasmas at several temperatures (Chubb 1972; Brown 1974). For the X-ray events described in Chapter 4, most of the instantaneous spectra (determined at every peak within each burst) are better fit by single-temperature thermal (exponential times E^{-1}), rather than power-law, forms. This section comprises a quantitative discussion of the properties of X-ray emission from a thermal plasma.

The number of electrons of energy W, per unit energy, in a thermal plasma follows a Maxwellian distribution:

$$f(W) = 2\pi^{-1/2} n_e T^{-3/2} W^{1/2} \exp(-W/T) V \quad , \qquad (4)$$

where n_e is the electron density; T, the plasma temperature; (in energy units); and W, the electron energy.

In general, the photon-energy and plasma-temperature dependences in the formulation of the bremsstrahlung cross section, $Q_E(W)$, are combined into one parameter, the Gaunt factor. Thus, $Q_E(W)$ can be expressed as:

$$Q_E(W) = Q_o G_{ff}(E,W,T)/E \quad , \qquad (5)$$

where the constant Q_o is the classical high-energy bremsstrahlung cross section, and $G_{ff}(E,W,T)$ is the Gaunt factor. For non-relativistic velocities, the electron velocity corresponding to W is given simply by the kinetic-energy relation:

$$v(W) = (2W/m)^{1/2} \quad , \qquad (6)$$

where m is the electron mass.

Substituting Equations 4, 5, and 6 into Equation 3, with $g_{ff}(E,T)$ representing $G_{ff}(E,W,T)$ averaged over all W for a particular range of T, yields the following expression for the spectrum of emitted radiation at a distance of 1 AU from the source, in photons cm^{-2} s^{-1} keV^{-1}:

$$I(E) = 1.07 \times 10^{3} \sum_j (n_e n_i Z^2)_j V \exp(-E/T) g_{ff}(E,T) \quad , \qquad (7)$$

where V is the volume of the emitting region, as before; $g_{ff}(E,T)$ is the temperature-averaged Gaunt factor, and the

summation is performed over the charge, Z, ion density, n_i, and electron density, n_e, for each ionic species, j, in the plasma. The temperature-averaged Gaunt factor has been derived, for various ranges of temperature and the ratio E/T, by Karzas and Latter (1961) and Gorenstein, Gursky, and Garmire (1968); the formulae used to derive $g_{ff}(E,T)$ in the hard X-ray and soft X-ray analyses of Chapters 4, 5, and 6 are given in Table 3-1.

TABLE 3-1

THE TEMPERATURE-AVERAGED GAUNT FACTOR, for $T > 3 \times 10^5$ K

E/T	$g_{ff}(E,T)$
$<<1$	$(3^{1/2}/\pi)\ \ln(2.2\ T/E)$
1	1
>1	$(T/E)^{0.4}$

The summation in Equation 7 depends on the ionization state and the elemental abundances within the source. For a fully-ionized plasma ($T > 10^5$ K), charge neutrality demands that $n_e = \Sigma Z n_i$. Thus, taking solar abundances into account, we have

$$\sum_j [n_e n_i Z^2] = 1.2\ n_e^2. \qquad (8)$$

The emission measure, EM, defined such that $EM = n_e^2 V$, is commonly employed in X-ray astronomy to incorporate the density and volume dependences of the spectrum into one parameter. This is particularly useful when analyzing observations from instruments without spatial resolution, which can not provide information on density gradients within the source volume. The substitution of Equation 8 and the definition of EM into Equation 7 yield (in units of photons $cm^{-2}\ s^{-1}\ keV^{-1}$):

$$I(E) = 1.3\times10^{3}\ EM \exp(-E/T)\ T^{-1/2}\ E^{-1}\ g_{ff}(E,T) \quad . \qquad (9)$$

By definition, the particles within a thermal source obey an isotropic velocity distibution in space; otherwise, a single-temperature plasma could not be maintained. Observations which are sensitive to X-ray directivity achieve prime importance in establishing the thermal or non-thermal nature of hard X-ray burst sources because, as discussed in the following section, non-thermal models predict significant effects due to anisotropy. Recent observations reported by Kane et al. (1980) are consistent with essentially isotropic hard X-ray emission during impulsive bursts, over observation angles between 13° and 79°. This lack of directivity provides strong support for thermal models, but it remains to be seen whether a larger sample of impulsive events exhibits a similar degree of isotropy. Similarly, a negligible degree of hard X-ray polarization is predicted for thermal sources in the solar atmosphere, in contrast to the large polarization expected from non-thermal beams (cf. Langer and Petrosian 1977; Bai and Ramaty 1978).

A potential cause of spectral distortion for both thermal and non-thermal sources is the albedo due to Compton backscattering of the hard X-ray photons from electrons in the photosphere. Although this effect is most prominent for anisotropic non-thermal cases, the contribution to observed thermal spectra can produce measurable distortion at energies around 30 keV (Bai and Ramaty 1978; Mätzler et al. 1978). The main effect is to lower the deduced source temperature by a few keV at most, which, for the OSO-5 observations, is on the order of the uncertainty in the derived temperature value itself. Because the lowest energy

considered in the spectral-fitting technique outlined in Chapter 4 is 28 keV, the albedo contribution has been neglected.

3.1.2 Non-thermal Bremsstrahlung: Thick-target Case

The term "thick-target" bremsstrahlung originally was employed by experimental physicists to denote the radiation emitted by a beam of high-energy electrons striking a target thicker than the energy-loss range of the electrons being considered. In solar-flare modelling, the analogous situation comprises a dilute beam of energetic electrons, directed downwards through the solar atmosphere, which emits thick-target bremsstrahlung upon reaching a region dense enough for the electrons to lose all their energy in collisions with the ambient medium. In all thick-target models, this target region is located in the chromosphere or transition zone, depending on the assumed energies in the electron beam and on the chosen model for the density structure of the solar atmosphere. These models usually assume a power-law electron energy distribution function, that is,

$$f(W) = A\, W^{-\delta} \quad , \tag{10}$$

where the real number δ is called the (power-law) spectral index, and A is a constant.

The simple power-law distribution in Equation 10 cannot be applied directly, because f(W) as defined approaches infinity as the electron energy becomes smaller and smaller. To avoid such unphysical conditions, a low-energy cut-off, usually of order 10 keV, is imposed on the electron spectrum. In order to duplicate observed spectra, which often include steepening at high photon energies, a high-energy cut-off (usually of order 100 keV) may be adopted as

well (Cf. Kane and Anderson 1970). The calculation of bremsstrahlung under these conditions differs markedly from the thermal case, covered in the last section. Instead of dealing with a single plasma, in which the number and density of the emitting electrons are directly related to the number and density of ions, two distinct components must be considered: a beam of high-energy electrons, of number density n much less than in the target region; and the denser, thermal plasma of electrons and ions in which the beamed electrons are stopped. The directional anisotropy of the electron beam also causes potentially significant modifications to the observed X-ray spectrum, primarily due to albedo, polarization, and backscattering effects. The effects of directivity on the bremsstrahlung X-ray spectrum have been studied in detail by Petrosian (1973, 1975), Langer and Petrosian (1977), and Bai and Ramaty (1978). Polarization of hard X-ray emission has been studied by Elwert and Haug (1970), Haug (1972), Brown (1972), Langer and Petrosian (1977), and Bai and Ramaty (1978), with emphasis on non-thermal beams as the origin of the X rays. Their results remain to be tested, though, because reliable polarization measurements of solar hard X rays are not available at present. These additional complications are not included in the intentionally-simplified treatments within this chapter. As pointed out by Mätzler et al. (1978), the photospheric albedo primarily affects the hard X-ray spectrum at photon energies around 30 keV. The OSO-5 data analyses described in Chapters 4 and 5 utilize the X-ray spectra above 28 keV only, thereby allowing the effects of the albedo to be neglected (see Section 3.1.1). Similarly, isotropic emission is assumed throughout this work, so that directivity and its effects on the X-ray spectrum need not be discussed here.

In solar flares, thick-target conditions imply that the electrons lose all their energy, mainly through electron-electron collisions, in the chromospheric "target region". The dominant radiation mechanism, electron-ion bremsstrahlung, only expends 10^{-5} times as much energy. The rate of collisional energy loss per unit time is, therefore:

$$dW/dt = -55.7\pi e^4 n_i v(W)/W \quad , \quad \text{for } 20 < W < 100 \text{ keV} . \qquad (11)$$

For target densities typical of the chromosphere, it can be assumed that a braking electron emits each photon instantaneously, relative to the energy-loss time scale. In other words, the electron energy does not change during a bremsstrahlung-producing encounter. An electron of initial energy W_o will emit photons of energy E as long as $W_o > E$. Thus, the total number of photons of energy E, per unit E, emitted by a braking electron of initial energy W_o, is:

$$m(E,W_o) = \int_{W_o}^{E} Q_E(W)\, n_i\, v(W)\, dt \quad , \qquad (12)$$

where $W = W(t)$; and $Q_E(W)$, the bremsstrahlung cross section, as introduced in Section 3.1.1. Substitution of Equation 11 into Equation 12 yields

$$m(E,W_o) = K \int_{W_o}^{E} W\, Q_E(W)\, dW \quad , \qquad (13)$$

where $K = (55.7\pi e^4)^{-1}$. Note that $m(E,W_o)$ is independent of the ion density, n_i. For comparison with observations, it is implicitly assumed that the energy-loss timescale is less than the temporal resolution of the detector.

Thus, the total photon emission rate seen at Earth can be closely approximated by the product of two quantities, the initial electron spectrum, $f(W_o)$, and the total number of photons emitted by each electron in the distribution, $m(E,W_o)$, integrated over all possible values of W_o:

$$I(E) = (1/4\pi R^2) \int_E^\infty f(W_0)\ m(E,W_0)\ dW_0 \quad . \tag{14}$$

With $Q_E(W)$ evaluated according the Bethe-Heitler formula (*Cf.* Brown 1971), and $m(E,W_0)$ defined according to Equation 13, the total photon emission rate seen at Earth is:

$$I(E) = (1/4\pi R^2) Q_0 K\ E^{-1} \int_E^\infty f(W_0) \{ \int_E^W \ln \frac{1+\sqrt{1-E/W}}{1-\sqrt{1-E/W}}\, dW \}\, dW_0 \quad . \tag{15}$$

By reversing the order of integration and defining the integral electron spectrum $F(W) = \int_W^\infty f(W_0) dW$, a reduced expression for I(E) results:

$$I(E) = (1/4\pi R^2) Q\ K\ E^{-1} \int_E^\infty F(W)\ \ln \frac{1+\sqrt{1-E/W}}{1-\sqrt{1-E/W}} dW \quad . \tag{16}$$

For a power-law injection spectrum, this expression is soluble analytically. Taking into account the necessity of a low-energy limit on the electron distribution, as previously discussed, f(W) is redefined as follows:

$$f(W) = A(E_0/W)^\delta \quad , \tag{17}$$

in units of electrons s^{-1} keV^{-1}, where E_0 is the low-energy cut-off (in keV). Therefore,

$$F(W) = \int_E^\infty A\ (E_0/W)^\delta\ dW = AE_0^\delta\ W^{-\delta+1}/(\delta-1) \quad , \tag{18}$$

in units of electrons s^{-1}. The tabulated Beta function (*Cf.* Brown 1971), B(n+1, 1/2), which is defined such that

$$B(n+1,1/2) = (n+1) \int_0^1 x^n\ \ln \frac{1+\sqrt{1-x}}{1-\sqrt{1-x}}\ dx \quad , \tag{19}$$

also is used below.

Equations 16, 18, and 19 yield the intensity of thick-target X rays from a solar plasma seen at Earth, in photons cm^{-2} s^{-1} keV^{-1}:

$$I(E) = (1/4\pi R^2) K Q_0 A E_0^{\delta} (\delta-1)^{-1} E^{-1} \int_E^{\infty} W^{-\delta+1} \ln \frac{1+\sqrt{1-E/W}}{1-\sqrt{1-E/W}} dW$$

$$= (1/4\pi R^2) K Q_0 A E_0^{\delta} E^{-\delta+1} (\delta-1)^{-1} \int_0^1 (E/W)^{\delta-3} \ln \frac{1+\sqrt{1-E/W}}{1-\sqrt{1-E/W}} d(E/W)$$

$$= (1/4\pi R^2) K Q_0 B(\delta-2, 1/2) [(\delta-1)(\delta-2)]^{-1} A (E_0/E)^{\delta-1}. \quad (20)$$

Thus, we see that the spectrum of the emitted X rays is flatter than the injected electron spectrum, such that the X-ray spectral index is less by 1 than the electron spectral index, δ.

Thus far, the derivation presented in this section has been concentrated on determining the photon spectrum produced by injecting a given electron spectrum into a thick target. In solar-physics research, however, the electron spectrum obviously cannot be measured *in situ*. The calculation of pertinent application, therefore, is the reverse of the process described above: to determine the characteristics of the flare-accelerated electron distribution from an observed (or hypothetical) X-ray spectrum. The inversion technique can be invoked, in principle, for any choice of electron distribution and of emission model; in practice, the form of the observed X-ray spectrum (*e.g.*, exponential or power law) often is assumed to indicate the appropriate electron spectrum. Because this type of analysis is necessary for the model testing in Chapter 5, the effective thick-target parameters which can be derived from X-ray observations and their relationship with actual physical conditions in the source region are included here. The motivation for focussing on specific forms of the thick-target parameters also is discussed, to clarify the method of model testing presented in Chapter 5.

The inversion of power-law photon spectra to yield the parent electron spectra is described in detail by Brown (1971). In the thick-target case, the injected electron distribution is modified by collisional energy losses in the target region, which preferentially deplete the low-energy portion of the spectrum (cf. Equation 11). As noted earlier (Equation 13 and following text), the relationship between the injected electron spectrum and the thick-target X-ray spectrum is independent of the target density, a feature which is unique to the thick-target case (see Sections 3.1.1 and 3.1.3). At present, no method exists for direct determination of the densities in hard X-ray sources; model-dependent calculations based on coincident analysis of emissions at other wavelengths (e.g., Crannell et al. 1978) apparently yield reasonable density estimates, but remain controversial topics. As a result, the thick-target assumption often is preferred for deducing electron spectra from X-ray observations. For a power-law X-ray spectrum of the form $I(E) = A\ E^{-\gamma}$ photons $cm^{-2}\ s^{-1}\ keV^{-1}$, where photon energy E is in keV, Brown derived the following expression for the number flux of injected electrons, with energies above a given low-energy cutoff, required by the thick-target model to account for the observed X-ray spectrum:

$$F(W_1) = 2.0 \times 10^{33}\ A\ (\gamma-1)^2\ B(\gamma-1/2, 1/2)\ W_1^{-\gamma}\ \text{electrons}\ s^{-1}, \quad (21)$$

where W_1 is the low-energy cutoff, in keV; A and γ are the parameters which characterize the hard X-ray spectrum; and $B(\gamma-1/2, 1/2)$ is the Beta function (Equation 19).

The thick-target parameters $F(W_1)$ and γ provide a convenient description of the instantaneous X-ray spectrum, and are used accordingly in the analysis presented in Chapter 5. It must be stressed that $F(W_1)$ does no

necessarily reflect the actual electron distribution emitting the observed X-ray spectrum; it can be interpreted as a purely effective parameter, representing the number flux (electrons s^{-1}) required by the thick-target case to reproduce the observed X-ray flux and spectral index. Specifically, if there is continuous reacceleration of the electrons in the source, as in a magnetic trap (cf. Section 3.1.4), then it is more meaningful to consider the instantaneous non-thermal emission measure. The non-thermal emission measure is defined as follows (Brown 1971; Hoyng 1975):

$$n\,N(W_1) = 1.46 \times 10^{8}\, W_1^{3/2}\, (\gamma - 3/2)^{-1}\, F(W_1) \quad cm^{-3}\ , \qquad (22)$$

where n is the background ion density, in cm^{-3}; and $N(W_1)$, the total number of energetic electrons with energies greater than W_1.

The parameters $F(W_1)$ and $nN(W_1)$ play crucial roles in the analysis of Chapter 5, wherein the applicability of the betatron-acceleration model (Brown and Hoyng 1975) to complex solar emission is evaluated. Because the test of the model requires comparison of observed X-ray spectral parameters with those predicted by the model, for each observational interval within a burst, it is convenient to formally characterize each instantaneous X-ray spectrum by the appropriate values of $F(W_1)$ and γ. The effects of the betatron process on the energetic electrons, as reflected in the hard X-ray spectral behaviour, can be characterized consistently by parameters which are directly comparable to the reduced X-ray observations. The fundamental premise of the model, the reacceleration of the X-ray-emitting electrons by means of the betatron process, naturally suggests the use of the non-thermal emission measure (Equation 22) to express the X-ray characteristics predicted

by the model. The foregoing discussion is intended only as an introduction to the concept of the effective thick-target parameters which are utilized later in this thesis; the betatron model itself, and the derivation of specific expressions for the thick-target parameters within the context of that model, are presented in more detail in Chapter 5.

The electron kinetic energy needed by the thick-target case to reproduce a given X-ray flux can be determined through inversion of Equation 20, and subsequent integration of the resultant electron energy spectrum (e.g., Brown 1975). This procedure was applied to the large flare of 1972 August 4 by Hoyng, Brown, and van Beek (1976), yielding the following requirements: 4×10^{39} electrons with energies ≥ 25 keV, with a total energy of 2×10^{32} erg. These requirements increase by an order of magnitude if the low-energy cutoff is placed at 10 keV (Brown 1975). To illustrate the problem in accepting this estimate, we note that the acceleration of 4×10^{39} electrons implies the energization of *every* electron in a volume of 2×10^{30} cm^3, assuming a reasonable coronal density of 2×10^9 cm^{-3}. A more realistic view of the acceleration mechanism, which is expected to be much less than 100% efficient, would necessitate the involvement of an even greater volume to provide sufficient electrons. None of the observational evidence presently available indicates that volumes of this magnitude are involved in flares (*cf.* Svestka 1976). Furthermore, the rapid intensity variation observed in impulsive hard X-ray bursts require acceleration on comparably short timescales. No acceleration mechanism proposed to date is capable of accelerating such large numbers of electrons, to such high energies, at such rapid rates.

Another aspect of the so-called "particle-number" problem becomes apparent upon considering the number and energy of the electrons responsible for microwave emission associated with most impulsive hard X-ray bursts. Although the theoretical treatment of the emission and absorption mechanisms affecting the observed microwave spectra is considerably more complex than that of the hard X radiation, the characteristics of the emitting electrons may be deduced in a manner similar to that described above for the X-ray spectra. For the impulsive event of 1966 July 7, Takakura (1972) found that the electron energy needed to produce the peak microwave intensity is approximately 10^{25} erg s^{-1}, while, for the associated hard X-ray event, a total electron energy of 2×10^{28} erg s^{-1}, for electrons above 100 keV, is required to produce the observed peak flux (de Feiter 1975). Consequently, the total kinetic energy of the electrons producing the hard X-ray event is approximately 10^3 times that of the electrons responsible for the microwave burst. Several analyses have attempted to reconcile the discrepancy between the hard X-ray and microwave electron-energy estimates (e.g., Holt and Ramaty 1969; Takakura 1972; Zirin and Tanaka 1973; Takakura 1975), mostly through manipulation of the physical parameters which determine the relevant low-frequency absorption mechanism (see Section 3.2.2). At present, it is unclear whether these effects are reasonable excuses for eliminating the problem, as the applicability of the various absorption processes is still under debate.

It should be noted that the particle-number problem is alleviated significantly if the thermal case is assumed, although the degree of improvement depends on how "thermal" the source actually is. The hard X-ray/microwave electron-energy discrepancy also disappears, if a common source is assumed for both emissions (e.g., Crannell et al. 1978).

3.1.3 Non-thermal Bremsstrahlung: Thin-target Case

If solar-flare electrons stream outwards through the corona, the low densities encountered result in X-ray emission associated with thin-target conditions; this corresponds to negligible collisional energy losses from the energetic electrons to the ambient medium. Consequently, the electron spectrum is not modified by collisions, as occurs in thick-target situations, but remains in its initial form. Equation 3 thus simplifies to the following expression:

$$I(E) = (\Delta N/4\pi R^2) \int_E^\infty f(W)\ Q_E(W)\ dW \quad , \qquad (23)$$

where ΔN is the target column density in protons per unit area. For the power-law injection spectrum of Equation 17 and the Bethe-Heitler formula for $Q_E(W)$, this equation becomes:

$$I(E) = (\Delta N/4\pi R^2) Q_0 A E_0^{\delta} E^{-1} \int_E^\infty (E_0/W)^{\delta} \ln\frac{1+\sqrt{1-E/W}}{1-\sqrt{1-E/W}}\, dW \ . \qquad (24)$$

As in the thick-target case, this expression can be solved analytically, involving use of the Beta function (Equation 19). The result is

$$I(E) = (\Delta N/4\pi R^2) Q_0\ B(\delta-1, 1/2)\ (\delta-1)^{-1}\ A(E_0/E)^{\delta} \ . \qquad (25)$$

In contrast to the thick-target result, we find that the thin-target X-ray spectrum has the same slope as the injected electron spectrum, so that the thin-target X-ray spectral index is greater by 1 than the thick-target spectral index. The most important characteristic of the thin-target case, however, is that most of the electrons escape the "target" region with little or no energy loss. As a result, the thin-target case requires more electron energy than does the thick-target case to reproduce a given

X-ray intensity. The thick-target model itself requires unreasonably large electron numbers and total energy to account for all but the smallest hard X-ray events, as discussed in Section 3.1.2. The discrepancy between the kinetic energy of the electrons needed to produce hard X-ray bursts and that of the associated microwave events (see Section 3.1.2) also is exacerbated for the thin-target case. Therefore, the thin-target emission models have been discounted, for the most part, as viable explanations for most hard X-ray bursts (e.g., de Feiter 1975).

3.1.4 Trap Models

Neither thick-target nor thin-target models for production of solar bremsstrahlung X rays can fully explain all features of the flare phenomenon. The shortcomings of both cases have been discussed thoroughly by several authors, including Hudson (1973), Kane (1974), Brown (1975), and Svestka (1976). To summarize, we point out the major faults in each model. In a purely thick-target situation, all the electron energy is deposited in the dense chromosphere/transition zone; consequently, this cannot provide type III bursts, interplanetary electrons, and "behind-the-limb" X-ray bursts, which are observed at heights well above the chromosphere. On the other hand, the thin-target case cannot account for the flare emissions which must come from the photosphere and chromosphere (i.e., H-alpha, EUV, and soft X rays), and requires even more energy than the thick-target case to reproduce a given X-ray spectrum (see Sections 3.1.2 and 3.1.3).

Thus, it seems natural to consider sources which combine the features of both thick- and thin-target models: the electron trap models. As originally proposed by Takakura

and Kai (1966), the prototype trap model described hard X-ray and microwave bursts in terms of energetic electrons magnetically trapped in the corona. The discovery that soft X-ray flares occur primarily in magnetically-bounded loops in the chromosphere/corona added further credence to the idea that the impulsive emissions also originate in a loop-shaped trap. The initial hypothesis of Takakura and Kai has been greatly modified over the years, for better agreement with the hard X-ray and microwave observations and with advances in theoretical treatments of the problem. Major work on the subject has been done by Brown and Hoyng (1975), Brown and McClymont (1976), Melrose and Brown (1976), and Emslie, McCaig, and Brown (1979).

The most striking difference between the earliest trap models and the currently-accepted versions is due to the realization that precipitation of electrons must occur in trap models, thus providing the more appropriate nomenclature "trap-plus-precipitation" models (Melrose and Brown 1976). The inclusion of a precipitating component results from Coulomb scattering of electrons into the loss cone (i.e., diffusion in pitch angle), at a rate which is estimated to be 2 to 3 times the collisional energy-loss rate (Hudson 1972; Melrose and Brown 1976). Unlike thick- and thin-target models, the trap-plus-precipitation model is compatible with the high coronal location of behind-the-limb events, yet also allows heating of the denser chromospheric layers by the precipitating electrons.

For convenience, the X-ray emission in the trap-plus-precipitation model may be divided into two components: $I_T(E)$, the emission from the electrons within the trap, and $I_p(E)$, the thick-target X rays from the precipitating electrons. Following Melrose and Brown (1976) and Sections 3.1.2 and 3.1.3, explicit expressions for $I_T(E)$ and $I_p(E)$

are derived below. In this treatment, wave-particle interactions and collective effects have been ignored, and are expected to be negligible (Melrose and Brown 1976). From Equations 3 and 6, the X-ray spectrum from the trapped electrons is :

$$I_T(E) = (1/4\pi R^2)\, n_i\, (2/m)^{1/2} \int_E^\infty W^{1/2}\, Q_E(W)\, f(W)\, dW \,. \qquad (26)$$

The precipitating component produces thick-target X rays, which can be evaluated by the same method as in Section 3.1.2. Here, however, the electron distribution is related to the trapped-electron spectrum by the precipitation rate, $r_p(W)$, so that there are $r_p(W)\, f(W)$ precipitating electrons per unit energy range per unit time. In the weak-diffusion limit, the precipitation rate is simply twice the Coulomb energy-loss rate, that is,

$$r_p(W) = 2\, r_0\, W^{-3/2} \,, \qquad (27)$$

where $r_0 \approx 5 \times 10^{-9} n_e\ s^{-1}\,(keV)^{3/2}$. Thus, following Equations 12 through 14, with $dW/dt = -r_0 W^{-1/2}$, we have

$$I_p(E) = (1/4\pi R^2)\, n_i\, (2/m)^{1/2} r_0^{-1} \int_E^\infty r_p(W)\, f(W)\, dW \int_E^W W_0\, Q\,(W_0)\, dW_0 \,. \qquad (28)$$

Substituting for r_p according to Equation 27, the precipitating electron X-ray spectrum is found to be

$$I_p(E) = (1/4\pi R^2)\, n_i\, (2/m)^{1/2} \int_E^\infty 2W^{-3/2}\, f(W)\, dW \int_E^W W_0\, Q\,(W_0)\, dW_0 \,. \qquad (29)$$

After partial integration of Equation 29, the expressions for I_T and I_p may be combined to yield the total X-ray spectrum from the trap-plus-precipitation model:

$$I(E) = I_T(E) + I_p(E)$$

$$= (1/4\pi R^2)\, n_i\, (2/m)^{1/2} \int_E^\infty W^{1/2} f_{ef}(W)\, Q_E(W)\, dW \quad , \qquad (30)$$

where

$$f_{ef}(W) = f(W) + 2\, W^{1/2} \int_W^\infty W_0^{-3/2}\, f(W_0)\, dW_0 \quad . \qquad (31)$$

$f_{ef}(W)$ can be interpreted as the equivalent electron energy spectrum in a trap model without precipitation. In other words, $f(W)$ produces the same X-ray spectrum in a trap-plus-precipitation situation as does $f_{ef}(W)$ in a trap without precipitation.

In the case of a power-law electron spectrum, we note that the X-ray spectrum from the precipitating electrons is proportional to that from the trapped component, so that the spectral indices are identical. The spectrum of precipitated electrons is steeper than in the trap itself, due to its collisional origin, just enough to balance out the greater hardness of a thick-target X-ray spectrum relative to a trap emission spectrum.

Trap models in general have an additional advantage over pure thick- or thin-target models in that the trap itself can account for rapid variations in the X-ray spectrum. In non-trap situations, intensity increases within a burst can result only from injection of new particles; and even for moderate events, an unreasonably large number of acccelerated electrons would be required to account for the observed flux (cf. Section 3.1.2). A trap allows for continued reacceleration of the trapped population of electrons, perhaps through pulsations in the magnetic structure of the trap (see Chapter 5), thus avoiding the particle-number problem. The energy requirements in either case remain problematically large, however, as a difficulty intrinsic to all non-thermal models (cf. Brown 1976).

To mitigate this extreme energy demand while retaining the advantages of a trap, several recent efforts have been devoted to the development of a "quasi-thermal" trap model (Brown, Melrose, and Spicer 1979; Smith and Lilliequist 1979; Vlahos 1979; Vlahos and Papadopoulos 1979; Brown, Craig, and Karpen 1980). In this model, the X rays emanate primarily from a hot (T of order 10^8 K) thermalized electron plasma, essentially confined to the top of the loop by a pair of conduction fronts which propagate at the ion-acoustic speed down the legs of the loop. Electrons with velocities greater than 2.6 times the electron thermal velocity are not confined by the slowly moving fronts, however, and precipitate down to the footpoints. Some thick-target X rays are emitted by this precipitating component, but the bulk of the X radiation comes from the thermal electrons. According to Smith and Lilliequist (1979), the Maxwellian-plus-tail model is at least 20 times more efficient (*i.e.*, requires 20 times less energy than non-thermal trap models. Complexity in the intensity structure of a burst may be achieved by means of numerous flaring "kernels", instead of a single bulk-heated plasma at the top of the arch; this possibility has been investigated by Brown, Craig, and Karpen (1980).

3.2 MICROWAVE EMISSION MECHANISMS

The basic connection between hard X-ray and microwave emission during flares was recognized quite early in the history of coincident observations at these wavelengths (Kundu 1961,1965). Intensity-versus-time profiles of impulsive microwave events closely resemble the associated hard X-ray profiles, although the resemblance generally deteriorates during the decay phase. The temporal coincidence between microwave and hard X-ray emissions during a flare was established originally by Kundu (1961), Anderson and Winckler (1962), and de Jager and Kundu (1963).

In recent years, the availability of coordinated observations with improved temporal resolution has led to the confirmation of this striking correlation, even in small structural details of the flux plots (*e.g.*, Figures 4-3 and 4-4). However, our understanding of the physical mechanisms behind this relationship remains incomplete, with several competing models currently being promoted to explain the observed characteristics. This section of Chapter 3 is devoted to the impulsive microwave emission: what the properties of solar microwave bursts indicate about the physical nature of their sources; and how these sources may be related to the source of the associated hard X-ray burst.

The early (pre-1965) history of solar microwave observations and interpretations is reviewed comprehensively by Kundu (1965). Microwave bursts from the Sun were first observed by Covington and coworkers (Covington 1948,1951). Systematic studies of these events initially appeared during the 1957-1958 International Geophysical Year (IGY), and have continued thereafter. Throughout this dissertation, the frequency regime denoted "microwave" is defined to be between 2 and 100 GHz; most microwave observations, however, only cover selected frequencies in the range 2 to 20 GHz. At present, the technology of microwave observations allows more comprehensive coverage than is attainable for hard X-ray observations. Polarization data and spatial information have been obtained for numerous microwave events, while the temporal resolution of many facilities has reached the millisecond range. Microwave events associated with the impulsive phase are classified variously as Type A/Simple Bursts and Impulsive Outbursts (Kundu 1959,1965), as well as the Simple 1, Simple 2, Spike, Complex, and Great burst categories used by the Solar-Geophysical Data reports (*cf.* Solar-Geophysical Data Descriptive Text 1970). The Complex and Great bursts often evince a second, non-impulsive stage;

the following discussion is applicable primarily to the Simple/Spike bursts and the impulsive portions of Complex and Great bursts.

As was the case for the hard X-ray emission processes, early microwave observers correctly identified the general emission mechanisms responsible for microwave bursts during solar flares: the gyrosynchrotron or the synchrotron process. Both types of radiation originate in high-energy electrons, spiralling around magnetic-field lines. In comparison to the bremsstrahlung process, the intensity, polarization, and directivity of (gyro) synchrotron emission depend on the same source parameters, with an important addition: the magnetic-field strength and geometry along the electrons' path. As a result, the analysis and interpretation of microwave spectra are considerably more complicated than for hard X-ray spectra. Furthermore, the solar atmosphere is practically transparent to hard X rays but not to microwaves. The effects of the plasma above the source greatly modify the outgoing microwave emission at lower frequencies, and must be taken into account.

Gyrosynchrotron and synchrotron emission are differentiated by the energy of the emitting electron: synchrotron emission comes from relativistic particles, while gyrosynchrotron denotes a mildly relativistic source. Because very high electron energies and extreme brightness temperatures are required by the synchrotron process for agreement with observed spectra, this process is considered a viable emission mechanism only in large bursts, particularly to explain the so-called "microwave type IV" phenomena. Other features support the gyrosynchrotron hypothesis: the electron energies inferred from observations by means of this hypothesis, whether a thermal or a non-thermal spectrum is assumed, compare favorably with

the predictions of most models of electron acceleration in flares; the degree of polarization, usually circular (Kundu 1965), is typical of gyrosynchrotron radiation; coherent plasma emission, as suggested by Bhatia and Tandon (1970), would require unreasonably large magnetic-field strengths ($B > 10^4$ G); thermal bremsstrahlung (Hachenberg 1958; Hachenberg and Wallis 1960; Takakura 1967) cannot reproduce the spectral shape of the majority of microwave bursts. Therefore, the gyrosynchrotron process is preferred as the source of impulsive microwave radiation during flares.

Within the past decade, several theoretical analyses of gyrosynchrotron emission under conditions relevant to solar flares have appeared in the literature (Ramaty 1969; Holt and Ramaty 1969; Takakura and Scalise 1970; Takakura 1972; Ramaty and Petrosian 1972; Kovalev and Korolev 1974; Tarnstrom 1976,1977; Mätzler 1978; Dulk, Melrose, and White 1979). Although solar microwave emission and its implications about the flare phenomenon are not thoroughly understood, the abovementioned analyses have enabled significant progress in the formation of a clearer picture of the roles played by energetic electrons and the complex magnetic-field topology in flares. In all studies of gyromagnetic emission and propagation through the ambient medium, the electron plasma frequency and electron gyrofrequency play prominent roles. The plasma frequency describes the oscillatory period of electrons within a plasma, the corona in this instance, due to the long-range forces coupling the particles; it is defined as follows (Krall and Trivelpiece 1973):

$$f_p = (n_e e^2/\pi\, m)^{0.5}$$
$$= 8.7\times10^{-3}\, n_e^{0.5} \quad \text{MHz} , \qquad (32)$$

where n_e is the local electron density in cm^{-3}, and m, the mass of the electron. The electron gyrofrequency is the frequency at which an electron will spiral around a particular magnetic-field line, and is defined as follows:

$$f_B = e\ B\ (1-b^2)^{0.5}/2\pi\ m\ c \quad , \qquad (33)$$

where B is the magnetic-field strength; c, the speed of light; and b, the ratio of the electron velocity to c. The $(1-b^2)^{0.5}$ term is a relativistic correction, more recognizable as the inverse of the Lorentz factor, Γ, where $\Gamma \equiv [\,1/(1-b^2)\,]^{0.5}$. In the non-relativistic limit, this term is approximately unity, so that

$$f_B \approx 2.8\ B \quad MHz \quad , \qquad (34)$$

for B in gauss. This approximation is adequate for the thermal case, because the steep electron energy spectrum ensures that the contribution from relativistic electrons is small. However, the Lorentz factor reappears in the non-thermal case, discussed in Section 3.2.2.

Section 3.2.1 comprises a quantitative overview of gyrosynchrotron microwave emission from a thermal population of electrons, as a counterpart to the hard X-ray source presented in Section 3.1.1. Gyrosynchrotron radiation from a non-thermal electron beam is considered in Section 3.2.2. In parallel with Section 3.1.3, the final section of this chapter covers microwave emission in models which combine thermal and non-thermal source characteristics.

3.2.1 Thermal Gyrosynchrotron

The brightness temperatures of impulsive microwave bursts are typically of order 10^7 to 10^9 K (1 to 100 keV) at flux maximum (Kundu 1965). These high temperatures, together

with the observed polarization of many bursts, originally led solar radio observers to conclude that the emission must come from a non-thermal population of electrons. This assumption has been challenged recently, as a response to mounting evidence that some hard X-ray bursts originate in a hot thermal plasma (Crannell et al., 1978; Elcan 1978; Mätzler et al., 1978). Also, the spectral shapes and intensity profiles observed during many microwave bursts are consistent with a thermal origin, as originally suggested (but wrongly attributed to bremsstrahlung) by Hachenberg and Wallis (1961). Models in which the impulsive X rays and microwaves emanate from the same electron population are attractive because, in these models, the close similarity in hard X-ray and microwave intensity structures during coincident events is a natural consequence of a common source. The gyrosynchrotron emission evaluated in this section can be thought of as originating in the same thermal plasma that produced the hard X-ray emission of Section 3.1.1.

The characteristics of microwave radiation from high-temperature plasmas were investigated originally by plasma physicists (e.g., Trubnikov 1961; Hirshfield, Baldwin, and Brown 1961; Hirshfield and Brown 1961; Drummond and Rosenbluth 1963; Shukla and Singh 1972). However, the source conditions of interest to plasma research, particularly those applicable to tokamak and other plasma machines, are not necessarily appropriate for solar-flare situations. More recent analyses by solar physicists, as well as plasma physicists interested in the solar-flare problem, have concentrated on the density, temperature, and magnetic-field strength regimes typical of solar flares. Mätzler (1978) and Dulk, Melrose, and White (1979) have calculated the gyrosynchrotron emission from electrons with a Maxwellian energy distribution, for temperatures above

10^8 K and densities typical of the solar corona, with similar results. The following discussion is based primarily on material in these papers, as well as relevant portions of Bekefi (1966).

For thermal plasmas with temperatures above 7 keV in which the magnetic energy density exceeds the thermal energy density, the total gyrosynchrotron emissivity exceeds the bremsstrahlung emissivity by several orders of magnitude (Mätzler 1978). In the microwave range, the gyrosynchrotron component dominates completely. Consequently, bremsstrahlung at microwave frequencies is neglected here.

In the non-relativistic limit, the gyromagnetic emission spectrum from one electron or an ensemble consists of a series of lines, each at a harmonic of the gyrofrequency f_B, with intensity decreasing and half-width increasing towards higher harmonics (*e.g.*, Bekefi 1966, Figure 6.10a). As higher electron energies are considered, the Lorentz factor becomes significant and the electron velocity distribution must be considered. Consequently, the spectrum loses its discrete-line character at all but the lowest frequencies, while the frequency at which the maximum intensity occurs shifts to higher harmonics. In their study of microwave emission from quasi-thermal electrons in solar flares, Dulk, Melrose, and White (1979) conclude that the harmonic numbers of interest are in the range $s=f/f_B \sim 10$ to 100.

We briefly consider propagation effects on thermal gyrosynchrotron spectra. Most of these effects are much more important for non-thermal sources, and will be covered in depth in Section 3.2.2. The influence of the corona on the outwardly-propagating microwave emission is confined primarily to the lowest harmonics of the gyrofrequency, for the following reasons. Radiation at and below the local

plasma frequency will be suppressed totally. Because the electron density decreases with height in the solar atmosphere, the highest plasma frequency of concern is that of the source region. For typical burst densities, $n_e \sim 10^8$-10^{10} cm^{-3}, the corresponding plasma frequency is in the range $f_p \sim 100$-1000 MHz--at most equal to the lower limit of the frequency range considered "microwave". The process of gyroresonance absorption is self-explanatory: the absorption of gyrosynchrotron emission by thermal electrons in the ambient medium, with maximum absorption at "resonances" (harmonics) of the local gyrofrequency. In essence, the actual mechanism is identical to gyrosynchrotron self-absorption (see below); gyroresonance absorption is due to electrons which are not sources of the burst-related emission, whereas self-absorption refers to absorption by the gyro-emitting electrons themselves. Gyroresonance absorption by thermal electrons in the coronal plasma in and above the source affects predominately the lowest harmonics: typically, the fundamental and second harmonic for the ordinary mode, and the fundamental, second, and third harmonics for the extraordinary mode (cf. Kundu 1965; Takakura 1967; also Section 3.2.2). Magnetic-field strengths in most burst sources are in the range 70 to 700 G, corresponding to $f_B \sim 200$ to 2000 MHz; for the lower field strengths, then, even the third harmonic is safely below the microwave range. In the non-thermal case, where emission at lower harmonic numbers predominates (see Section 3.2.2), thermal gyroresonance absorption has significant influence on the spectrum. On the other hand, the harmonic numbers of relevance to thermal sources are sufficiently high that gyroresonance absorption can be neglected. Free-free absorption by coronal electrons may contribute negligible absorption at microwave frequencies (Holt and Ramaty 1969). However, for sources at sufficiently small heights or low temperatures, this absorption mechanism could

dominate (Ramaty and Petrosian 1972; Mätzler 1976; Marsh et al. 1980). A detailed discussion of free-free absorption is given in Section 3.2.2; it is shown that this process can be neglected for the thermal sources studied in this section.

The remaining absorption process of interest is gyrosynchrotron self-absorption, which is the reabsorption of the radiation by the source electrons themselves. For the densities, magnetic-field strengths, and temperatures observed during solar bursts, self-absorption is an integral part of the emission process. The Razin suppression mechanism (cf. Section 3.2.2) also must be considered, since the self-absorption process and the Razin effect are highly interdependent (Ramaty 1969). As is shown in Section 3.2.2, the densities and magnetic-field strengths typical of most thermal bursts identified to date (i.e., Crannell et al. 1978) yield Razin cut-off frequencies which are well below the microwave range (e.g., $f_R \sim 200$ MHz). Dulk, Melrose, and White (1979) confirm that the Razin effect has little influence on the absorption coefficients of thermal gyrosynchrotron sources, for the frequency range, magnetic-field strengths, and densities relevant to impulsive microwave bursts.

The emission and absorption of a Maxwellian plasma are related by Kirchoff's Law; thus, to solve the transfer equation for the intensity as a function of frequency, only the absorption coefficients need to be known. Both the extraordinary and the ordinary (x and o) modes must be considered, since the absorption coefficients for these modes can differ greatly. The transfer equation for an isothermal point source (Bekefi 1966; Mätzler 1978) yields the following expression for the intensity, in each mode, seen at Earth:

$$I_{o,x}(f) = 0.08\ f^2\ T\ [\,1-\exp(-\tau_{o,x})\,] \quad \text{sfu} \quad , \qquad (35)$$

where f is the frequency in GHz; T, the temperature in keV; and $\tau_{o,x}$, the optical depth, is defined more precisely below. The solar flux unit is defined as 1 sfu = 10^{-22} W m^{-2} Hz^{-1}. To find the emission from an extended source, Equation 35 must be integrated over the projected area, A. The optical depth, τ, is the line-of-sight integral of the absorption coefficient, k, such that $\tau = \int k\, dz$. Those microwave bursts observed to be polarized are nearly always circularly polarized (Magun and Mätzler 1973). If mode-coupling is assumed to be negligible, then the total intensity equals the sum of the intensities in the two modes, each of which is expressed as follows:

$$I_{o,x}(f) = 0.08\, f^2\, T \int_A [1-\exp(-\tau_{o,x})]\, dA \quad \text{sfu} \quad . \qquad (36)$$

The total intensity, I, then equals the sum I_o+I_x. The degree of circular polarization is defined to be $(I_x-I_o)/I$. Equation 36 can be simplified for two limiting cases: $\tau \ll 1$ and $\tau \gg 1$. Thus,

$$I_{o,x}(f) = \begin{cases} 0.08\, f^2\, T\, A & \gg 1 \\ 0.08\, f^2\, T \int_A \tau_{o,x}\, dA & \ll 1 \end{cases} \qquad (37)$$

At intermediate optical depths ($\tau \cong 1$), of course, neither approximation is valid. However, the frequency range over which $\tau \cong 1$ is very narrow, due to the small physical depth of this "skin" between the optically-thick inner volume and the surrounding optically-thin plasma.

To solve for I(f), functional forms for $\tau_{o,x}$ (i.e., $k_{o,x}$) and for dA must be chosen. The absorption coefficients, $k_{o,x}$, incorporate a complex dependence on the plasma temperature; magnetic-field strength; electron density; harmonic number, or f/f_B; and the angle between the line of sight and the magnetic field of the source. The angular

dependence can be eliminated either by assuming that all the emission is in the extraordinary mode, so that the radiation is propagated perpendicular to the field lines (e.g., Dulk, Melrose, and White 1979), or by averaging $k_{o,x}$ over all directions, yielding an average value which is approximately 1/4 of the maximum value (e.g., Mätzler 1978). The following expression for τ is given by Mätzler (1978), for temperatures, densities, and magnetic fields typical of flares:

$$\tau_{o,x} \propto n_e \, z \, (f_{o,x}/f)^{\alpha} \quad , \tag{38}$$

where α is a slow function of T ($\alpha < 10$ for $T > 20$ keV), and $f_{o,x}$, the turnover frequency for the mode of interest, is the frequency at which $\tau_{o,x} = 1$.

The determination of dA as a function of frequency is dependent mainly on the density and magnetic-field gradients within the source, neither of which can be measured at present with adequate temporal and spatial resolution. The choice of source-parameter geometry is at best an intelligent estimate, although the set of physically reasonable cases is limited by theoretical considerations as well as available interferometric and magnetographic solar data. At a given frequency, the projected source area consists of an optically-thick inner region, surrounded by an optically-thin region; as mentioned previously, the boundary between these two components is relatively sharp. Because the brightness of the optically-thin region is smaller, by a factor of τ, than that of the optically-thick part, the integration in Equation 37 can be reduced to the problem of deriving the total optically-thick area at each frequency. For example, Mätzler (1978) defines a monotonically-decreasing distribution function for dA(f) expressing the fractions of the total area with turnover

frequencies in the range $f_{o,x}$ to $f_{o,x}+df_{o,x}$. The form adopted for this distribution function allows certain magnetic-field topologies within the source to be incorporated in the calculated spectra.

Disregarding the dA term for the moment, we now see the general form of the isothermal gyrosynchrotron microwave spectrum: below the turnover frequency, the emission follows the Rayleigh-Jeans expression for black-body radiation, and is proportional to f^2; while at frequencies above the turnover, the flux density follows a power law, decreasing sharply with increasing frequency. The exponent of this power-law fit to the optically-thin part of the spectrum is $(-\alpha+2)$, according to Mätzler (1978); thus, microwave observations at high frequencies could be used to derive α, and hence the source temperature, T (cf. Mätzler 1978; Dulk, Melrose, and White 1979).

Unfortunately, good microwave coverage at frequencies above 15 GHz is sparse, although this situation is being alleviated through recent additions and improvements to receivers at Berne, Nagoya, Toyokawa, and other observatories. A more feasible method of determining the source temperature is by means of spectral fitting to the hard X-ray data (see Section 3.1.1). Coincident hard X-ray and microwave coverage provides a powerful tool for determination of conditions within flaring regions. The areas and temperatures derived for the single-spike bursts, through joint analysis of hard X-ray and microwave data (Crannell et al. 1978), are comparable to the values obtained from high-resolution interferometric observations of impulsive microwave bursts (Alissandrakis and Kundu 1974,1978; Marsh and Hurford 1980; Marsh et al. 1980). One application for coincident data analysis, described fully in Chapter 4, enables the calculation of the magnetic-field

strength within the source, as well as its evolution throughout the flare. This technique is briefly summarized here. The formulae for the total flux, I(f), as presented by Mätzler (1978) or Dulk, Melrose, and White (1979), can be inverted to yield the frequency at which a particular flux is observed. The relationship is simplified greatly by concentrating on the flux at the turnover frequency, which is at or near maximum intensity. Because $\tau_{o,x}=1$ at this frequency, the definition $\tau_{o,x}=k_{o,x}z$, where z is the effective depth along the line of sight, and an analytical expression for $k_{o,x}$ (e.g., Mätzler 1978, Equations 1 and 3) may be used to derive $f_{o,x}$. Total-flux observations include emission from both modes, so, for comparison to observed spectra, it is convenient to introduce the turnover frequency f_T, defined as the arithmetic average of f_o and f_x. The resultant expression for f_T is determined by the source parameters T, B, and $n_e z$ (see Section 4.2). The dependence on the column density is slight, so that adopting a value typical of the lower corona will be sufficient. As previously mentioned, T can be derived from the hard X-ray data. Thus, a simple relationship is obtained between f_T and B. The maximum magnetic-field strength in the flaring region, at a given time, can be found from the observed microwave and hard X-ray spectra. It is crucial, when implementing this procedure, to use simultaneous hard X-ray and microwave spectral information, preferably with comparable temporal resolution.

Contrary to earlier beliefs, a thermal plasma can emit polarized gyrosynchrotron emission. A significant degree of circular polarization can be expected from thermal microwave sources, primarily at high, optically-thin frequencies. For the simple case where the temperature and magnetic field are constant throughout the source and sharp boundaries are assumed, the optically-thick portion of the spectrum will

show no polarization, while the optically-thin part will be highly polarized (up to 90%) in the extraordinary mode. (Mätzler 1978; Dulk, Melrose, and White 1979). In real sources, however, the density may well be non-uniform, the magnetic-field topology may be complex, and edge effects may prove significant. As a result, the degree of polarization observed during a solar burst probably will deviate from the "ideal" case.

3.2.2 Non-thermal Gyrosynchrotron

In Sections 3.1.2 and 3.1.3, the hard X-ray emission from a dilute beam of accelerated electrons was described. These electrons also will emit gyrosynchrotron radiation upon interacting with the ambient magnetic field of the solar atmosphere. The calculation of the gyrosynchrotron emission from a non-thermal electron distribution is considerably more complex than for the thermal case: the directionality of the beam must be considered and, because Kirchoff's Law no longer applies, the emissivities and absorption coefficients must be determined separately. The actual derivation of the emissivity and the absorption coefficients is quite complicated and not directly relevant to the purposes of this thesis. Thus, this section comprises a mostly qualitative discussion, with formulae for useful quantities (such as the total flux density) presented as appropriate. Detailed calculations are given by Takakura (1967), Ramaty (1969), Takakura and Scalise (1970), Trulsen and Fejer (1970), Wild and Hill (1971), and Tarnstrom (1976,1977).

The emissivity for a single electron moving along a helical path, at an arbitrary angle to the magnetic field direction, is a function of the electron energy, the magnetic-field strength, and the pitch angle. For an ensemble of electrons characterized by a known energy

distribution function, the total emissivity is found by summing the discrete contribution from each electron. As a result, the gyrosynchrotron emission from an electron beam does not appear to be made up of discrete lines, as does the single-electron spectrum, but is "smeared out" by line broadening due to the relativistic change of mass at higher electron energies (Bekefi 1966; Takakura 1967). As in the thermal case, the emissivity for each mode, j_o and j_x, must be determined individually. If the line of sight is perpendicular to the magnetic-field direction, the emissivity is zero for the ordinary mode and non-zero for the extraordinary mode; for this reason, some theoretical studies of gyrosynchrotron emission assume this orthogonal geometry, so the extraordinary mode alone can be considered (e.g., Dulk, Melrose, and White 1979). As long as the emitting electrons are only mildly relativistic, the emissivity in the extraordinary mode always exceeds that in the ordinary mode (Holt and Ramaty 1969; Ramaty 1969).

The radiation at low frequencies (harmonic number < 10) can be influenced by several processes: absorption below the plasma frequency, the Razin effect, free-free and gyroresonance absorption by the ambient thermal electrons in the corona, and gyrosynchrotron self-absorption.

Absorption below the plasma frequency was discussed in Section 3.2.1. It was shown that this process only could affect the microwave spectrum significantly if $n_e > 10^{11}$ cm^{-3}, which is higher than the densities typically observed in impulsive microwave burst sources.

The Razin effect is intrinsic to electrons radiating in a background plasma and not in vacuum; for this reason, it is also referred to as "medium suppression". Because the index of refraction in an ionized medium is less than unity, the

emissivity of individual electrons is suppressed, while the corresponding absorption coefficient (for self-absorption) is reduced as well. Hence, the Razin effect and gyrosynchrotron self-absorption are highly interdependent, and must be considered simultaneously in any self-consistent treatment of gyrosynchrotron processes in solar flares. Ramaty and Lingenfelter (1967) and Ramaty (1968) introduced a critical parameter, a, which is a measure of whether or not the low-frequency emission from a particular electron is suppressed. This parameter is defined as

$$a = 1.5\ f_B/f_p \quad , \tag{39}$$

where f_B is the gyrofrequency (Equation 34) and f_p, the plasma frequency (Equation 33). Gyrosynchrotron radiation from an electron of energy Γmc^2 (Γ is the Lorentz factor) is greatly reduced at low frequencies if $a\Gamma < 1$; this condition obtains when either the magnetic field is sufficiently low and/or the density is sufficiently high to produce an appropriate ratio of f_B and f_p (see Equation 39). Furthermore, if $a\Gamma \ll 1$ (low Γ), the total radiated power is strongly suppressed; this results from the combined effects of the Razin mechanism and the small emissivity of mildly-relativistic electrons at high frequencies (Ramaty 1968, 1969).

The effect of Razin suppression on the spectrum as a whole can be expressed in terms of a cut-off frequency, f_R, below which the spectrum is severely modified. This critical frequency depends on source parameters as follows (Ginzburg and Syrovatskii 1965; Ramaty and Petrosian 1972):

$$f_R = 2\times10^{-3}\ n_e/B_\perp \quad \text{MHz}, \tag{40}$$

where $B_\perp$ is the source magnetic-field component perpendicular to the line of sight, in gauss. Although this formula was derived initially for synchrotron radiation by ultrarelativistic electrons, Ramaty (1969) found that this expression agrees with the value of f_R obtained for mildly-relativistic electrons from detailed numerical analysis, to within 10%. Thus, the parameter f_R, defined in Equation 40, is suitable for application to gyrosynchrotron spectra. For the thermal spike bursts studied by Crannell et al. (1978) and Mätzler et al. (1978), the densities and magnetic-field strengths within the emitting regions were found to be of order 10^9 cm^{-3} and 100 G, respectively, corresponding to a Razin cut-off frequency of f_R= 200 MHz. Because this frequency is well below the microwave range, the Razin effect is negligible for these and similar thermal events. For non-thermal sources at greater depths (higher densities) in the chromosphere/corona, the Razin effect does become important. As an example, if $n_e = 10^{11}$ cm^{-3}, as in some soft X-ray bursts, and B = 400 G, then f_R= 5 GHz; those microwave spectra observed to turn over at 5 GHz might originate in the same source as the soft X-ray emission and be dominated at low frequencies by the Razin suppression mechanism.

The absorption coefficient for free-free absorption is a function of frequency, source temperature, and electron density. As was done to evaluate the effects of Razin suppression, the free-free absorption can be characterized by a critical frequency, f_{br}, below which the spectrum is strongly absorbed by this process. Thus, after Ramaty and Petrosian (1972):

$$f_{br} = 2\times10^{-12}\ (EM)^{0.5}/T^{0.75}\ A^{0.5} \quad \text{MHz} , \qquad (41)$$

where the emission measure $EM = n_e^2 V$ in cm^{-3} (see Section 3.1.1), V being the volume in cm^3; T, the temperature in

keV; and A, the projected area of the source in cm^2 (where it is assumed that V=AL, L being the linear depth of the source). For typical spike-burst parameters ($EM=5x10^{45}$ cm^{-3}, T=32 keV, and $A=5x10^{17}$ cm^2), Equation 41 yields $f_{br} \cong 15$ MHz. Therefore, we conclude that free-free absorption within these thermal sources is negligible at microwave frequencies. Since the cut-off frequency for free-free absorption is inversely related to temperature, however, this process can become significant if the lower-temperature medium in or around the emitting region , such as the corona, is considered. This is of particular interest in non-thermal models, wherein the flare region comprises a dilute beam of high-energy electrons immersed in the ambient solar chromosphere/corona. To illustrate: if typical values for source density, $n_e \sim 10^{10}$ cm^{-3}, and size, $L \sim 5x10^9$ cm, are assumed, we can derive the temperature for which the free-free cut-off is located at a particular microwave frequency. For $f_{br}=5$ GHz, a commonly observed turnover frequency, Equation 41 yields $T \cong 2x10^6$ K (~0.2 keV), a reasonable value for the quiescent corona. Soft X-ray burst observations generally yield temperatures an order of magnitude higher (cf. Svestka 1976), however, and the presence of significant amounts of lower-temperature gas within the microwave-producing regions of flares has not been established. Analyses of soft X-ray line data also yield density estimates which greatly exceed those derived from microwave and hard X-ray coverage, by as much as 4 orders of magnitude (Svestka 1976; Doschek and Feldman 1979). Consequently, the role of free-free absorption in non-thermal microwave spectra is far from clear. This problem is reflected in the literature: for example, Holt and Ramaty (1969) state that free-free absorption is negligible, while Ramaty and Petrosian (1972) suggest that this process may be the dominant absorption mechanism, particularly for the small class of spectra which are "flat" above the turnover frequency.

Gyroresonance absorption by the ambient thermal electrons strongly influences the spectral shape at low frequencies. As noted in the previous section, both the ordinary and extraordinary modes are absorbed at the fundamental and second harmonic of the gyrofrequency, while only the extraordinary mode is absorbed at the third harmonic. The absorption coefficient is dependent on the temperature and density of the thermal electrons, as well as the magnetic field in the region; for bursts with high temperatures ($T > 10^7$ K) and densities ($n > 10^{10}$ cm^{-3}), absorption of extraordinary mode radiation at the fourth harmonic also may occur (Ramaty and Petrosian 1972). Because most microwave observations do not distinguish between ordinary and extraordinary-mode radiation, a single frequency is defined in order to evaluate the effects of gyroresonance absorption on the total-power spectrum. This critical frequency, f_g, is defined as the highest frequency at which gyroresonance absorption can modify the spectrum. Thus,

$$f_g = 3 - 4\ f_B$$
$$= 8.4 - 11.2\ B \quad \text{MHz} \quad , \qquad (42)$$

(Takakura 1972; Ramaty and Petrosian 1972). A turnover frequency of 5 GHz would imply $B \sim 450$-600 G in the source region, assuming that thermal gyroresonance is the dominant absorption mechanism.

Gyrosynchrotron self-absorption was introduced briefly in the previous section. For the thermal case, the emissivity and the absorption coefficient are related by Kirchoff's law for the optically-thick portion of the spectrum, so that the self-absorption coefficient is known if the emissivity is provided. The non-thermal case is considerably more complicated, as mentioned at the beginning of this section. The assumption of a power-law electron number (or energy)

spectrum enables numerical solution of the equations for the self-absorption and emissivity (Holt and Ramaty 1969; Ramaty 1969). Under this assumption, the coefficient for self-absorption is a function of: the magnetic-field strength, density, and area of the emitting region; the spectral index of the electron spectrum and the anisotropy, if any, of the electron pitch-angle distribution (cf. Ramaty 1969); the angle between the magnetic field and the line of sight; and the frequency of observation. Models which incorporate a non-uniform magnetic field within the emitting region (e.g., Takakura and Scalise 1970; Kovalev and Korolev 1976; Mätzler 1976; Böhme et al. 1977) require, in addition, a dependence on the magnetic-field geometry. For comparison with competing absorption mechanisms and with observations, we adopt simple source conditions (no anisotropy and uniform magnetic field) and determine the critical frequency, f_{sa}, below which the spectrum is absorbed significantly by gyrosynchrotron self-absorption. Ramaty and Petrosian (1972) conclude that, for non-thermal source parameters typical of solar bursts, the value of f_{sa} derived by numerical analysis (Ramaty 1969) can be reasonably approximated by the following expression, originally formulated for relativistic synchrotron sources (Slish 1963; Tucker 1976):

$$f_{sa} = 2.8 \times 10^{-2} B^{0.2} (I_m/\theta)^{0.4} \quad \text{MHz} , \qquad (43)$$

where I_m is the maximum flux density of the source in solar flux units, and θ, the angular size of the source in radians (cf. also Guidice and Castelli 1975). Thus, for source parameters $B \sim 200$ G, $I_m \sim 100$ sfu, and $\theta \sim 10^{-9}$ (e.g., Marsh et al. 1980), $f_{sa} \cong 2$ GHz.

Constraints can be placed on the choice of absorption mechanism active in individual bursts through inspection of

the spectral slope at low frequencies, for which $\tau >> 1$ (cf. Guidice and Castelli 1975). Each absorption process yields a characteristic slope, under ideal conditions, as listed in Table 3-2; the spectral slope, **m**, is defined such that the flux density is proportional to f^m, for the optically-thick regime.

TABLE 3-2

SPECTRAL CHARACTERISTICS OF ABSORPTION PROCESSES

Process	m	References
free-free	2	Castelli et al. 1974, Guidice and Castelli 1975
thermal gyroresonance	>3	Castelli et al. 1974
gyrosynchrotron (self)	$\geq$2.5	Ramaty and Petrosian 1972, Guidice and Castelli 1975

In principle, the observed slope of the optically-thick portion of the spectrum, in conjunction with the critical frequencies defined above for each process, can be used to determine the dominant absorption mechanism for a particular event. For most bursts, however, two or more absorption processes are found to fit the observational requirements equally well. If the source size and density, as well as the strength and geometry of the magnetic field within the source were known by independent means, then the relevant absorption process or processes could be identified with certainty. Since this information is unavailable for the majority of microwave bursts, empirical studies of the low-frequency spectrum have been concentrated on statistical surveys, searching for trends toward a particular value of the observed slope. Schöechlin and Magun (1979) recently analyzed 106 microwave burst spectra, and found that the most frequent value of the low-frequency spectral index is 1.4. This slope is inconsistent with all non-thermal models, and best characterizes an optically-thick, thermal

source with temperature and magnetic-field inhomogeneities in the source boundary. Schöechlin and Magun also find a minor peak in the distribution of spectral indices at 2.5, in agreement with Guidice and Castelli (1975). This peak probably is due to a small class of non-thermal events, and can be explained in terms of self-absorption of emission by a power-law electron distribution.

Anisotropy in the propagation of the electron beam further complicates the issue of absorption mechanisms, by producing directivity in the emissivity which is indistinguishable from absorption dependent on viewing angle; the self-absorption becomes anisotropic as well. Non-uniform magnetic field configurations also have been shown to affect spectral shape, by varying both the emissivity and the absorption coefficients with position in the source region. Most models of this sort assume a magnetic field which decreases with height above the photosphere and with distance from the central source of the field. Both half-dipole (e.g., Takakura and Scalise 1970) and bipolar (e.g., Mätzler 1976) geometries have been considered, as counterparts to the observed coronal loops which appear to track the magnetic fields in the solar atmosphere.

The differential microwave flux in each mode, $dS_{o,x}(f)$, is given by the following expression (Takakura and Scalise 1970):

$$dS_{o,x}(f) = (1/R^2)\ j_{o,x} \exp(-\tau_{o,x})\ dV \quad , \qquad (44)$$

where $j_{o,x}$ is the emissivity for the ordinary or extraordinary mode; R, the Earth-Sun distance (1 AU); $\tau_{o,x}$, the mode-dependent optical depth, as defined previously; and dV, the volume element. The emissivity and optical depth

are functions of frequency, while for non-uniform magnetic-field geometries, dV also depends on frequency (cf. Kovalev and Korolev 1976).

For the ideal, homogeneous case, this equation simplifies in the limits of $\tau \ll 1$ and $\tau \gg 1$, and can be integrated easily to find the total flux:

$$S_{o,x}(f) = \begin{cases} (1/R^2)\ j_{o,x}\ V & \tau \ll 1 \\ (1/R^2)\ j_{o,x} \int \tau_{o,x}\ dV\ , & \tau \gg 1 \end{cases} \qquad (45)$$

where V is the source volume. At very high frequencies, the spectral shape simply reflects the emissivity shape; a power-law electron spectrum thus yields a power-law microwave flux spectrum in the optically-thin regime. Unfortunately, this ideal case only applies to a limited portion of the spectrum, and cannot accomodate non-uniform magnetic-field configurations.

Kundu and Vlahos (1979) have interpreted the observed spectral and polarization characteristics of impulsive microwave bursts in terms of an inhomogeneous source structure, assuming an asymmetric, bipolar magnetic loop, in which the microwave-emitting electrons are contained. Kundu and Vlahos adopt the analytical formalism for dV derived by Kovalev and Korolev (1976), plus the formulae for $j_{o,x}$ and $\tau_{o,x}$ given for non-thermal sources by Takakura and Scalise (1970) and Takakura (1972), for determination of the total microwave flux originating in a source of non-uniform magnetic field. Substitution of these expressions into Equation 45 and subsequent integration yield the following expression for the total flux in either mode:

$$S_{o,x}(f) = (1/R^2)\ G\ (f/f_{B_{max}})^k \int_{m_1}^{m_2} m^{-k+1}\ j_{o,x}(m)\ \exp[-\tau_{o,x}(m)]\ dm, \qquad (46)$$

where G is a function of the source area and maximum height, the ratio of the maximum and minimum magnetic-field strengths, and the arbitrary constant, k, which essentially describes the divergence of the field lines; $f_{B_{max}}$, the gyrofrequency for the maximum magnetic field within the source; $m = f/f_{B_{max}}$; and the limits of integration, m_1 and m_2, depend on f, $f_{B_{max}}$, and $f_{B_{min}}$ (Kovalev and Korolev 1976; Kundu and Vlahos 1979, Appendix I). The total flux, S(f), is $S_o(f)+S_x(f)$, and the degree of polarization is $(S_x-S_o)/S$. Kundu and Vlahos explain the polarization structure and time evolution of the source in terms of the relative field strengths at the footpoints of the loop, and find qualitative agreement with observations. However, the qualitative nature of this work precludes critical evaluation of the model until quantitative predictions are provided.

Unlike the thermal case, non-thermal gyrosynchrotron emission is polarized intrinsically in both the optically-thick and optically-thin regions of the spectrum. In an optically-thick thermal source, the radiation intensity is the same in both modes (by Kirchoff's Law), whereas in an optically-thick non-thermal source, the ordinary mode radiation dominates (Ramaty 1969). In both cases, the extraordinary mode radiation prevails throughout the optically-thin portion of the spectrum. Assuming a single non-thermal source, Holt and Ramaty (1969) attribute the reversal of polarization at some frequency, observed in most microwave bursts (Kundu 1965), to the transition from the optically-thick to the optically-thin regime. The polarization reversal also could be due to selective absorption by the thermal gyroresonance process (see above), according to Takakura (1967). Thus, this polarization phenomenon cannot be unambiguously interpreted as support for either hypothesis. As always, the determination of

polarization can be complicated further by the introduction of multiple source regions (e.g., a bipolar loop emitting from either or both footpoints), non-uniform magnetic-field geometry (e.g., an asymmetric loop), and/or density inhomogeneity within the source.

3.2.3 Trap and other "Combination" Models

The basic features of non-thermal and quasi-thermal trap models were discussed in Section 3.1.4. In general, such models include a population of energetic electrons contained within a magnetic loop, the footpoints of which are rooted in the photosphere. Most of the microwave emission observed during impulsive events comes from electrons with energies above 100 keV (Holt and Ramaty 1969), depending on the number of electrons at these high energies (i.e., on the spectral index of the electron distribution). In contrast, the associated hard X-ray emission originates primarily in electrons in the energy range from 10 to 100 keV (cf. Section 3.1). Therefore, the electrons producing simultaneous hard X-ray and microwave radiation could constitute a common distribution function, but would occupy contiguous energy ranges.

The effects of this separation become particularly important in trap models, because the highest energy electrons are expected to precipitate out of the trap and down the legs of the loop (Melrose and Brown 1976; see also Section 3.1.4). According to the quasi-thermal model proposed by Brown, Melrose, and Spicer (1979), the primary energy release at the top of the loop causes bulk energization of the local plasma; the resultant turbulence causes the formation of ion-acoustic conduction fronts, which propagate slowly towards the footpoints. Electrons with energies greater than $3v_{th}$, where v_{th} is the electron thermal velocity in the energy-release region, will escape

through the conduction fronts. If the electrons in the heated plasma assume a Maxwellian velocity distribution characterized by temperature $T \sim 3 \times 10^8$ K, then all electrons with kinetic energies above 200 keV will precipitate out of the energy-release region. These electrons will retain the steep slope characteristic of the original Maxwellian, unless subjected to further acceleration within the precipitation zones (cf. Vlahos 1979, Chapter 4). In a non-thermal trap, as discussed in Section 3.1.4, the energy spectrum of the precipitating electrons remains a power law, although collisional processes will change the spectral index. The existence of a non-thermal component in the source region can be deduced potentially by inspection of the observed microwave spectrum, from the presence of an optically-thin spectral index much flatter than would be expected from the high-energy portion of a Maxwellian (assuming temperatures typical of impulsive bursts). This diagnostic can be misleading, however, because the presence of a steep gradient in the magnetic field within the source region can reduce the steepness of the associated microwave spectrum above the turnover frequency (cf. Kovalev and Korolev 1976 for examples).

At present, the available data do not lend unambiguous support to either the non-thermal or thermal versions of trap models. Observations at frequencies above 20 GHz are rare, so that the slope of the optically-thin spectrum has not been measured for the majority of bursts. The poor coverage of the millimeter-wave region has been improved at several observatories within the past few years; as yet, the paucity of impulsive flares in these pre-solar-maximum years has prevented statistical studies of the properties of burst spectra in the optically-thin regime. It is to be hoped that coverage during and after the Solar Maximum Year will contribute enormously to our understanding of the emission

mechanisms involved in microwave events, as well as the energy distribution of the emitting electrons themselves.

Chapter 4

SPECTRAL EVOLUTION OF MULTIPLY-IMPULSIVE BURSTS

The impulsive phase provides the most direct evidence available for the role of energetic electrons in solar flares (Kane 1974). In order to study these electrons, and thereby the physical processes responsible for their acceleration, observations which determine both temporal and spatial features of impulsive emissions are required. Of particular significance is the location of the sources with respect to the magnetic-field topology of the active region. The different dependences of the hard X-ray and microwave emission on source properties such as electron density, magnetic-field strength, and temperature or spectral index (see Chapter 3) enable these source parameters to be determined and their evolution to be followed throughout an impulsive event. Each set of source properties can be utilized to locate the emitting region in the solar atmosphere, by means of extant models of density and magnetic-field strength as a function of height above photospheric active regions. The results of such an analysis provide information on the evolution of the spatial characteristics of the impulsive flare source and further clues as to the basic mechanisms of the flare process. In the current absence of direct, hard X-ray images of flares, this is one of the few methods by which the relative positioning of impulsive hard X-ray burst sources can be estimated.

According to the research reported here, the multiply-impulsive solar bursts do not comprise a homogeneous set of events. Rather, they fall into two categories according to their spectral characteristics: those events for which the

measured values of the microwave turnover frequency and electron temperature yield the same magnetic-field strength for the source of each peak within a burst; and those events which demonstrate significant differences between the magnetic-field strengths of the sources of different peaks within a burst, as deduced from variations in turnover frequency and temperature. These two classes of spectral behaviour are interpreted as evidence for two types of spatial structure in impulsive bursts: events whose component spikes apparently originate in one location, and events in which groups of spikes appear to come from separate regions which flare sequentially. Although the concept of separate regions contributing to a complex flare has been discussed by many authors (e.g., Hagen and Neidig 1971; Zirin and Tanaka 1973; Alissandrakis and Kundu 1975; Vorpahl 1976), the present work is the first analysis showing both hard X-ray and microwave evidence for the existence of these discrete flaring sites within the regions producing multiply-impulsive bursts.

The analysis of the selected set of multiple-spike bursts is described in Section 4.1. In Section 4.2, the division of these events into two classes according to the evolution of spectral properties and magnetic-field strength is discussed, and specific examples of each type are presented. The conclusions drawn from this research are presented in Section 4.3, and the results are evaluated in the context of observations and current theoretical predictions.

4.1 DATA ANALYSIS

A total of 66 multiply-impulsive solar flares have been identified in the OSO-5 hard X-ray spectrometer data. The properties of the instrument are described in detail in Chapter 2. These events were chosen for their apparent impulsive nature, according to the following morphological criteria:

1) Maximum count rate greater than or equal to 280 counts s^{-1};
2) Successive peaks which are distinctly separable, with rapid rise to and fall from an intensity at least 3σ above noise;
3) No apparent gradual component immediately before, during, or after the impulsive event, above 15% of the maximum flux.

Microwave data were collected for as many events as possible from Sagamore Hill, Bern, and other ground-based observatories.

Interest in these events was sparked by the resemblance of the component spikes to the simple impulsive "spike bursts" discussed by Crannell et al. (1978). The time-intensity profiles of the multiple-spike bursts appear to consist of groups of overlapping spikes; thus, it seemed worthwhile to look more deeply for evidence of fundamental structures corresponding to the individual spikes within each event. For the simple spike bursts, Crannell et al. found that the microwave and hard X-ray emissions during each time interval are consistent with a common origin in the same localized population of energetic electrons. Similarly, for the analysis of the multiple bursts we have assumed that, at each moment, the hard X rays emanate from the same source as the microwaves. As is shown in the following sections, however, this common source may or may not be found at the same location throughout an entire event.

Twenty events were observed to have sufficiently intense hard X-ray emission and coincident microwave coverage with sufficiently good time resolution to allow a detailed study of the spectral evolution throughout each event. The major peaks of each burst were identified in the hard X-ray time-

intensity profiles. Least-squares fits were performed for each spectrum, to both single power-law and isothermal forms. For many of the multiple bursts, including those discussed in detail in Section 4.3, the X-ray spectra of the major peaks are much better fitted by single-temperature thermal distributions.

Microwave spectra were obtained for the times corresponding to the X-ray peaks within each event. The Sagamore Hill and Bern records, the primary sources of microwave data, provided flux measurements with uncertainties of at most ±10%. The temporal resolution is approximately 3 s for the Sagamore Hill data and 0.1 s for the Bern data. Records with poorer time resolution were given lower weight. The turnover frequency f_T, the frequency at which the spectrum changes from being optically thick to optically thin (see Section 3.2.1), was determined empirically by inspection of each microwave spectrum. Then the following procedure for finding the ambient magnetic-field strengths from the properties of the microwave spectra was applied.

The magnetic-field strength corresponding to each peak within an event was calculated according to the following formula, taken from the work on gyrosynchrotron radiation from a thermal population of electrons by Mätzler (1978) (see also Section 3.2.1):

$$f_T = f_B(5.8+0.406T)\ (2.5\times10^{-26}\ n_e z/B)^{1/(\gamma+2)}\ \text{MHz}\ , \qquad (47)$$

where f_B is the local cyclotron frequency in MHz (Equation 34); T, the source electron temperature in keV, as derived from the hard X-ray spectrum; $n_e z$, the column density in cm^{-2}; B, the ambient magnetic-field strength in gauss; and γ, the high-frequency (very optically thin) slope of the

microwave spectrum, such that $I \propto f^{-\gamma}$ ($\alpha=\gamma+2$; see Section 3.2.1). The microwave spectral slope, $\gamma=6$, was determined by inspection of several microwave spectra. The value adopted for the column density, $n_e z=4\times10^{17}$ cm^{-2}, is typical of the relevant region of the solar atmosphere (Mätzler 1978). The accuracy of these estimates is quite adequate, because Equation 47 is only weakly dependent on both quantities.

For the parameter values given above, the magnetic-field strength depends on the electron temperature and the turnover frequency according to the following relationship:

$$B = 2.2\times10^{-8} \left[f_T / (5.8+0.406T) \right]^{1.14} \quad G \quad . \qquad (48)$$

It is crucial to note that, without the temperature derived from the hard X-ray spectrum, it would be impossible to determine the magnetic-field strength for each peak. The microwave spectra alone are not sufficient to distinguish whether peak-to-peak changes in the observed turnover frequency indicate changes in the magnetic field or simply reflect changes in the temperature of the source electrons.

The event of 1970 March 26 provides a striking illustration of the necessity for both hard X-ray and microwave data. The spectrum, shown in Figure 4-1, exhibits a marked shift to higher turnover frequency at 1728.3 UT, the peak of highest flux during the burst. However, the X-ray analysis shows that this peak also exhibits the highest temperature, 73 keV, as compared to the values derived for the other 3 peaks, 34-45 keV. As a result, the magnetic-field strength is comparable for all 4 peaks. Without the temperatures provided by the hard X-ray spectra, the change in turnover frequency might be mistakenly interpreted as a shift to higher field strength.

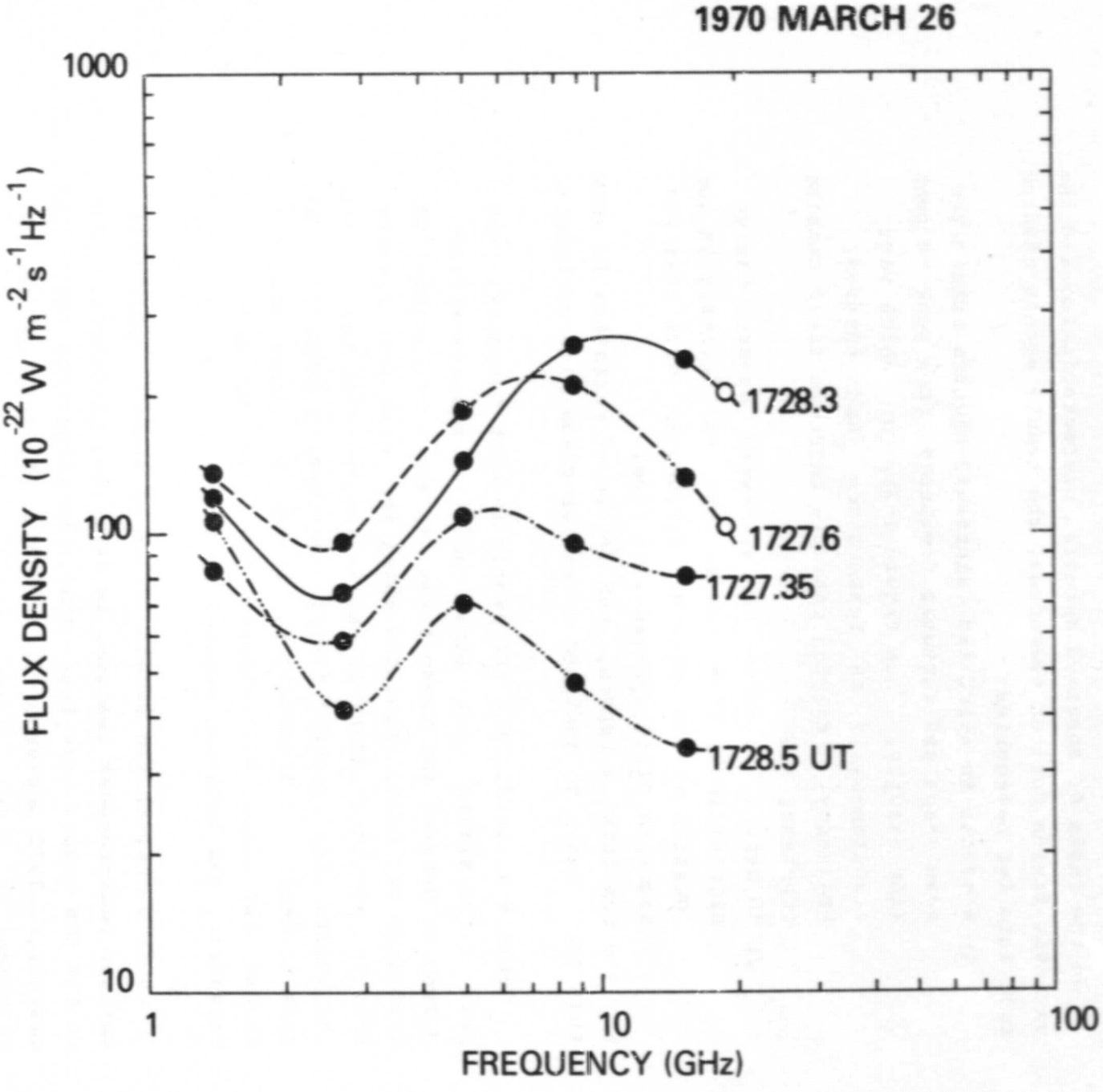

Figure 4-1. Microwave spectra at the times of peak intensity during the multiply-impulsive event of 1970 March 26.

4.2 RESULTS

On the basis of observed spectral characteristics and the magnetic fields derived therefrom, the twenty events studied fall into two categories:

1) 8 events in which the microwave spectra retain the same shape and turnover frequency from peak to peak (for example, see Figure 4-2), or which vary simultaneously in temperature and turnover frequency, implying that the magnetic field remains constant; and
2) 10 events in which the microwave spectra change significantly from peak to peak, particularly in the location of the turnover frequency, such that the magnetic field changes with time.

For the remaining 2 bursts, the degree of variation is such that they cannot be assigned to either class with certainty.

Table 4-1 lists, for the events in each category, the peak times within each burst and the magnetic-field strengths derived for these times by means of Equation 48. The range of field strengths shown for each peak results from the ±1-sigma uncertainties in the best-fit temperature. The events with spectral shapes that remain unchanged from peak to peak are discussed in Chapter 5, where possible causes for their multiplicity are suggested and one candidate, the betatron mechanism, is critically analyzed.

In this chapter the second class of events, those with obvious peak-to-peak changes, is described in detail. Two of the ten events have been chosen to illustrate the second category: 1970 September 8, 1228-1233 UT, and 1969 May 29, 1938-1944 UT. These bursts contain the largest number of clearly separable peaks, thus providing the largest number

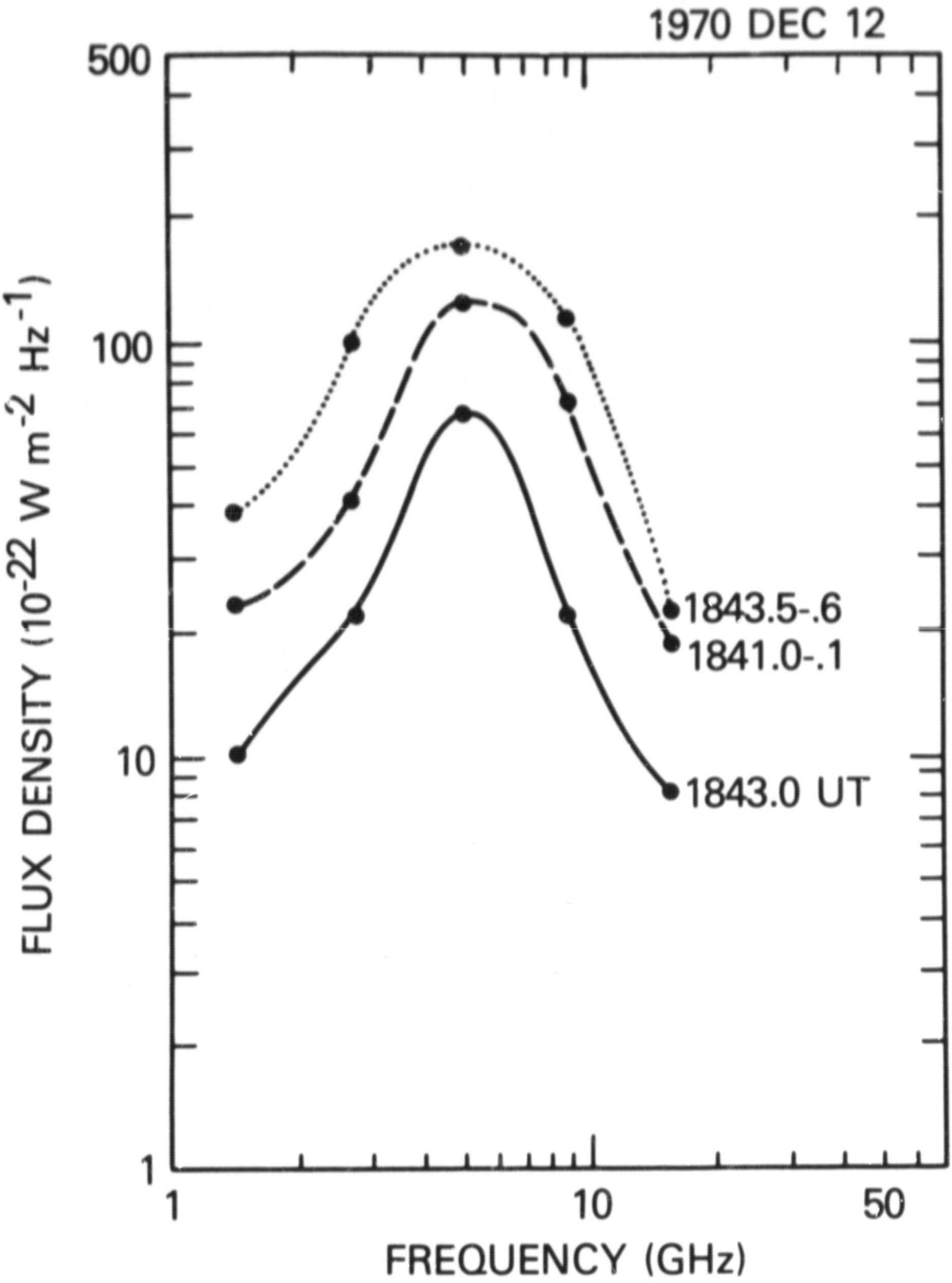

Figure 4-2. Microwave spectra at the times of peak intensity during the multiply-impulsive event of 1970 December 12. Note the consistency of spectral shape and turnover frequency.

TABLE 4-1

CLASSIFICATION OF BURSTS BY MAGNETIC-FIELD EVOLUTION

Date	Peak Time (UT)	B (gauss)	
Constant Field Strength			
1969 August 11	1219.7	62.3 - 72.4	
	1219.95	60.5 - 69.3	
	1220.2	67.5 - 76.8	
1969 November 5	1759.9	33.6 - 57.3	
	1800.15	45.9 - 64.5	
	1801.2	56.9 - 78.5	
1970 March 1	1400.2	49.2 - 53.6	
	1400.55	60.4 - 70.6	
	1400.8	56.9 - 70.5	
	1401.7	51.1 - 60.3	
	1402.0	42.4 - 63.3	
1970 March 26	1727.35	66.8 - 77.7	
	1727.6	63.2 - 71.7	
	1728.3	64.5 - 75.3	
1970 July 23	1046.3	78.4 - 111.6	
	1046.6	98.8 - 130.3	
1970 December 12	1840.8	51.2 - 71.0	
	1841.3	56.8 - 71.7	
	1843.5	68.9 - 79.3	
1970 December 13	1832.0	44.9 - 62.6	
	1832.2	31.7 - 53.9	
	1832.5	26.4 - 55.1	
1971 August 22	0751.2	73.0 - 82.8	
	0751.7	71.3 - 84.1	
Variable Field Strength			
1969 March 31	1159.15	42.1 - 66.0	115.3 - 180.6
	1159.3	36.1 - 48.8	115.5 - 156.4
	1159.6	27.8 - 44.3	91.7 - 146.4
	1159.8	31.2 - 67.4	102.9 - 222.7
1969 April 26	2303.2	76.8 - 88.9	
	2303.5	100.3 - 110.7	
	2303.8	80.4 - 86.2	
	2304.5	100.3 - 110.0	
	2306.15	62.6 - 72.8	
	2306.75	50.1 - 54.6	
	2307.4	45.3 - 58.5	
1969 May 29	1938.6	51.1 - 65.8	
	1938.9	47.9 - 61.4	
	1939.4	35.6 - 55.3	
	1941.95	66.0 - 71.7	160.6 - 174.4
	1942.15	55.2 - 62.9	144.3 - 164.2
	1942.4	73.1 - 85.2	207.7 - 242.2
	1942.5	64.7 - 71.4	183.8 - 203.0
	1943.1	(140 - 220)*	
1969 December 20	2013.55	80.4 - 131.3	
	2013.7	21.9 - 47.2	

C-2

1970 May 29	1120.5	≤ 81.0	
	1120.8	144.3 - 238.2	
	1122.1	29.7 - 37.2 ; 138.4 - 173.8	
	1122.65	25.3 - 42.2 ; 116.6 - 205.2	
	1126.7	35.9 - 75.6	
	1127.15	62.4 - 81.2	
	1127.7	63.1 - 78.6	
1970 June 28	2000.8	81.3 - 94.8	
	2001.35	93.1 - 104.4	
	2001.95	116.6 - 128.3	
	2002.2	114.2 - 126.2	
	2002.5	91.5 - 102.0	
	2003.65	88.7 - 98.4	
	2004.6	139.6 - 155.0	
	2004.95	81.7 - 89.6	
	2009.6	49.1 - 67.5	
1970 July 23	1839.95	91.5 - 114.4	
	1840.8	156.0 - 191.2	
	1841.5	158.8 - 184.7	
	1841.8	138.8 - 173.6	
	1842.2	167.9 - 205.8	
	1843.25	130.5 - 141.2	
	1843.5	118.6 - 128.5	
	1844.2	100.8 - 113.7	
	1844.4	94.5 - 106.8	
	1844.5	96.3 - 104.4	
	1845.15	78.1 - 88.9	
1970 September 8	1229.1	84.4 - 141.9	
	1229.35	100.0 - 130.2	
	1229.5	115.2 - 136.3	
	1229.65	≥ 173.8 - 205.2	
	1229.95	58.2 - 82.1	
	1230.8	68.6 - 80.4	
	1231.4	73.8 - 87.7	
	1231.55	77.2 - 90.2	
	1231.7	72.3 - 84.3	
1971 May 3	1412.5	30.1 - 43.3 ; 118.7 - 170.8	
	1412.8	127.3 - 152.3	
	1413.4	151.1 - 165.8	
	1413.7	(45.7 - 54.5) ; 124.1 - 147.7	
1971 August 21	0934.5	34.3 - 40.7	
	0934.9	82.9 - 95.2	

---

* No X-ray coverage at this time (see text).

of reliable hard X-ray and microwave spectra. The parameters characterizing these two bursts are presented in Table 4-2, which lists for each peak within the bursts the time of the X-ray peak; the hard X-ray flux from 14 to 254 keV; the flux at the peak of the microwave spectrum; the turnover frequency f_T; the best-fit temperature and emission measure of the hard X-ray spectrum and the reduced chi-squared of the fit; and the corresponding magnetic-field value, derived from f_T and T as described in Section 4.2.

TABLE 4-2

OBSERVED AND DERIVED X-RAY AND MICROWAVE PARAMETERS

Peak Time (UT)	X-Ray Flux 14-254 keV (photons cm^{-2} s^{-1} keV^{-1})	Microwave Flux Density at f_m (sfu)	f_T (GHz)	T(keV)	EM (10^{45} cm^{-3})	Reduced χ^2	B (gauss)
1970 September 8							
1229.1	0.028	32	9	52.1	0.05	0.11	84.4-141.9
1229.35	0.109	85	10.5	62.6	0.12	0.38	100.0-130.2
1229.5	0.097	~115	10	44.0	0.25	0.99	115.2-136.3
1229.65	0.106	>125	>13	47.3	0.28	0.54	>173.8-205.2
1229.95	0.043	58	6	53.5	0.09	0.37	58.2-82.1
1230.8	0.055	68	5	39.4	0.16	0.34	68.6-80.4
1231.4	0.053	161	4	25.6	0.26	2.65	73.8-87.7
1231.55	0.117	156	5	34.2	0.44	1.08	77.2-90.2
1231.75	0.095	140	~4	26.9	0.45	1.35	~72.3-84.3
1969 May 29							
1938.6	0.089	94	4.8	50.2	0.20	1.53	51.1-65.8
1938.9	0.094	130	5.0	56.0	0.19	1.48	47.9-61.4
1939.4	0.048	62	4.3	56.4	0.11	5.36	35.6-55.3
1941.95	0.305	290;390	5.5;12.0	49.1	0.66	1.02	66.0-71.7;160.6-174.4
1942.15	0.351	380;530	5.6;13.0	59.5	0.56	1.31	55.2-62.9;144.3-164.2
1942.4	0.166	240;310	5.0;12.5	36.6	0.50	0.91	73.1-85.2;207.7-242.2
1942.5	0.192	170;390	5.0;12.5	43.9	0.48	0.80	64.7-71.4;183.8-203.0
1943.1[a]	-----	700	12	(36-60)	----	----	(140-220)

[a] No X-Ray coverage at this time (see text)

The hard X-ray time-intensity profiles in the nine energy channels between 14 and 254 keV for the September 8 event are shown in Figure 4-3. The microwave records of this event at 5 and 15.4 GHz, obtained by Sagamore Hill, are shown in Figure 4-4. The different phases of microwave spectral evolution, shown in Figures 4-5a, 4-5b, and 4-5c, are denoted in Figures 4-3 and 4-4 by the sections labeled "a", "b", and "c", respectively. In phase "a" the turnover frequencies range from 9 to $\geq$13 GHz. The spectrum seen at 1229.65 UT appears to increase monotonically with frequency, up to the highest observed frequency, 15.4 GHz. This spectrum also could consist of two components, however, as would result from adding the spectra resembling those of the preceding and following peaks (at 1229.5 and 1229.95 UT). Although the high-frequency portions of the spectra differ in slope, the turnover frequencies both lie between 4 and 6 GHz in the next two phases. The inferred magnetic-field strengths range from B $\geq$ 120 G in phase "a" to about 75 G in the later phases, as detailed in Table 4-2.

The event of 1969 May 29 exhibits spectral changes which differ qualitatively from those of the September 8 event, but which lead to similar conclusions. The hard X-ray and the microwave time studies of this burst, shown in Figures 4-6 and 4-7, are divided into phases "a", "b", and "c" corresponding to the microwave spectra shown in Figures 4-8a, 4-8b, and 4-8c. During phase "a", the turnover frequencies are approximately 4.5 GHz. In the next phase, however, a "double-humped" structure appears in each of the microwave spectra, for which two turnover frequencies can be found: 5-5.6 and 12-13 GHz. The existence of two turnover frequencies for each peak in this phase is equally consistent with source parameters of two magnetic fields or two temperatures or both. Because a two-temperature distribution can be neither ruled out nor verified on the

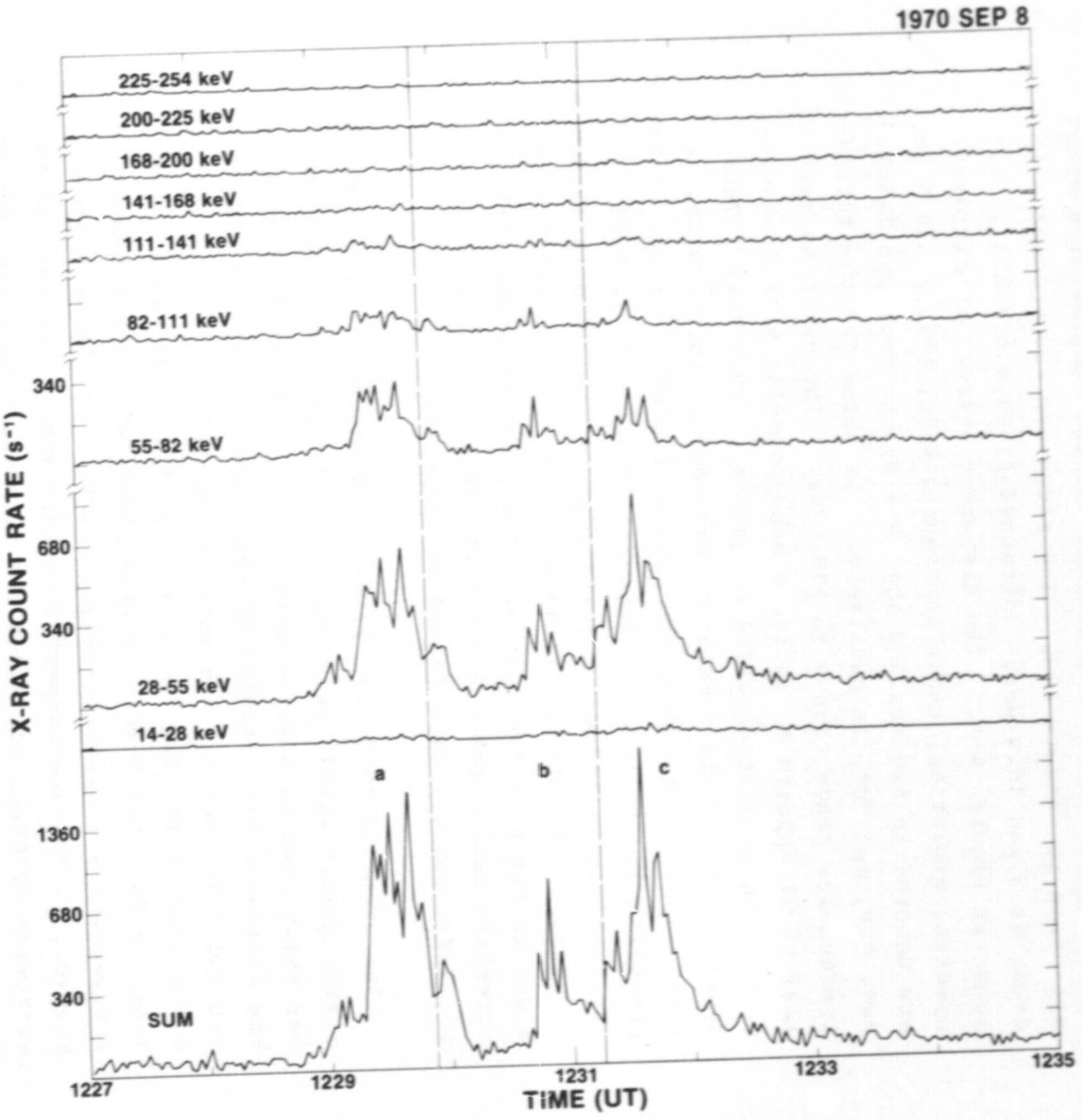

Figure 4-3. Hard X-ray time-intensity profiles for the multiply-impulsive event of 1970 September 8. Profiles labeled "a", "b", and "c" correspond to the phases of microwave spectral evolution shown in Figures 4-5a, 4-5b, and 4-5c.

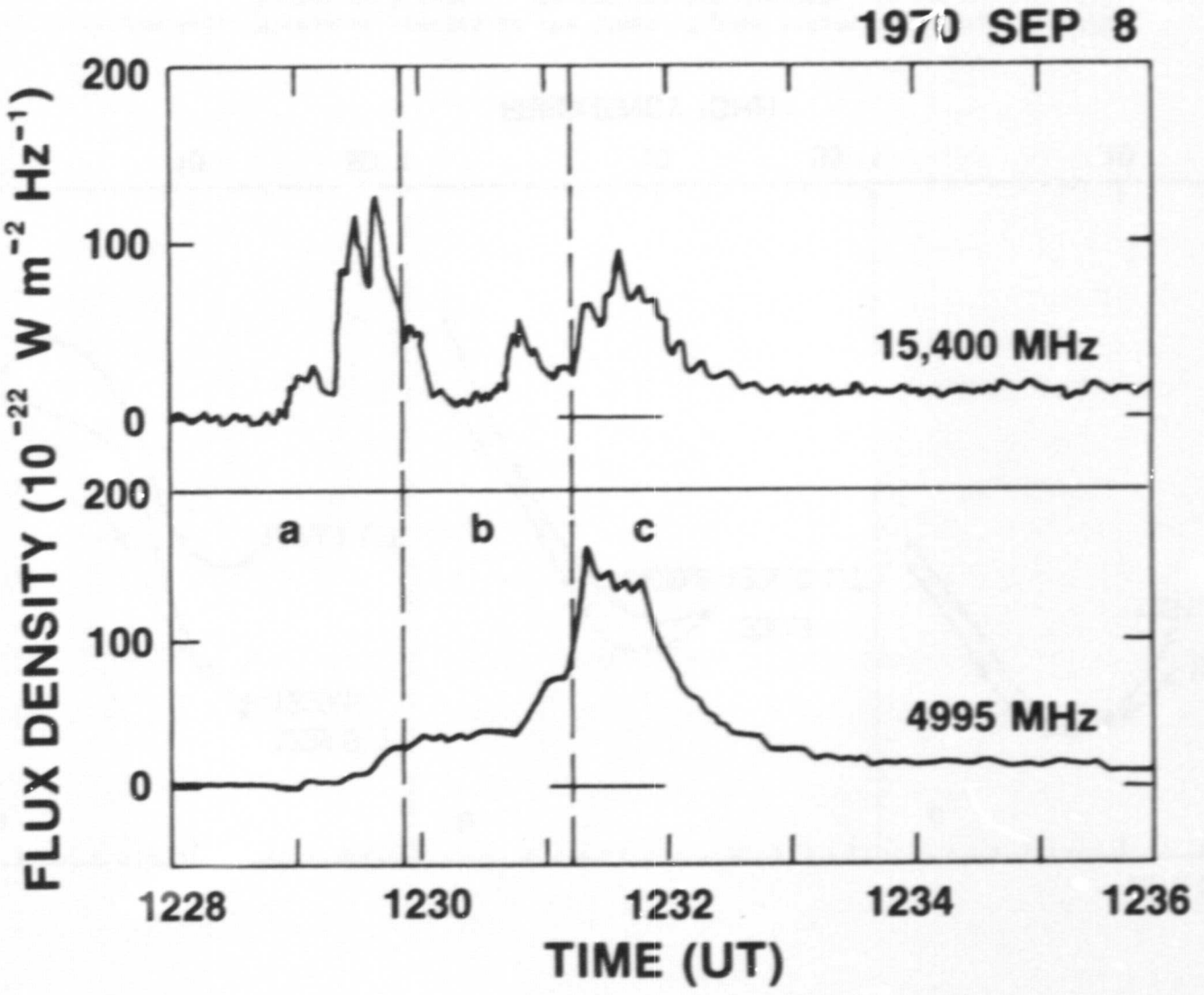

Figure 4-4. Microwave time-intensity profiles at 4995 and 15,400 MHz for the 1970 September 8 event. Portions labeled "a", "b", and "c" correspond to Figures 4-5a, 4-5b, and 4-5c, respectively.

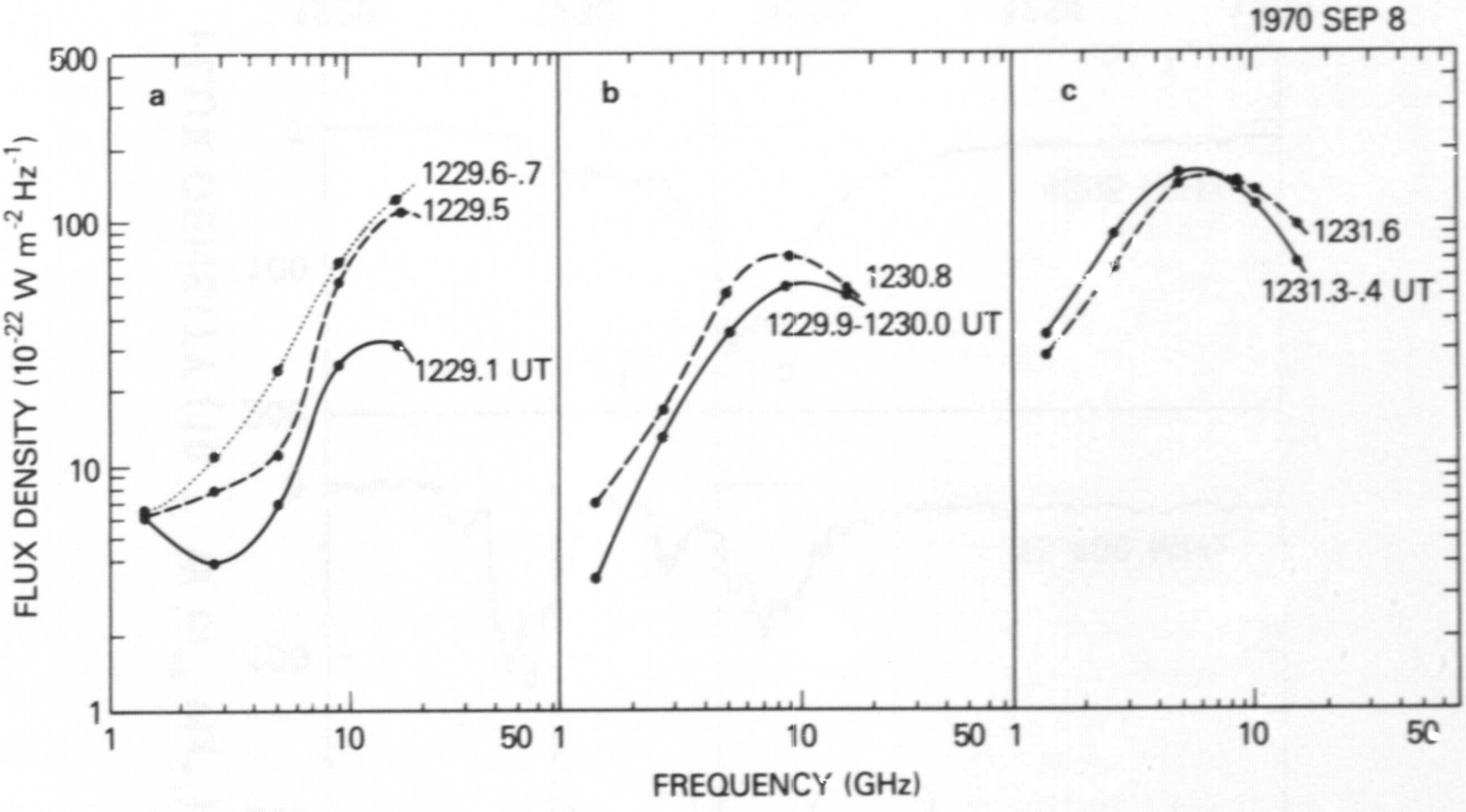

Figure 4-5. Microwave spectra at the times of peak intensity during the 1970 September 8 event. The spectra are divided into phases "a", "b", and "c" according to spectral morphology.

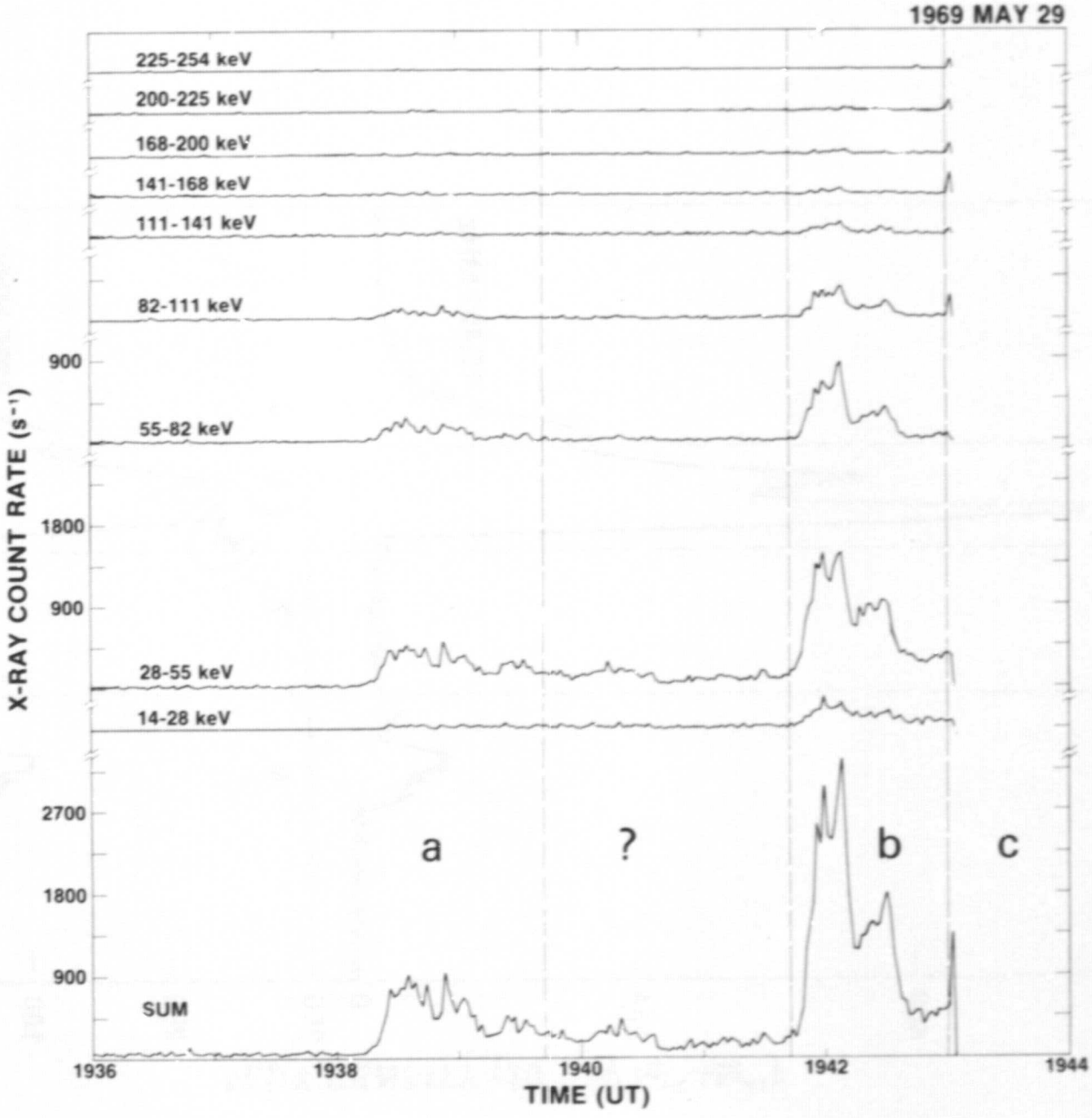

Figure 4-6. Hard X-ray time-intensity profiles for the multiply-impulsive event of 1969 May 29. Portions labeled "a", "b", and "c" correspond to the phases of microwave spectral evolution shown in Figures 4-8a, 4-8b, and 4-8c.

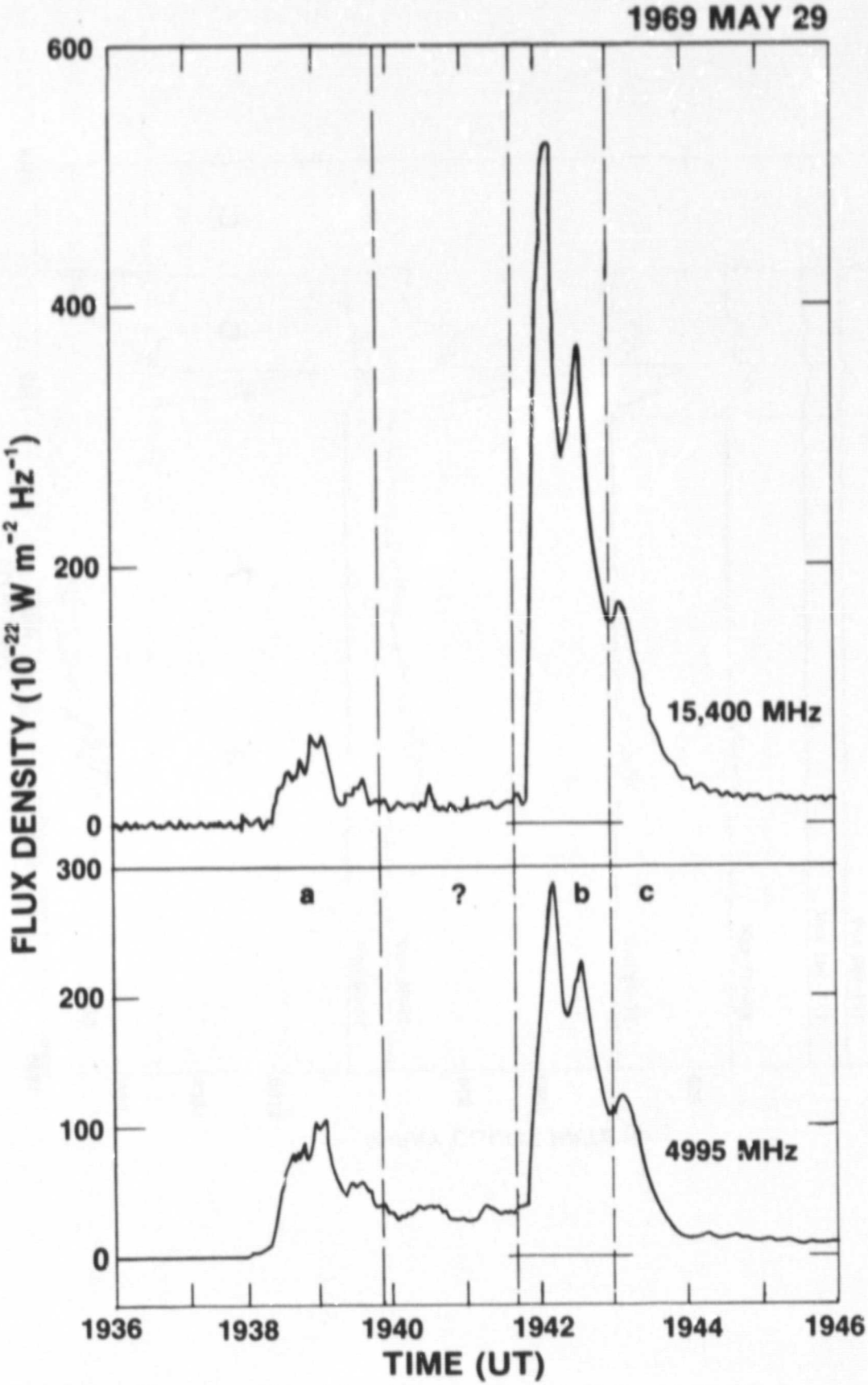

Figure 4-7. Microwave time-intensity profiles at 4995 and 15,400 MHz for the 1969 May 29 event. Portions labeled "a", "b", and "c" correspond to Figures 4-8a, 4-8b, and 4-8c, respectively.

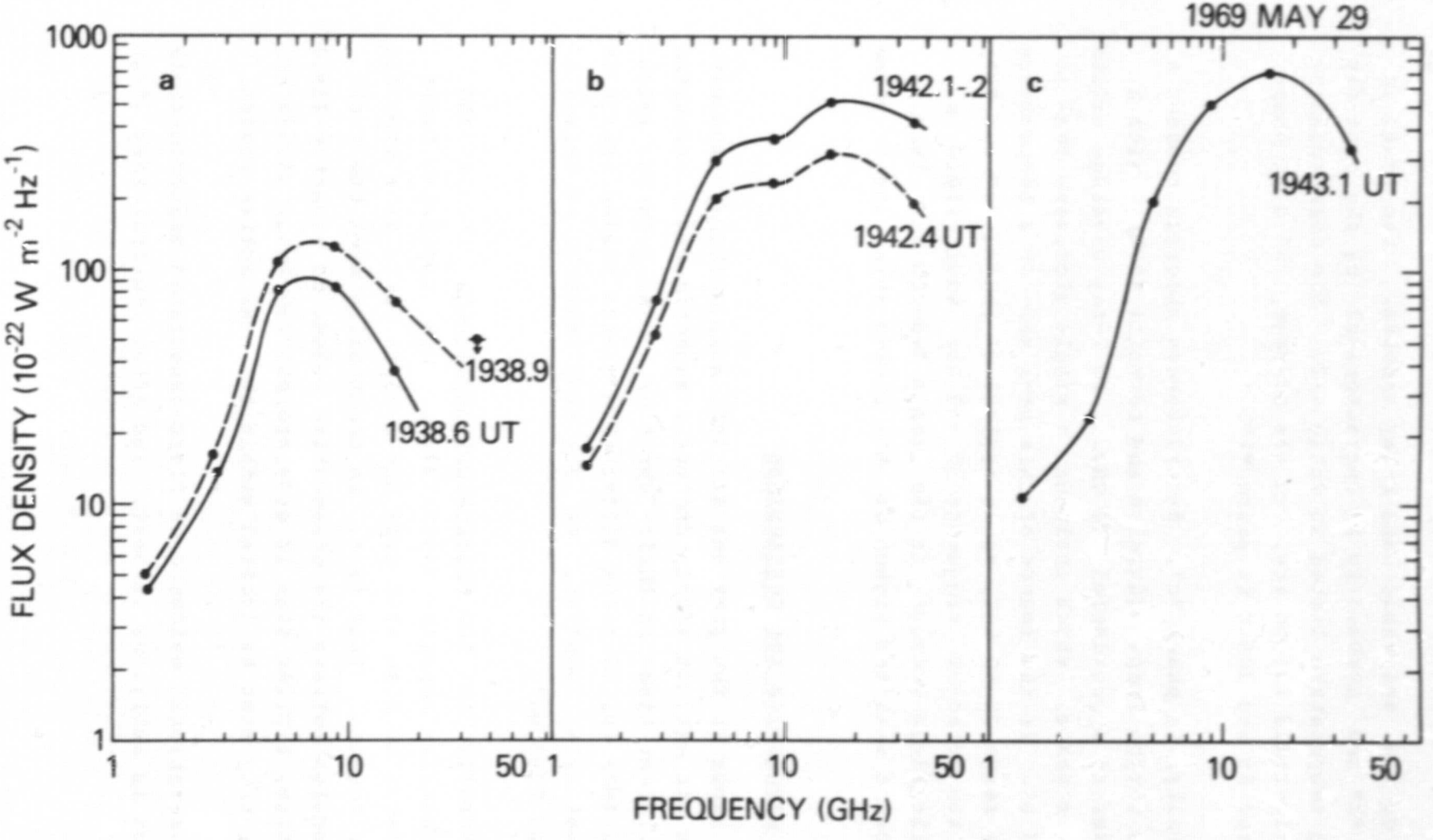

Figure 4-8. Microwave spectra at the times of peak intensity during the 1969 May 29 event. The spectra are divided into phases "a", "b", and "c" according to spectral morphology.

basis of the available hard X-ray spectra, the peaks in phase "b" are assumed to be characterized by the best-fit single temperature listed in Table 4-3. The corresponding magnetic-field values are, on the average, 50 G in phase "a", and 65 and 200 G in phase "b".

Finally, in phase "c", the microwave spectrum resumes a single C-type shape (Guidice and Castelli 1975) with a turnover at approximately 12 GHz. No X-ray coverage exists for this phase, which includes a single microwave peak at 1943.1 UT. If the source of this peak were at a temperature in the range 34-60 keV, as is typical of phases "a" and "b", then the turnover frequency of ~12 GHz would yield a magnetic-field strength in the range 140-220 G. This is consistent with the higher of the fields appearing in phase "b".

4.3 DISCUSSION AND CONCLUSIONS

As shown in the previous section, some multiply-impulsive bursts can exhibit widely different magnetic-field strengths at different times in their duration. The question which then arises is, do these different magnetic fields appear in the same burst location, or are they features of separate flaring regions?

According to the Solar-Geophysical Data Prompt and Comprehensive Reports (1969-1972), each impulsive burst correlates in time with only one H-alpha flare in a specific active region. This fact, in conjunction with the short time scales between the consecutive phases of magnetic-field evolution, implies that if separate sources exist within one burst, they must be located within the same active region.

Observational evidence on flare-associated magnetic-field changes is ambiguous at best, and often contradictory (Rust

1976a,b). Although extensive observations of the photospheric field have been made over the past 20 years (e.g., Howard and Babcock 1960; Howard and Severny 1962; Severny 1969; Michard 1971; Harvey and Harvey 1976), almost no information has been obtained on the temporal evolution and spatial structure of the fields in the chromosphere and corona, where most of the hard X-ray and microwave bursts occur. The available information, most of it indirect, leads to the conclusion that the magnetic field in a single location does not change during flares by factors of 2-3, as would be required to fit the present observations. The existence of homologous flares, which are nearly identical events occurring within hours of each other, strongly suggests that the magnetic features of a flaring region are not destroyed, even during large events (de Feiter 1974; Svestka 1976; Zirin 1978). The persistence of magnetic structures above active regions is implied also by the presence of "elementary burst structures" both in hard X-ray and in microwave events (van Beek, de Feiter, and de Jager 1974; de Jager and de Jonge 1978; Wiehl 1979). Magnetic reconnection processes, which are thought to provide the energy for the impulsive phase, convert at most 5% of the ambient magnetic-field energy into heating and particle acceleration (Baum and Bratenahl 1976; Schnack and Killeen 1977, quoted by Spicer 1978). If the reconnection process results from a driven instability (cf. Spicer 1978), the magnetic energy will be replenished at the same rate as it is released, for the duration of the flare. Thus the ambient field strength should remain constant, on the average, and not change drastically between the emission of one group of spikes and the next.

The main conclusion is, therefore, that the different magnetic-field strengths belong to separate regions in the flare area. The idea that complex, impulsive structures in

flares originate in different areas has been proposed by many authors (e.g., Beigman et al. 1969; Hagen and Neidig 1971; Anderson and Mahoney 1974; Vorpahl 1976; Zirin 1978). This suggestion has been supported primarily by evidence of an indirect nature. Zirin and Tanaka (1973) observed good temporal correlations between hard X-ray spikes and H-alpha brightenings during the 1972 August 2 flare. Hobbs et al. (1973) and Alissandrakis and Kundu (1975) observed impulsive microwave bursts with the NRAO interferometer at 3.7 and 11.1 cm. They found evidence for discrete small-scale features within the bursts, with sizes of a few arcsec. Using the VLA interferometer at 4.9 GHz, Marsh, Zirin, and Hurford (1979) observed microwave events with impulsive components clearly located in regions a few arcsec apart, but with no hard X-ray coverage. Simultaneous interferometric-microwave and hard X-ray observations of a single impulsive event, occurring on 1979 February 17, have been interpreted in terms of a migrating double-source model (Kosugi 1980). All of these observations are consistent with the existence of small-scale spatial features within impulsive flares. Circumstantial support for the existence of different source regions in the burst of 1970 September 8 is provided by an analysis of periodic hard X-ray emission in large bursts seen with OSO-5 (Lipa 1978). Of the 28 bursts studied, only 2 exhibit no signs of periodic behaviour in their time-intensity profiles: the 1970 September 8 event, and a non-impulsive event. This lack of periodicity puzzled the author of this earlier work, because the intensity structures of these events are not appreciably different from those of the pulsating events. In the context of the present research, however, the aperiodicity of the September 8 event appears to be a natural consequence of the multiple sources present in the flaring region.

The distance between the sources within the bursts presented here cannot be determined accurately from the available data. Certain assumptions can be made, however, which enable one to estimate this separation.

If the sources were causally related, then the time between successive manifestations of different magnetic-field strengths would equal the time required for some triggering disturbance to propagate between the two regions. This relationship provides a distance estimate only if there exists such a sequential connection between the component sources. Under the assumption that the disturbance travels at or near the Alfvén speed V_A, the distance D between the individual sources can be expressed as follows:

$$D = V_A \Delta t = 2.2 \times 10^6 \; B \; n_e^{-0.5} \; \Delta t \quad \text{km} \quad , \qquad (49)$$

where n_e is the local electron density in cm^{-3}; B, the local magnetic-field strength in gauss; and Δt is chosen to be the time between the last hard X-ray peak in one phase and the first peak in the following phase, in seconds. For the relevant values of n and B, the Alfven speed is found to be ~ 3500 km s^{-1} for the September 8 burst and ~ 2700 km s^{-1} for the May 29 burst. The temporal separation for the September 8 event is $\Delta t \cong 12$ s, yielding a source separation of about 4.2×10^4 km. The corresponding values for the May 29 event are $\Delta t = 30$ s and $D = 8.1 \times 10^4$ km, respectively.

Another technique for deriving the source separation requires a quantitative model for the functional dependence of the local magnetic-field strength on height in the solar atmosphere. The main obstacle to implementing this method is that realistic models of the magnetic-field topology within flaring regions are not available. For simplicity, the potential dipole model of Takakura and Scalise (1970)

has been used to illustrate this technique. The true distance is underestimated because no horizontal separation can be taken into account. Taking the photospheric field strength B_o=2800 G, after Castelli et al. (1974), the model yields the following expression:

$$h = (1.2\times10^{17}/B)^{0.333} - 3.5\times10^{4} \quad \text{km} \; . \qquad (50)$$

The vertical distance between the sources, therefore, is:

$$\Delta h = (1.2\times10^{17}/B_1)^{0.333} - (1.2\times10^{17}/B_2)^{0.333} \quad \text{km} \; . \qquad (51)$$

For the September 8 event, the vertical separation derived in this manner is $\Delta h \geq 3.7\times10^{4}$ km, which is comparable to the first estimate. For the May 29 event, the vertical distance is $\Delta h \cong 3.8\times10^{4}$ km, only half the first estimate; this would be consistent with the existence of a significant horizontal separation between the regions. Again, it must be stressed that, while the actual values of the distances derived above are only estimates, the difference in magnetic-field strengths still strongly suggests a difference in location. The distances estimated by means of the Alfvén-speed assumption fall well within the areas reported for the H-alpha flares associated with these hard X-ray bursts (Solar-Geophysical Data Prompt and Comprehensive Reports, 1969-1972).

In conclusion, the present analysis of hard X-ray and microwave bursts has identified a class of multiply-impulsive solar events which consist of basic impulsive spikes, groups of which originate in localized flaring regions. Further investigation of the fine structure within regions producing complex flares will benefit greatly from the use of observational equipment with good temporal and spatial resolution. Coincident observations with hard X-ray

imaging instruments and interferometers operating in the microwave range are needed particularly to resolve the basic impulsive elements in these bursts, thereby increasing our understanding of the underlying physical processes.

Chapter 5

THE ROLE OF BETATRON ACCELERATION IN COMPLEX SOLAR BURSTS

As is shown in Chapter 4, the multiple-spike bursts comprise two distinct classes: events whose component spikes apparently originate in one location, and events in which groups of spikes appear to come from separate regions which flare sequentially. The latter case is discussed in detail in Chapter 4, using two specific bursts to illustrate the characteristics of the group. The first part of the present chapter is devoted to the former class of events, focussing on the search for the cause of multiplicity in emissions from a single source region. In the second part of this chapter, the applicability of a specific model, initially chosen as a possible explanation for the properties of the multiply-impulsive emissions, is evaluated in the context of the more complex, extended flare emissions. For the most part, models which attempt to account for the intensity variations seen in all but the simplest bursts are qualitative, and do not provide quantitative methods of evaluating their hypotheses. Several reports of periodicities or quasi-periodicities in flare-associated hard X-ray and microwave emissions have appeared in the literature (e.g., Maxwell and Fitzwilliam 1973; Hoyng, Brown, and van Beek 1976; Lipa 1978), but the theories proposed to explain these phenomena have been speculative rather than analytical (e.g., McLean et al. 1971; Wild and Smerd 1972).

The simplest explanation of intensity variations within a hard X-ray burst is that each spike represents a new electron-acceleration event (see Chapter 3). Multiple accelerations could result either from energizing of a

separate population of electrons to produce each spike, or from repeated reacceleration of the same electron population. The former case is more compatible with pure thick-target or thin-target models (*cf.* Sections 3.1.2 and 3.1.3, respectively), because in both models the electrons are "lost" (by collisions or by escape) and are not available for reacceleration. The latter case - reacceleration - necessitates a trap situation, in which the initially-introduced distribution of energetic electrons loses its members sufficiently slowly that repeated reacceleration can persist throughout the burst duration. The reacceleration hypothesis is attractive because it does not require large numbers of electrons to account for all the intensity peaks. However, the energy requirements are the same for both successive accelerations of fresh electrons and reacceleration of a single electron population.

In a trap model involving reacceleration, the analysis relies on fewer unknown quantities than in models involving discrete "injections" of accelerated electrons: once the electron spectrum and number density are set at the beginning, they can be determined at any other time during the burst. Furthermore, because the single source location (*i.e.*, the upper loop) must be consistent with the properties of a trap (see Section 3.1.4), the physical conditions in the source can be assumed to remain constant or to evolve in a well-defined manner. The symmetry inherent in most trap models also allows the propagation of periodic or quasi-periodic disturbances within the loop. In contrast, the models which assume separate accelerations of separate electron distributions to account for each intensity peak require as many discrete sources as there are intensity maxima; these models also lack inherent symmetries to account for periodic behaviour.

The first serious attempt to incorporate the features mentioned above in a quantitative trap model, and to apply it to an observed hard X-ray burst, was made by Brown and Hoyng (1975). Intrigued by the nearly periodic spacing of intensity maxima in the complex flare of 1972 August 4, Brown and Hoyng proposed that a quasi-periodic disturbance, causing repeated acceleration of trapped, X-ray-emitting electrons, might explain the observed behavior. Oscillations in the magnetic field of the trap appeared to be the most likely mechanism for inducing continual reacceleration of the trapped electrons, according to Brown (1973). Brown and Hoyng specifically chose magneto-acoustic waves, which travel along the field lines at approximately the Alfvén speed (cf. Section 4.3, Equation 50). The interaction of the oscillating field with the energetic electrons results in betatron acceleration of the particles, so named because this process is responsible for accelerating particles in betatron machines. The term "betatron model" will be used henceforth for the model developed by Brown and Hoyng, and for the adaptation applied in the present research.

In order to clarify the logical sequence of the material comprising this chapter, a brief preview of the results is presented here. The purely impulsive events were found to show no signs of betatron acceleration, according to the criteria described in Section 5.2.2. As a result, the betatron model cannot explain the existence of periodic or non-periodic multiply-peaked structure in complex impulsive bursts. The serendipitous inclusion, in this initial study, of two events which manifest emissions of both impulsive and non-impulsive characteristics, also designated "two-stage" bursts (see Introduction and Section 5.4), led to a more exciting discovery: during the initial few minutes of the second stage, the non-impulsive X-ray emission appears to be

consistent with the predictions of the betatron-acceleration model. To evaluate this preliminary result more rigorously, several intense two-stage events, also selected from the OSO-5 data, were subjected to the appropriate analysis and comparison with the test criteria, as was done for the multiply-impulsive events. The results of this study firmly establish the identification of the betatron process as a viable mechanism for producing the early second-stage emission, and verify the absence of betatron action in the impulsive stage. Paradoxically, while attempting to evaluate the betatron-acceleration mechanism as a possible origin for the multiplicity of impulsive emissions, we have identified, instead, a mechanism which is conspicuously absent in the impulsive stage. Furthermore, this mechanism appears to be a characteristic of the second-stage emissions, and the unique signs of its presence may serve as an improved method of identifying non-impulsive X radiation.

The betatron model is described in Section 5.1, after Brown and Hoyng (1975) and Hoyng (1975). The analysis technique and criteria for testing the model are discussed in Section 5.2. Section 5.3 and 5.4 comprise the results of the application of the betatron model to the multiple-spike bursts and the two-stage bursts, respectively. In Section 5.5, the interpretation of these results is presented. The conclusions on the role of betatron acceleration in solar flares are summarized in Section 5.6.

5.1 THE BETATRON MODEL

The general features of the betatron model, as they affect the burst evolution, are depicted in Figure 5-1. The basic characteristics of a simple magnetic trap, as described in Section 3.1.4, apply. For this model of electron acceleration, the magnetic field is assumed to be spatially uniform but temporally varying. Magnetic loops on

1. INJECTION OF IMPULSIVELY-ACCELERATED ELECTRONS INTO A TRAP (LOOP)

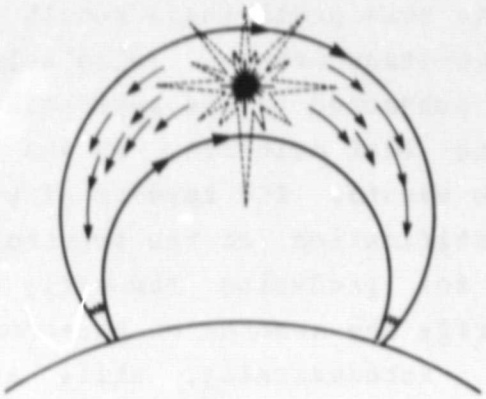

2. OSCILLATIONS IN MAGNETIC FIELD PROVIDE BETATRON ACCELERATION OF TRAPPED ELECTRONS

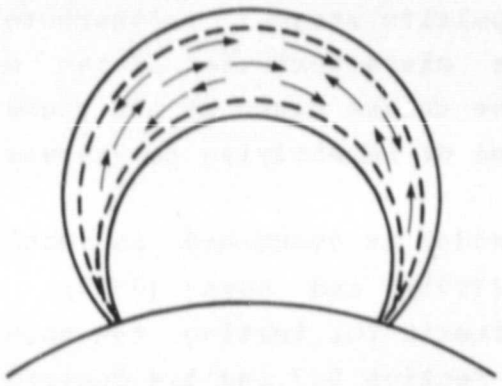

3. FINAL STAGE = DECAY OF EVENT, REFLECTING LEAKAGE OF ELECTRONS FROM TRAP, EXPANSION OF TRAP, ETC.

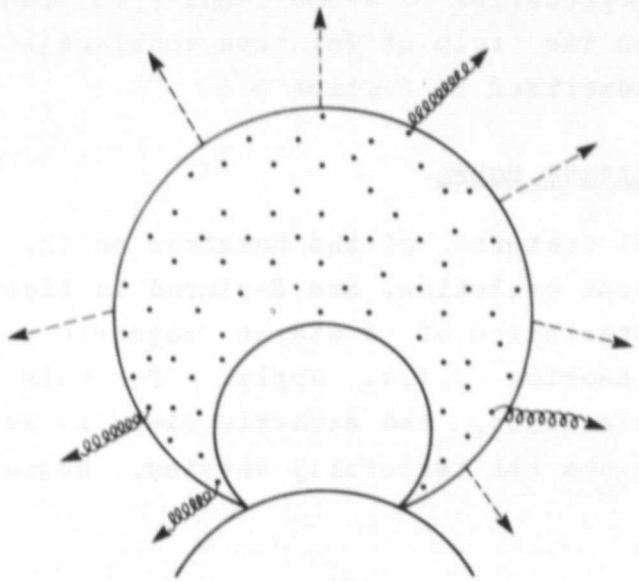

Figure 5-1. A pictorial representation of the betatron model, showing the physical evolution of the X-ray source region.

the Sun actually exhibit bipolar field topologies, with the field lines converging at the footpoints. The assumption of constant magnetic field in the trapping region is satisfied only in the upper part of a loop, where the expansion of the field is most negligible. For this assumption to apply, therefore, the emitting electrons must be confined to the top of a loop. Under these simplified conditions, one-dimensional geometry is adequate.

The particles are accelerated by the electric field associated with the changes in the longitudinal magnetic field (that is, time-dependent oscillations of the magnetic field). Throughout the betatron phase (see Figure 5-1), the entire trapping region essentially expands and contracts, as would result from the passage of a magneto-acoustic disturbance through the loop. It is reasonable to assume that the scale length of the magneto-acoustic waves travelling across the magnetic field of the trap is much greater than the gyration (Larmor) radii of the energetic electrons, and that the frequency of field oscillation is much less than the gyrofrequency. Hence the changes in electron energy associated with their transverse motion is determined by the adiabatic invariance of their magnetic moments (e.g., Krall and Trivelpiece 1973, Appendix I.7). Thus,

$$W_\perp / W_{\perp 0} = B/B_0 \ , \qquad (52)$$

where $W_{\perp 0}$ and $W_\perp$ are the electron energies due to motion transverse to the magnetic field when B_0 and B, respectively, are the magnetic-field strengths. The quantities $W_{\perp 0}$ and B_0 represent the initial values of the transverse energy and field strength, immediately before the onset of betatron acceleration. Throughout this chapter, the subscript "o" denotes initial values of the relevant

parameters. The effect of the field variations on the total energy, W, is given by the expression

$$\begin{aligned} W &= W_{\perp} + W_{\parallel} \\ &= (B/B_0) W_{\perp 0} + W_{\parallel 0} \\ &= W_0 (1 + b W_{\perp 0}/W_0) \end{aligned} \quad , \qquad (53)$$

where $W_{\parallel}$ is the electron energy parallel to the magnetic field, and

$$b = (B/B_0) - 1 \quad . \qquad (54)$$

5.2 METHOD OF ANALYSIS AND TEST OF THE MODEL

To show the effects of the betatron mechanism as manifested in the hard X-ray emission, the behaviour of the electron spectrum resulting from this process must be established first. Then, by adopting an appropriate emission model, the specific behaviour induced by betatron action on the electrons can be identified in the coincident behaviour of the X-ray spectrum. The predicted X-ray characteristics are expressed in terms of parameters which can be compared directly to X-ray observations of selected events. The X-ray data are interpreted by means of the same emission model as is adopted for the betatron-model calculations, to ensure consistency between the format of the model predictions and that of the observed spectral properties. The division of this section into two parts was dictated by the need to introduce these basic parameters, which are common to both the observational and theoretical analyses, before entering the detailed derivations of the measurable effects predicted by the betatron model. Hence, Section 5.2.1 is devoted to a description of the analysis technique applied to the X-ray data for each burst, while

Section 5.2.2 comprises an in-depth derivation of the X-ray characteristics predicted by the betatron model, and the method for testing these predictions for consistency with the X-ray emission from complex bursts.

5.2.1 Data Analysis

To investigate the temporal evolution of the X-ray emission for a large set of events, it is necessary to adopt a model for the emission process which allows both consistency with the tenets of the betatron model and calculational tractability. The actual choice is not crucial, so long as the same process is retained throughout. In a trap, some complex combination of thick-target and thin-target emissions most likely applies; however, within the confines of this analysis, the simplest case which is analytically tractable will suffice. In choosing between thick-target and thin-target representations, it was noted that the thick-target case provides the simplest means of relating the electron spectrum to the photon spectrum: the instantaneous emission is independent of the density in the trap (*i.e.*, the target region), and does not rely on the temporal evolution of the electron energy distribution (see Sections 3.1.2 and 3.1.3). In a sense, the selection of the thick-target case provides a self-consistent means of characterizing the electron and photon spectra, at each moment, without necessarily representing the actual physical situation in the source region.

The thick-target parameter $F(W_1)$, introduced in Section 3.1.2, is used in the present analysis to characterize the observed X-ray spectra in terms of the emitting electrons. This parameter is defined as follows (*cf.* Equation 21):

$$F(W_1) = 2.0 \times 10^{33} \, A \, (\gamma-1)^2 \, B(\gamma-1/2, 1/2) \, W_1^{-\gamma} \quad , \qquad (55)$$

where $F(W_1)$ is the number flux of accelerated electrons injected into the target region, with energies greater than W_1, in units of electrons s^{-1}; , the hard X-ray spectral index; A, the normalization constant of the power-law X-ray spectrum, as defined by $I(E)=AE^{-\gamma}$ (see Section 3.1.2); and $B(\gamma-1/2,1/2)$, the Beta function, defined in Equation 19. The low-energy cut-off, W_1, is taken to be 25 keV, slightly below the lowest energy of the hard X-ray observations used here to determine the spectrum. Substituting W_1=25 keV into Equation 55 yields

$$F(25) = 2.0\times10^{33} A (\gamma-1)^2 B(\gamma-1/2,1/2) (25)^{-\gamma} . \quad (56)$$

For the hard X-ray bursts studied, F(25) and γ were calculated for each 0.2-second interval by means of the computer program listed in Appendix A. Although a least-squares fitting routine (as was used in the analysis described in Chapter 4) would provide the most accurate determinations of the spectral index, γ, and the normalization constant, A, this procedure is far too time-consuming to be practical for analysis of thousands of spectra. A less precise but adequate technique was implemented, wherein is the weighted mean of the spectral indices determined for each pair of energy channels showing significant flux above the noise level; a pair consists of Channel 2 and one of the higher-energy channels (see Chapter 2, Table 2-1). To avoid systematic errors induced by the point-to-point variation in the highest-energy channel containing significant flux, the spectral index was calculated using data from Channels 2, 3, and 4 only. The constant A was determined from the flux in Channel 2, I(2), the mean energy of that channel, E(2), and the previously-calculated value of γ, according to the following expression:

$$A = I(2)\ [E(2)]^{-\gamma} \qquad (57)$$

Finally, F(25) was calculated using the relevant values of and A and Equation 56. A plot showing the evolution of F(25) versus γ then was generated for each event, and searched for indications of the pattern characteristic of betatron acceleration (see next subsection).

5.2.2 Procedure for Testing the Betatron Model

In order to relate the expressions derived in Section 5.1 to the changes produced in the flux and spectrum of the energetic electrons, the original relationship between the transverse and total energies must be known, as well as the X-ray flux and spectrum at that instant. The former requirement corresponds to deducing the initial pitch-angle distribution of the electrons when they where "injected" (*i.e.*, the primary acceleration) into the trap, a characteristic intrinsic to the physics of this initial acceleration process. In the absence of definitive evidence favoring a particular model for the brief initial process, Brown and Hoyng (1975) adopt acceleration by a large-scale electric field as a plausible choice. Under these conditions, W does not change with the action of this primary electric field on the electrons, and is treated as a constant for the entire population of high-energy electrons.

The original betatron model thus is predicated on injecting electrons with a particular anisotropic pitch-angle distribution into a trap. Although direct electric-field acceleration is the most common example of this type of mechanism, it need not be the only possibility. Other possible acceleration mechanisms, including those which yield isotropic pitch-angle distributions, are considered in Section 5.5, with emphasis on the applicability of the betatron model under these alternative initial conditions.

The assumption of a directed electric field, or any process which results in the same anisotropic pitch-angle distribution, as the initial accelerating mechanism is a pivotal aspect of the model. Because electric-field acceleration results in smaller pitch angles for the higher-energy electrons (Hoyng 1975), their electron energy is due predominately to motion parallel to the magnetic field (i.e., $W_{\parallel} >> W_{\perp}$). The betatron-acceleration process, however, acts only on the transverse electron energy (cf. equation 52). Consequently, the change in energy is the same for all electrons, but the fractional change in total energy, W, is less for the higher-energy electrons. As the magnetic field increases, the more numerous lower-energy electrons are accelerated proportionately more than those at higher energies, so that the power-law electron spectrum steepens while the instantaneous electron rate required to account for the X-ray flux increases. The opposite correlation obtains when the field decreases: the lower-energy electrons are decelerated most, resulting in spectral hardening and decreasing electron flux. Thus, a plot showing the behaviour of the instantaneous electron rate versus spectral index, resulting from the betatron-acceleration process, would exhibit a curve of correlation traced from low values of the electron rate and spectral index to high values of both parameters. The spectral behaviour ascribed to the oscillating strength of the magnetic field, as described above, corresponds to periodic "motion" up and down the predicted correlation path.

It also is necessary to relate the hard X-ray photon spectrum to the parent electron spectrum. Because this analysis is focussed on evaluating variations in the observed flux and spectrum, rather than absolute values, the choice of a particular form for the electron distribution is not of critical importance. For simplicity, the work

presented here adopts the power-law electron number spectrum used by Brown and Hoyng:

$$f_0(W_0) = (\delta_0 - 1)\,(N_0/W_1)\,(W_0/W_1)^{-\delta_0} \quad , \qquad (58)$$

in units of electrons per unit energy. N_0 is the total initial number of electrons with energies greater than the low-energy cut-off, W_1 (see Section 3.1.2), such that $N_0 \equiv \int_{W_1}^{\infty} f_0(W_0)\,dW_0$, and δ_0, the initial electron spectral index. If continuity is assumed, the combination of Equations 53 and 58 produces an expression for the spectrum of the trapped electrons at any time during the betatron-acceleration phase:

$$\begin{aligned} f(W,b) &= f_0(W_0)\,(dW_0/dW) \\ &= (\delta_0 - 1)\,(N_0/W_1)\,[(W - bW_{\perp 0})/W_1)^{-\delta_0} \quad , \end{aligned} \qquad (59)$$

It is assumed that collisional losses are negligible, over the lifetime of the betatron-acceleration phase.

The total number of electrons above energy W_1, $N(b)$, and their effective spectral index, δ, at any time, are obtained from Equation 59 as follows:

$$\begin{aligned} N(b) &= \int_{W_1}^{\infty} f(W,b)\,dW \\ &= N_0[1 - (bW_{\perp 0}/W_1)]^{-\delta_0 + 1} \quad . \end{aligned} \qquad (60)$$

Because the spectrum given by Equation 59 is not quite a power law, an effective power-law index, $\delta(b)$, is defined to characterize the actual electron spectrum. Following Hoyng (1975), $\delta(b)$ is defined as the logarithmic point slope at the lowest energy of observation, E_1. Thus,

$$\delta(b) = \delta_0/[1 - (bW_{\perp 0}/E_1)] \quad . \qquad (61)$$

The spectrum defined by Equations 59 and 61 describes the electron distribution in the trap and its spectral index, at each moment during the betatron phase. Because this distribution is assumed to be only weakly affected by collisions with the background plasma in the loop, the X-ray emission can be derived directly from this electron spectrum, without the modifications required by the thick-target model (see Section 3.1.2). According to Brown (1971), the electron spectral index, δ, and the resultant hard X-ray spectral index, γ, are related by the following expression:

$$\delta = \gamma - 1/2 \quad . \tag{62}$$

The instantaneous electron rate, $F(W_1)$, and the total number of electrons above the cutoff energy W_1, $N(b)$, obey the following proportionality:

$$F(W_1) \propto (\gamma - 3/2)\, n\, N(b) \quad , \tag{63}$$

where n is the ambient particle density in the trap (see also Section 3.1.2, Equation 22). It is convenient to express the relationship between $F(W_1)$ and $N(b)$ in terms of the ratios of betatron-phase parameters to the initial values; that is,

$$F(W_1)/F_0(W_1) = [\,(\gamma - 3/2)/(\gamma_0 - 3/2)\,](n/n_0)[\,N(b)/N_0\,] \quad , \tag{64}$$

where the subscript "o" denotes initial values, as before. The assumption of one-dimensional geometry implies that $n/n_0 = B/B_0 = 1+b$.

In order to derive F/F_0 as a function of γ/γ_0 alone, rather than of b, an expression relating b and γ is required. Equations 61 and 62 yield the quantity b as a

function of γ, the lowest energy of observation, E_1, and the initial transverse electron energy, $W_{\perp 0}$, as follows:

$$b = (\gamma-\gamma_0)E_1/(\gamma-1/2)W_{\perp 0} \quad . \tag{65}$$

Hence, Equation 64 can be reexpressed, with the aid of Equations 60 and 65, as follows:

$$\frac{F(W_1)}{F_0(W_1)} = \frac{(\gamma-3/2)}{(\gamma_0-3/2)}\left[1+\frac{(\gamma-\gamma_0)\ E_1}{(\gamma-1/2)\ W_{\perp 0}}\right]\left[1-\frac{(\gamma-\gamma_0)\ E_1}{(\gamma-1/2)\ W_1}\right]^{-\gamma_0+3/2} . \tag{66}$$

For consistency with the work of Brown and Hoyng and with the thick-target parameter, $F(W_1)$, defined by Equation 56, the low-energy cut-off, W_1, was set at 25 keV. In the context of the OSO-5 observations, this is a reasonable choice because it implies only a minor extrapolation below the energy range of the hard X-ray spectrometer. The lowest channel used in the OSO-5 data analysis is Channel 2, spanning the energy range 28 to 55 keV (cf. Table 2-1); hence, E_1=28 keV. The initial transverse energy, $W_{\perp 0}$, remains a free parameter which can be varied to obtain the best possible fit to the data (see Section 5.4). With the abovementioned values for W_1 and E_1 substituted into Equation 66, the (F,γ) relationship used for comparison of the betatron model with the OSO-5 hard X-ray observations is

$$\frac{F(25)}{F_0(25)} = \frac{(\gamma-3/2)}{(\gamma_0-3/2)}\left[1+\frac{(\gamma-\gamma_0)\ 28}{(\gamma-1/2)\ W_{\perp 0}}\right]\left[1-\frac{(\gamma-\gamma_0)}{(\gamma-1/2)}(1.12)\right]^{-\gamma_0+3/2} . \tag{67}$$

where $W_{\perp 0}$ is in units of keV.

For each event studied, the results of the (F,γ) analysis of the hard X-ray data (Section 5.2.1) and the (F,γ)

correlation predicted by the betatron model (Equation 67) are used jointly to test for the presence of a phase of betatron acceleration, in the following manner. First, we note that the relationship expressed by Equation 67 describes a curve in the (F,γ) plane, from low values of $F(25)$ and γ to high values of both parameters (see, e.g., Figures 5-3 and 5-6). The (F,γ) plot characterizing the burst observations then is examined for visible evidence of such a curve, as a preliminary indication of the possible presence of betatron acceleration during some portion of the event. Those bursts which show no signs of the (F,γ) correlation curve defined by Equation 67 thus are identified as non-betatron events, and are not candidates for further analysis.

Those bursts for which the (F,γ) plots exhibit the unique pattern indicative of betatron acceleration are denoted betatron events, and are investigated further to establish the relevant properties of the betatron stage. For each burst which exhibits a betatron stage, the parameters $F_0(25)$ and γ_0 are determined observationally, from the hard X-ray flux and spectrum at the moment when the betatron action apparently starts (see Section 5.2.1). In the actual (F,γ) plots, the betatron-induced pattern appears as a general trend of moving, from point to point, up and down the particular curve; according to the model, this behaviour reflects the rise and fall of the magnetic-field strength during the trap oscillations. As a result, the beginning (or end) of the betatron phase usually is distinguishable as the point where the observed (F,γ) path changes to (or from) the best-fit predicted curve. To determine the (F,γ) correlation curve which best fits the observed betatron "feature" in the (F,γ) plot, the relevant values of $F_0(25)$ and γ_0 are substituted into Equation 67, and various values of the transverse electron energy, $W_{\perp 0}$, are tried. In this

manner, the start time and duration of the betatron action in these events, as well as the initial value of the electron energy perpendicular to the magnetic field, are identified.

5.3 APPLICATION TO THE MULTIPLE-SPIKE BURSTS

A set of 20 multiply-impulsive hard X-ray bursts were selected from the OSO-5 data, for testing the betatron model. These events were chosen from the larger set of multiply-impulsive bursts, initially selected according to the criteria outlined in Section 4.1, by requiring sufficient X-ray flux to allow determination of the thick-target parameters F(25) and γ throughout most, if not all, of the event. Table 5-1 lists the bursts and the time periods over which they were tested for the presence of betatron acceleration. The test periods denote the time span for which the flux in 2 or more channels was above the noise level, although minor "breaks" due to low flux above Channel 2 are included occasionally.

An example of the (F,γ) plot obtained for a multiple-spike burst, the event of 1970 March 26, is shown in Figure 5-2. The smooth, curved path predicted by the betatron model (see Section 5.2.2) is absent in this plot. Of the 20 events studied, only 2 evinced definite signs of betatron acceleration in their (F,γ) plots: 1969 April 26 and 1969 May 6. The (F,γ) plot for the April 26 event is shown in Figure 5-3 , with the best-fit curve predicted by the betatron model (Equation 67) superposed on the relevant portion of the graph (Figure 5-3, Part 2). Due to the large range of F(25), about 3 orders of magnitude, the (F,γ) plot for this event is presented in two parts, roughly corresponding to the two stages of the burst. The difference between Figures 5-2 and 5-3 is obvious: even without considering the betatron model, the immediate

TABLE 5-1

MULTIPLE-SPIKE BURSTS TESTED FOR BETATRON ACCELERATION

Date	Timespan of Test Period
1969 February 13	20:12:44 - 20:13:35
March 21	19:43:36 - 19:44:29
March 22	06:44:04 - 06:45:40
April 26	23:02:58 - 23:09:00
May 6	02:38:48 - 02:44:42
May 29	19:38:17 - 19:39:08 ; 19:41:47 - 19:43:01
June 6	16:06:01 - 16:07:28
1970 March 1	05:01:26 - 05:03:51
March 1	13:59:10 - 14:02:11
March 1	20:03:59 - 20:06:03
March 17	05:27:06 - 05:27:50
March 26	17:27:11 - 17:27:55
May 26	11:22:15 - 11:23:57
June 28	20:00:29 - 20:05:29
July 23	18:42:05 - 18:46:31
August 18	22:07:08 - 22:08:03
September 8	12:28:59 - 12:30:04 ; 12:30:39 - 12:31:59
1971 May 3	14:12:05 - 14:15:13
August 21	09:34:01 - 09:35:14
August 22	07:50:09 - 07:52:00

implication is that the April 26 event manifests a physical phenomenon, evident in Part 2 of Figure 5-3, which is completely absent in the March 26 event. The (F,γ) plot for the May 6 burst qualitatively resembles Figure 5-3, but is characterized by a different value of the free parameter W_{10}, the initial transverse electron energy, for the best-fit betatron-action path.

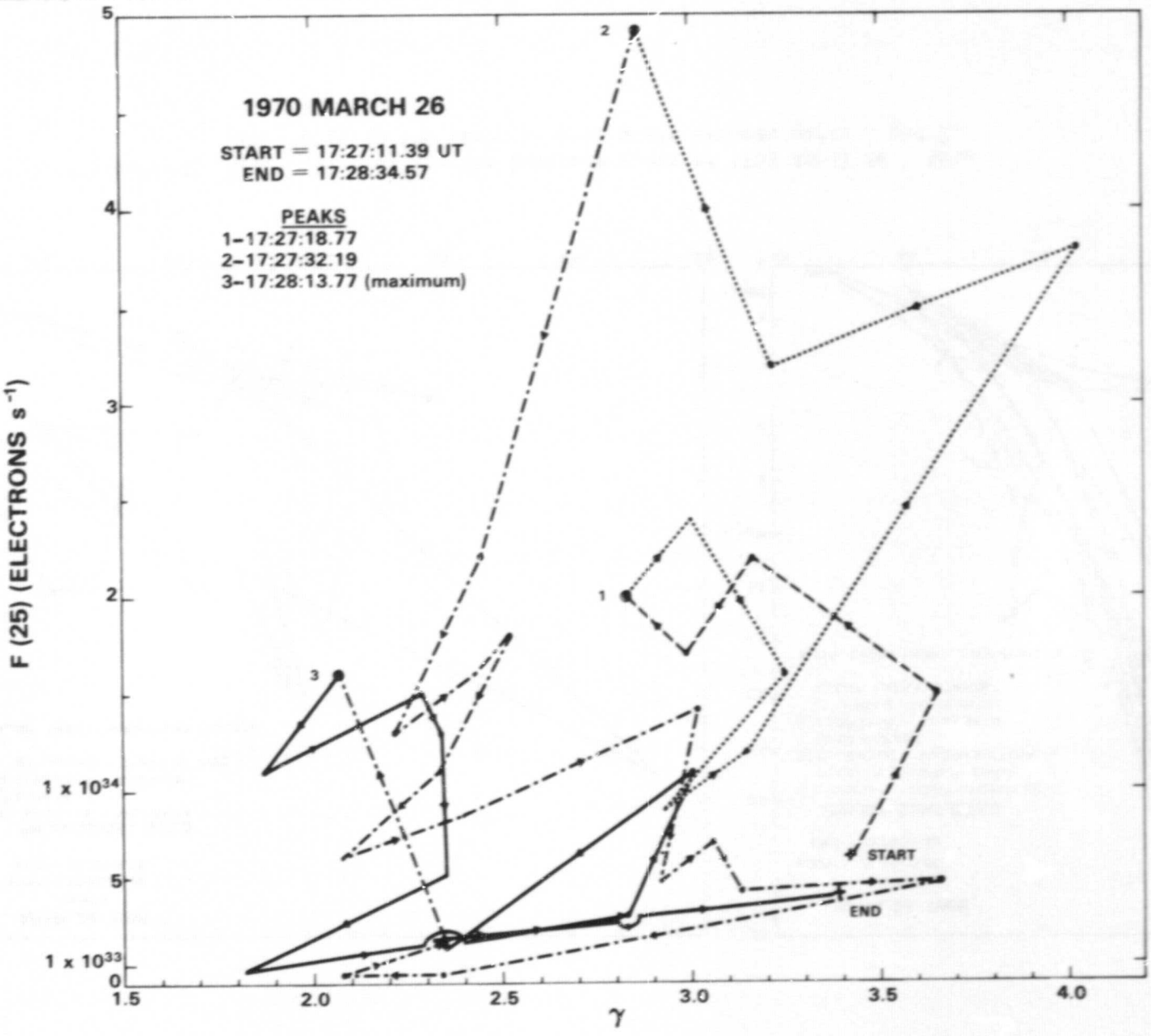

Figure 5-2. The (F,γ) plot for the multiply-impulsive event of 1970 March 26.

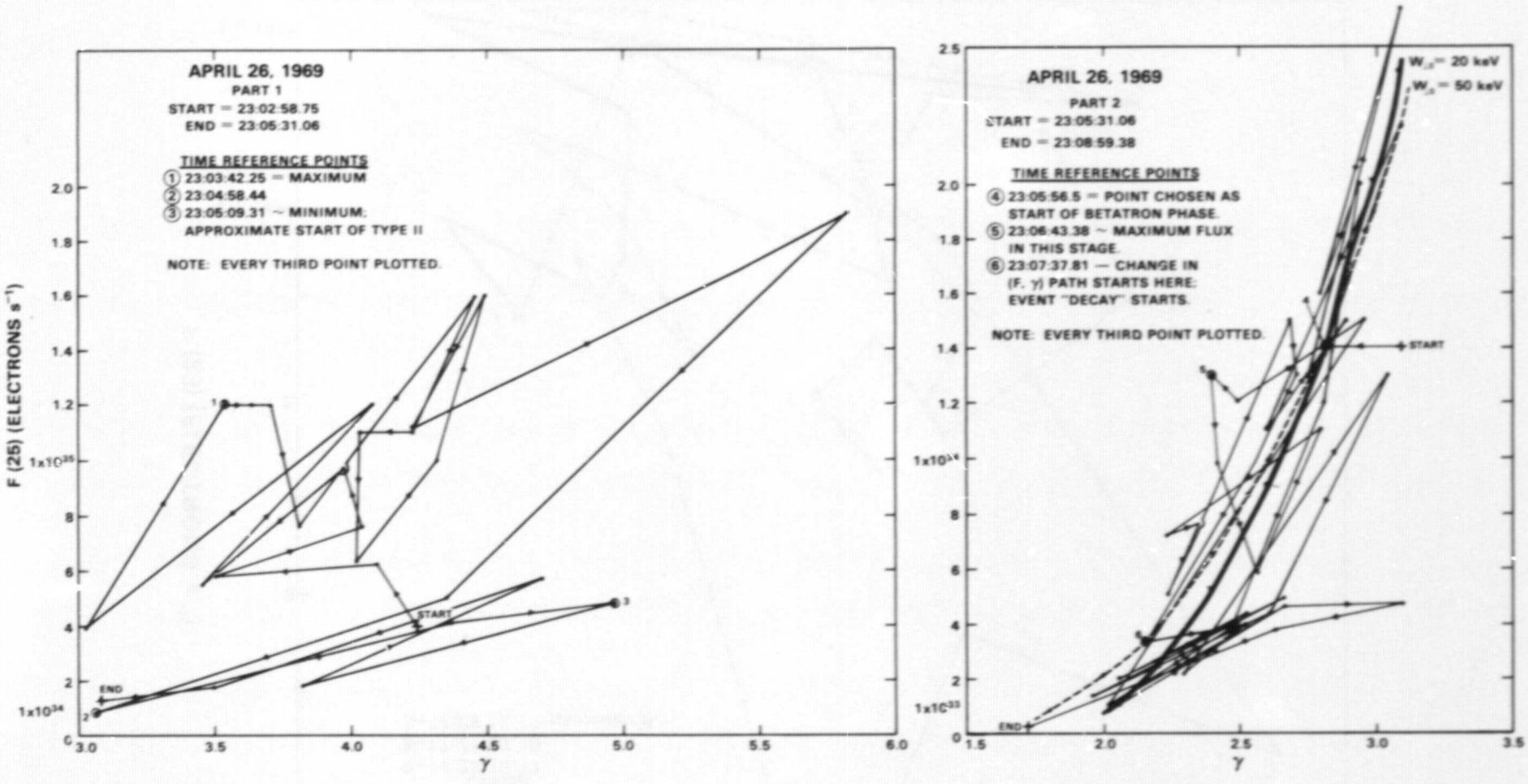

Figure 5-3. The (F,γ) plot for the betatron event of 1969 April 26. Note the change in the vertical-axis scale between parts 1 and 2.

The next question is, of course, what differentiates these 2 events from the other multiple-spike bursts? From inspection of Table 5-1, one distinguishing feature is apparent: the timespans over which the 2 bursts were tested for betatron action both exceed 5 minutes, whereas the majority of the remaining events (12 of 17) were tested for periods less than 2 minutes. However, this is not unique to the two events which evince betatron phases: six other multiply-impulsive bursts had test durations of over 2 minutes, yet did not show signs of betatron acceleration. Consequently, the longer duration of the betatron events may be a "necessary but not sufficient" condition for the presence of the betatron process.

An additional characteristic must be found which differentiates between the betatron and non-betatron events. To identify the underlying cause, the nature of betatron acceleration was considered, with particular emphasis on observable manifestations of the related physical processes. The most promising line of investigation proved to be the identification of other flare-associated emissions which are evidence for the presence of the magnetic-field oscillations fundamental to the betatron process. Such oscillations could result from photospheric activity, such as twisting of the footpoints of the magnetic trap, or from the passage of an energetic disturbance, such as a shock wave, through the trap. The lack of H-alpha coverage with good spatial and temporal resolution during the last solar maximum prevented further evaluation of the former hypothesis. The latter hypothesis, however, provides a clue to another feature distinguishing the betatron events.

The flare-associated phenomenon most commonly interpreted as evidence for shock waves is the radio type II burst, generally observed at frequencies below 600 MHz (Kundu

1965). Meter-wave data were available for 15 of the 20 events studied; copies of the dynamic spectra were graciously supplied by Drs. Maxwell (Fort Davis), Stewart (Culgoora), and Urbarz (Weissenau). The radio records were searched for evidence of type II emission, resulting in the identification of type II bursts accompanying 7 of the 15 X-ray events. Of these 7 events, 1 burst included the start of the type II emission within the test period: the April 26 event. The 10-580 MHz dynamic spectrum, obtained by the Fort Davis (Harvard) Radio Station, is shown in Figure 5-4, together with the time-intensity profile of the hard X-ray burst. The type II burst began at approximately 2305.5 UT, with fundamental emission at 120 MHz, while the stage of betatron acceleration apparently started at 2305.7 UT. Indirect evidence for the existence of a periodic perturbation during the April 26 event is provided by the Fourier analysis of the hard X-ray emission (Lipa 1978), in which several significant periods ranging from 22 to 71 s were identified. Also seen in conjunction with the April 26 event were a succession of chromospheric brightenings, to the east of the main flare, and oscillations of a nearby filament, suspended $\sim 10^5$ km above the flaring region (Harvey, Martin, and Riddle 1974). These authors affirm that one shock wave was responsible for both the radio and the optical phenomena, lending additional support to the proposed association of a shock wave with the two-stage event under consideration. Unfortunately, no meter-wave coverage was available for the other betatron event, 1969 May 6.

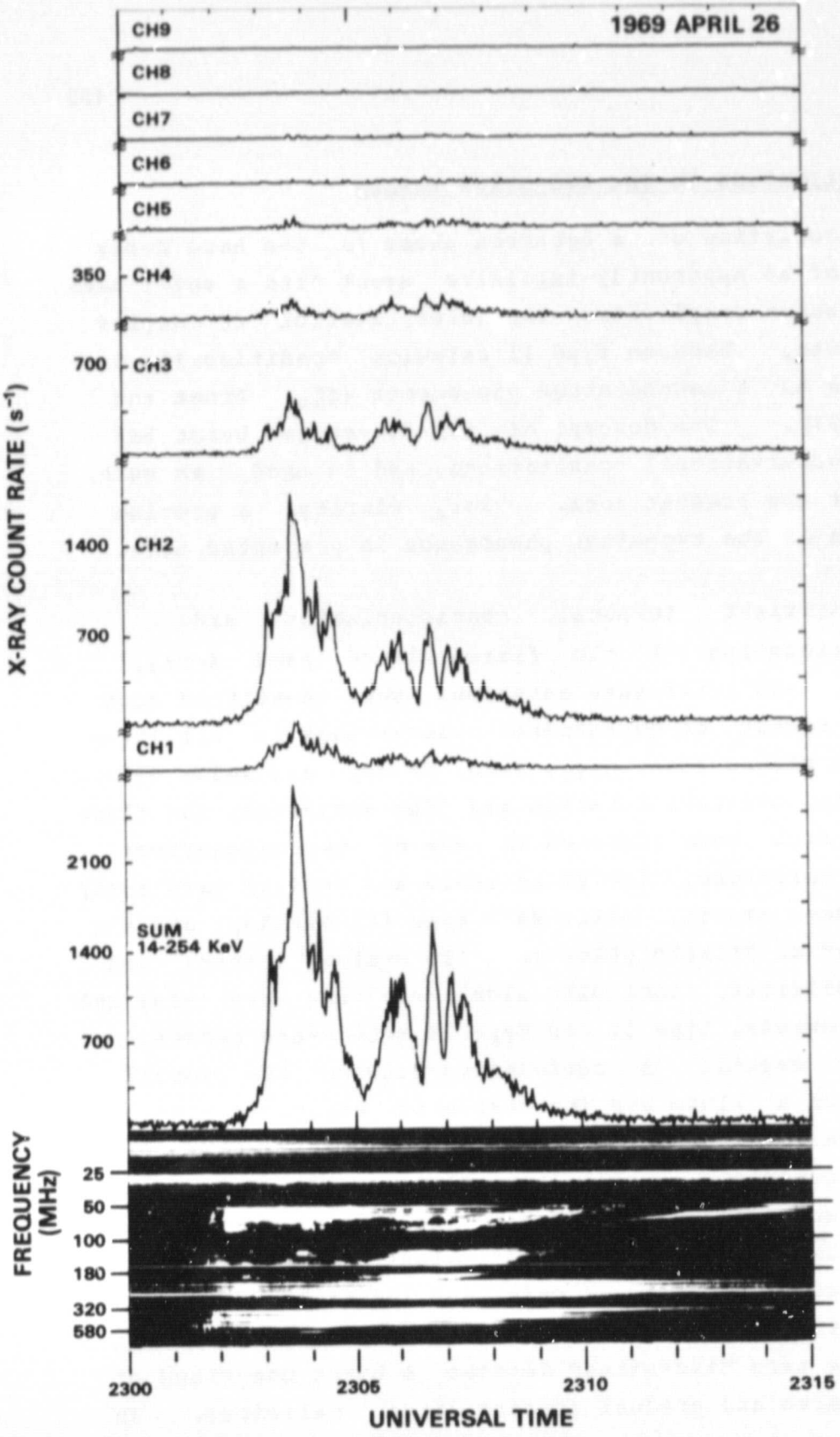

Figure 5-4. Hard X-ray time-intensity profiles for the 1969 April 26 event, together with the 10-580 MHz dynamic spectrum.

5.4 APPLICATION TO THE TWO-STAGE BURSTS

The association of a betatron phase in the hard X-ray emission of an apparently-impulsive event with a meter-wave type II burst complicates the interpretation of complex solar events, because type II emission traditionally is classified as a second-stage phenomenon (Cf. Frost and Dennis 1971). The concept of the two-stage burst has standard observational connotations, and is used, as such, throughout the present work. For, clarity, a precise definition of the two-stage phenomenon is presented here.

The distinct temporal characteristics and interrelationships of the flare-related hard X-ray, microwave, and meter-wave emissions were identified soon after the advent of coordinated observations in all three wavelength ranges (see, e.g., Wild, Smerd, and Weiss 1963). Based on the observed duration and fine structure, the flare emissions each were assigned to one of two categories: impulsive emissions, including rapid and "spiky" hard X-ray and microwave events, meter-wave type III bursts, and the "explosive" or "flash" phase seen in H-alpha flares; and gradual emissions, including slowly-evolving hard X-ray and microwave events, type II and type IV meter-wave bursts, and soft X-ray events. A correlation between the overall magnitude of a flare and its component emissions also was noted: small events tend to be characterized only by impulsive emissions, while large flares often include both impulsive and gradual emissions. The fact that, for these large events, the impulsive emissions invariably were observed before the gradual emissions led to the division of these events into impulsive and gradual phases or stages. Hence, the term "two-stage" denotes a burst comprised of both impulsive and gradual (second-stage) emissions. In

current usage, a two-stage hard X-ray event consists of the initial, impulsive-phase radiation, generally accompanied by other impulsive emissions (*e.g.*, type III bursts and impulsive microwave events), followed by second-stage radiation, generally associated with type II and type IV emission.

The multiply-impulsive bursts, introduced in Chapter 4, were selected solely on the basis of the appearance of the hard X-ray time-intensity profiles (*cf.* Section 4.1), without consulting the coincident coverage at other wavelengths. As noted in the previous section, however, the presence of type II emission appears to be critically associated with both second-stage emission and the presence of betatron acceleration, so a closer look at the morphologically-chosen multiple-spike bursts is required. According to the criteria outlined above, the event of 1969 April 26 is a two-stage event: the initial phase of X-ray emission is associated with type III bursts, while the second stage of X-ray activity is closely associated with a type II burst (see Figure 5-4). Unfortunately, the lack of meter-wave coverage for the May 6 burst prohibits a similar procedure for observational verification as a two-stage event. It is evident that the morphology of the time-intensity profiles for hard X-ray events is not a reliable indicator of the impulsive or non-impulsive character of the emissions; the April 26 and May 6 events "look" as impulsive as the other hard X-ray bursts denoted multiply-impulsive, and do not resemble the "classic" two-stage bursts (for example, Figure 1-1).

The relationship between the two stages of flare-related emissions and the underlying physical processes is poorly-understood, at present. The terms "impulsive-stage acceleration" and "second-stage acceleration" have been

adopted, perhaps too eagerly, to denote the particle-energizing processes in which the impulsive-phase and second stage emissions, respectively, originate. The implication of a one-to-one correspondence between acceleration mechanisms and temporally-associated emissions may not be a viable point of view, considering the complexity of the two-stage phenomena. As suggested by the above discussion of the April 26 event, "spiky" emission structures are not necessarily characteristic of the canonical impulsive-phase acceleration processes alone (see Figure 5-4). On the other hand, flares which produce type II bursts do not necessarily produce significant amounts of associated X-ray emission, attributable to second-stage acceleration.

The betatron process is applied here to reacceleration of the X-ray-emitting electrons, of energies below a few hundred keV. It is crucial to note, therefore, that the betatron-acceleration mechanism considered here is not being tested as a candidate for the elusive "second-stage acceleration" process, which is the hypothetical physical mechanism responsible for very energetic electrons and ions observed in interplanetary space, in association with large solar flares. The possibility that a connection exists between the betatron process and the mechanisms responsible for accelerating electrons and ions to energies in excess of 1 MeV and 1 GeV, respectively, is not ruled out by the present study, and is an intriguing subject for future work.

To better establish the connection between betatron acceleration and second-stage emission, a number of large two-stage bursts were selected from the OSO-5 hard X-ray data and subjected to the same analysis as the multiply-impulsive events (i.e., as described in Section 5.2). The burst selection was aided by K. Frost (GSFC), who had identified many of these two-stage events previously in the

course of his own research (e.g., Frost 1969; Frost and Dennis 1971). The events chosen, and the time periods over which they were tested for betatron acceleration, are listed in Table 5-2.

TABLE 5-2

TWO-STAGE BURSTS TESTED FOR BETATRON ACCELERATION

Event	Date	Test Timespan (UT)
1	1969 February 24	23:12:20 - 23:19:56
2	February 27	13:56:55 - 13:57:58; 13:59:30 - 14:14:58
3	March 1	21:40:40 - 21:49:26
4	March 21	01:49:42 - 01:59:06
5	March 30	02:47:08 - 03:00:00
6	April 26	23:02:58 - 23:09:00
7	May 6	02:38:48 - 02:44:42
8	November 24	09:14:08 - 09:27:52
9	November 27	19:30:19 - 19:39:12
10	1970 July 20	11:21:22 - 11:32:18
11	August 12*	20:18:26 - 20:28:56
12	November 5	03:17:10 - 03:35:00
13	December 11	10:27:35 - 10:31:02
14	1971 January 24*	23:19:15 - 23:36:00

Because the 1969 April 26 and May 6 bursts have been reclassified as two-stage events (see previous section), they are included in the tables and in the discussion of this section for completeness. The events denoted by an asterisk were observed only for part of the entire flare, due to the satellite entering or leaving the Earth's shadow while the flares were in progress.

TABLE 5-3

RESULTS OF BETATRON ANALYSIS AND RELATED CHARACTERISTICS

Event	Start Time of Type II (UT)	Start Time of Betatron Phase (UT)	Best-fit $W_{\perp 0}$	Periodic?
1	2311.5	23:13:09	100	---
2	1404.3	14:04:23	75	No
3	2142.0	21:42:29	100	Yes
4	0150.0	----	---	Yes
5	0250.5	02:50:29	100	Yes
6	2305.5	23:05:56	50	Yes
7	(no coverage)	02:41:04	100	---
8	(no coverage)	09:18:34	100	---
9	1932.0	19:31:19	75	Yes
10	none?(see text)	11:23:54	75	Yes
11	2015.0	----	---	Yes
12	0324.0	03:24:46	100	Yes
13	1030.0	----	---	Yes
14	2315.6	----	---	Yes

Table 5-3 summarizes the results of the test of the betatron model for the two-stage events. The event numbers are used for convenience, and refer to Table 5-2. For each event, Table 5-3 lists, where applicable: the start time of the associated type II emission; the approximate start time and best-fit value of $W_{\perp 0}$ for the betatron phase; and the presence of periodicities found by Lipa (1978) in the hard X-ray emission. Those events for which there is a dashed line in the "Periodic?" column were not analyzed by Lipa (1978). All but one of the 14 hard X-ray events, that of 1970 July 20, were accompanied by type II bursts. It is interesting to note that type III drift pairs were reported for this event (Solar-Geophysical Data Prompt Reports, 1970), a feature which closely resembles weak type-II emission with "herringbone" structure (cf. Kundu 1965). Due

to the scatter of the (F,γ) points throughout the betatron phase, the best-fit start times and values of $W_{\perp 0}$ are empirical estimates only, and should not be taken as precise parameters (see Section 5.5).

To illustrate the properties of the two-stage bursts which contain a stage of betatron acceleration, the (F,γ) plot for Event 9, 1969 November 27, is shown in Figure 5-5. A schematic representation of the general (F,γ) path outlined during this burst is included in the upper-left corner of Figure 5-5, for ease in interpreting the more complex main graph. The time-intensity profile for this event, summed over the nine energy channels from 14 to 254 keV, is shown in Figure 5-6. The impulsive stage, from 19:30:19 to 19:31:19, is distinguished easily, in Figure 5-6, by the lack of the (F,γ) correlation path indicative of betatron action, and by the overall trend, with time, of a significant decrease in the value of γ accompanying a smaller change in F(25). The character of the plot changes at approximately 1931.3 UT, coincident with a minor peak in the X-ray intensity (see Figure 5-6). The three main peaks all fall within a narrow range of F(25) and γ, followed by the development of a smooth path leading from low to high values of both F(25) and γ. The period identified as a phase of betatron action, characterized by the variation of F(25) and γ up and down this path, begins at approximately 19:31:19 UT, and ends at 19:34:56, a duration of 3.6 minutes. Also marked in Figure 5-6 are two (F,γ) paths predicted according to the betatron model (Equation 67), for which the free parameter $W_{\perp 0}$ equals 50 and 100 keV, respectively. Thereafter, the event decay is reflected by the overall tendency towards lower F(25) and higher γ, with the flux reaching the noise level at 19:39:12 UT. With minor variations, this pattern for the overall evolution of the (F,γ) path is exhibited by the other nine betatron

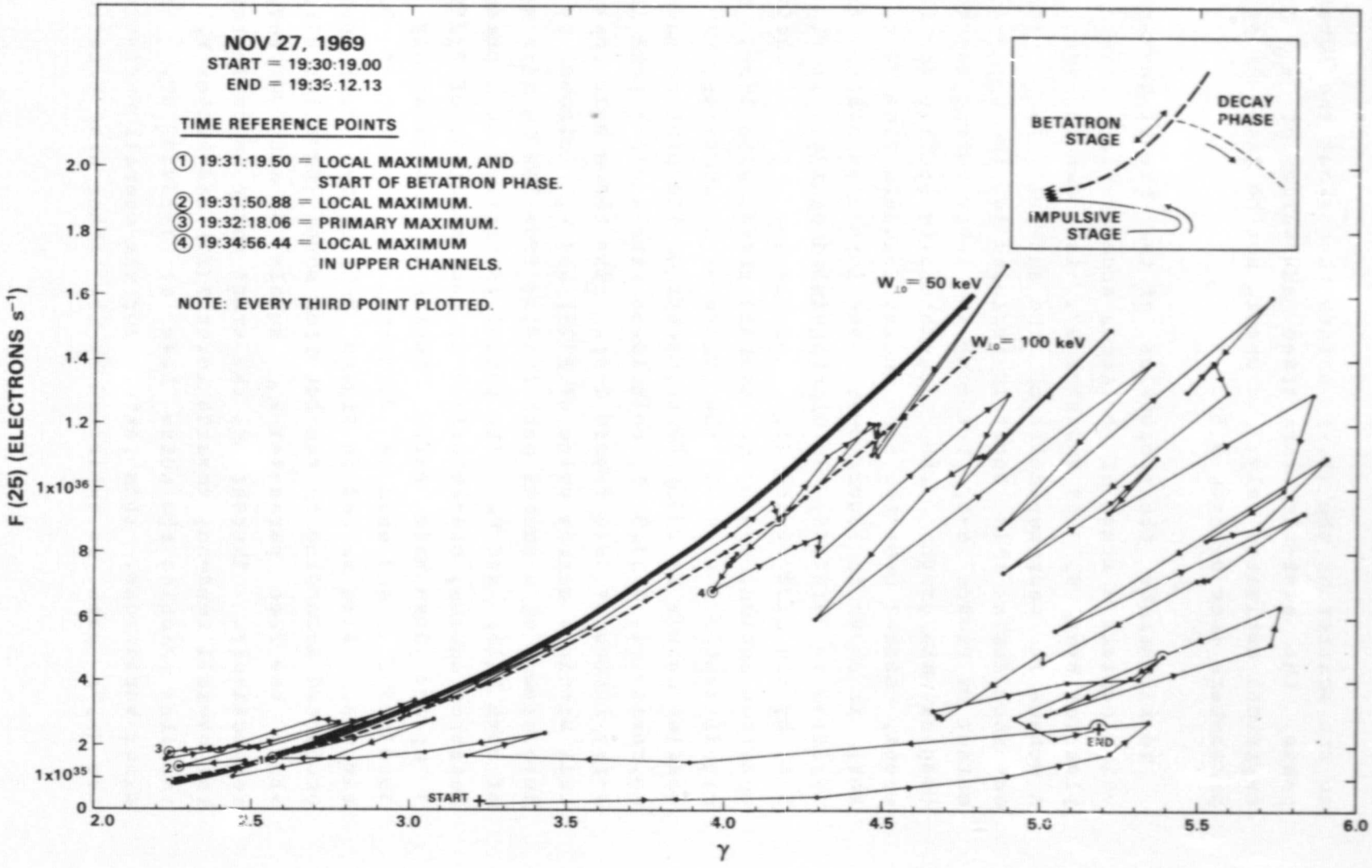

Figure 5-5. The (F,γ) plot for the two-stage betatron event of 1969 November 27.

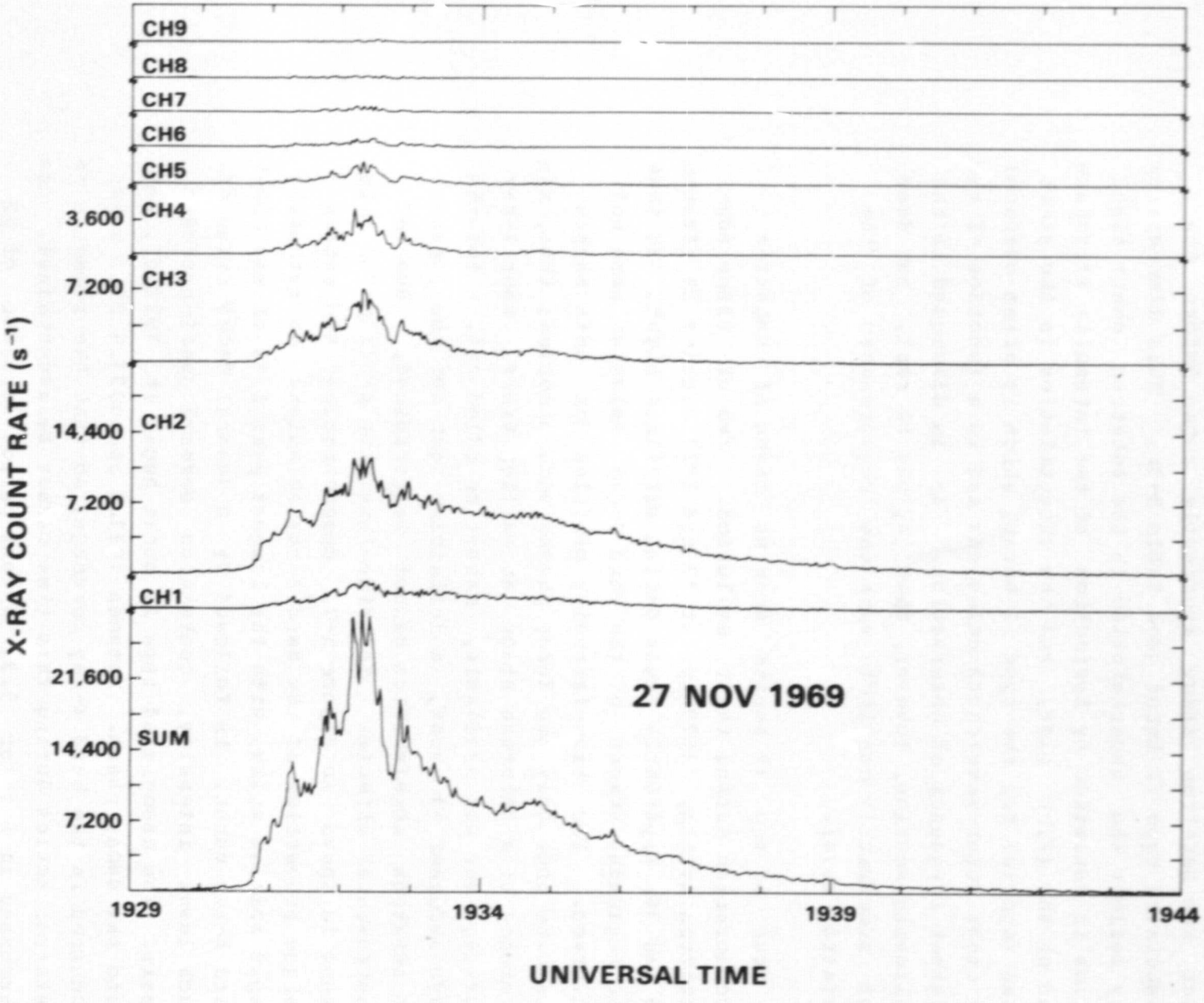

Figure 5-6. Hard X-ray time-intensity profiles for the 1969 November 27 event.

events as well. Event 9 is somewhat atypical, however, in that the betatron stage apparently began before the associated type II burst (see Table 5-3). This discrepancy may reflect the uncertainties in the betatron start time, which is estimated by inspection of the intensity structure and of the (F,Y) plot, and the uncertainties in the start time reported for the type II burst, which is often obscured by other meter-wavelength emissions and is a function of the highest frequency of observation. As is discussed in the following section, however, this gap may be real, but does not necessarily conflict with the requirements of the betatron model.

Four of the 14 bursts show no signs of betatron acceleration during their evolution. Two of these non-betatron events, 1970 August 12 and 1971 January 24 (Events 11 and 14) apparently began during satellite night, so that the beginning stages of the hard X-ray emission were not observed. The time-intensity profiles for both bursts indicate that only the decay phases were observed; thus, the presence of a betatron stage at earlier times, when X-ray coverage was not available, cannot be ruled out. For the 1970 December 11 event, a definitive test for the presence of betatron acceleration cannot be performed, due to instrumental effects. The time-intensity profile for this event is shown in Figure 5-7, demonstrating the rather unique properties of the hard X-ray emission: an extremely rapid initial spike, with the largest peak flux of any OSO-5 hard X-ray burst, is followed by a general decay stage of much lower intensity, containing several quasi-periodic peaks. The associated type II burst began at 1030 UT, well into the decay phase. Between 1031.0 and 1031.9 UT, a gap occurred in the hard X-ray coverage, so that the presence of betatron action during this time cannot be ascertained. As discussed in Section 5.3, a test-period duration of ≥ 2

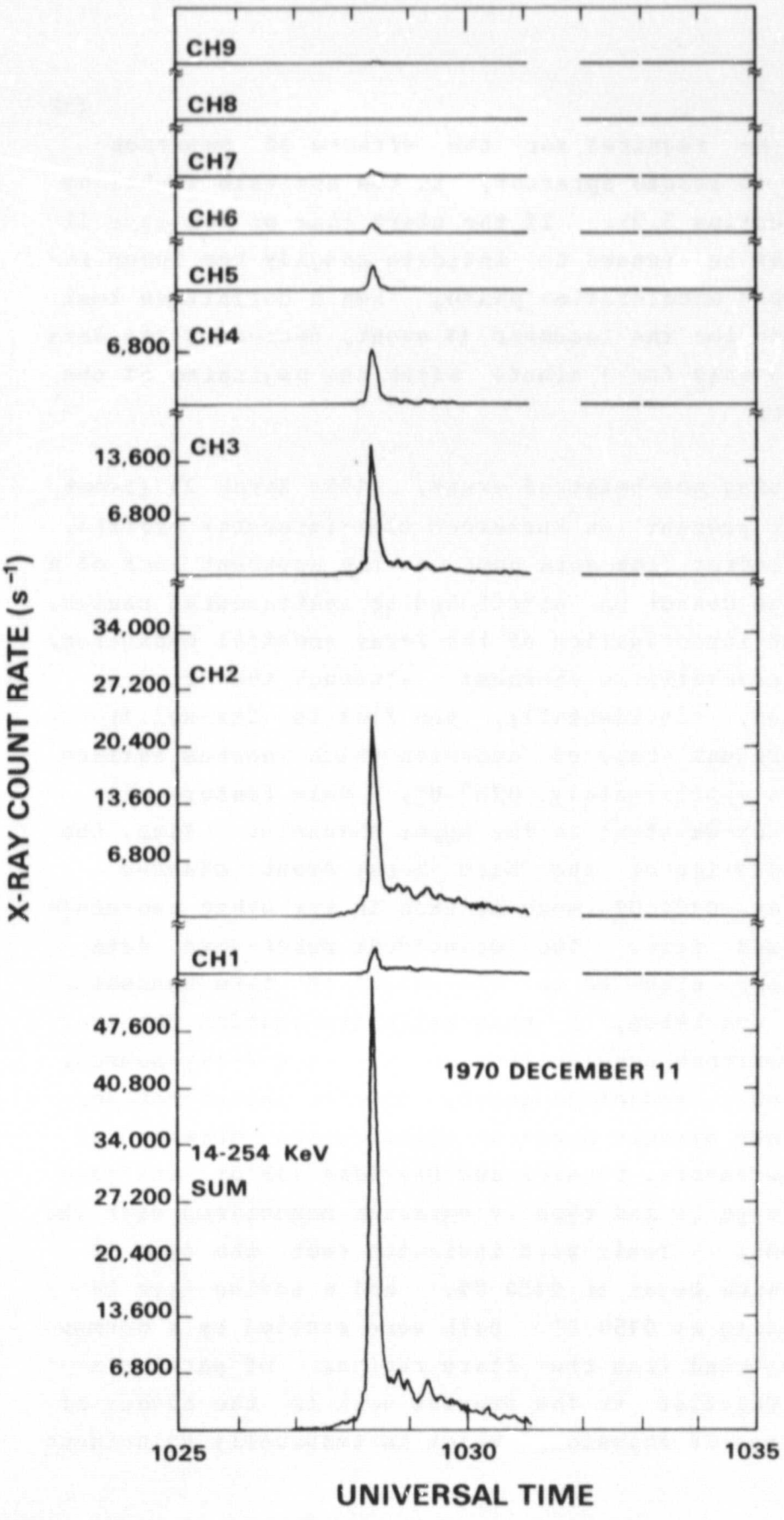

Figure 5-7. Hard X-ray time-intensity profiles for the unusual two-stage event of 1970 December 11.

minutes may be required for the effects of betatron acceleration to become apparent, in the analysis technique used here (Section 5.2). If the start time of the type II emission might be assumed to indicate roughly the inception of the betatron acceleration phase, then a definitive test cannot be made for the December 11 event, because X-ray data were obtained only for 1 minute after the beginning of the type II burst.

The remaining non-betatron event, 1969 March 21 (Event 4), does not present an anomalous time-intensity profile, nor does it suffer from data gaps, so the apparent lack of a betatron stage cannot be attributed to instrumental causes. Upon detailed investigation of the X-ray spectral evolution, a unique characteristic emerges: although the flux in Channel 2 (and, incidentally, the flux in Channel 1) exhibits a gradual stage of emission which reaches maximum intensity at approximately 0157 UT, this feature is practically non-existent in the upper channels. Thus, the spectral evolution of the hard X-ray event changes drastically at ~0154 UT, more so than in any other two-stage bursts analyzed here. The coincident meter-wave data provide further clues as to the origin of this unusual behaviour , and hence, a reasonable explanation for the absence of betatron acceleration in the hard X-ray source. Using the 80-MHz radioheliograph, 158-MHz interferometer, and 10-200 MHz dynamic spectral observations obtained at Culgoora Observatory, Stewart and Sheridan (1970) analyzed the complex type II and type IV emission associated with the March 21 event. Their work indicates that the type II emission, which began at 0150 UT, and a moving type IV burst, beginning at 0154 UT, both were excited by a common shock wave ejected from the flare region. Of particular interest in relation to the present work is the advent of the moving type IV emission, which is temporally coincident

with the start of the "peculiar" hard X-ray phase. It appears that this gradual X-ray emission emanates from the moving type-IV source, and not from electrons which are energized by typical second-stage acceleration processes. Thus, betatron acceleration, which acts on electrons in a stable magnetic trap, would not be expected to apply in the unusual circumstances of the March 21 event. Moving type IV bursts also are associated with Events 1 and 3 (1969 February 24 and March 1) but, in both cases, the radio event began long after the end of the hard X-ray emission (Riddle 1970; Schmahl 1973).

5.5 DISCUSSION

The betatron model has been shown to be generally consistent with observations of several two-stage bursts, and particularly identified as a second-stage phenomenon. In this section, the quantitative properties derived for these events, according to the model, are critically evaluated. The present discussion is concentrated on three aspects of the betatron test results: the significance of the presence or absence of periodicities in the betatron-phase X-ray emission; the duration of the betatron stage; and the comparison between the onset of type II emission and the start of betatron action within the associated X-ray source. These results also are considered in comparison to the "original" betatron event, the great flare of 1972 August 4, using the results reported by Brown and Hoyng (1975), Hoyng (1975), and Hoyng, Brown, and van Beek (1976). At the end of this section, the initial conditions and primary acceleration mechanism assumed by the original betatron model are discussed, and alternative hypotheses are critically evaluated. Brief attention also is devoted to the post-betatron phase of the events under consideration, and to the interpretation of the changes in (F,γ) behaviour which characterize this final phase.

5.5.1 Interpretation of Periodic Behaviour in Two-stage Events

As noted in Section 5.3, the existence of periodicities in the burst emission provides further support for the betatron hypothesis. Multiple periods were identified for those events studied by Lipa (1978), generally within the range 15 to 90 s (see Table 5-4 for relevant events). Unfortunately, Lipa's analysis was not well-suited for evaluating the detailed dynamical evolution of the periodic behaviour; the 14-254 keV fluxes were analyzed in consecutive 190-s segments, with no systematic attempt to partition the bursts according to physically-meaningful criteria (e.g., into impulsive and non-impulsive phases). The results of these Fourier analyses were reported only for 15 of the 28 events studied (Lipa 1978); thus, periods are available for only 5 of the betatron events, although Lipa reported the presence of pulsations in all but one of the 10 betatron flares.

For events 3, 6, 9, and 12, the betatron-acceleration stage is included in a single 190-s test segment, thereby allowing determination of the pulsation frequencies specifically when the betatron mechanism was operating. The reported periods range from 12 to 77 s, and usually differ in value and/or phase from the periodicities found during the non-betatron phase of the same event. Event 10, however, exhibited periodic behaviour before, but not during, the betatron phase. This event (1970 July 20) is anomalous in another respect: no type II emission accompanied the X-ray event. Type IV radio emission, a large interplanetary-proton event, and a microwave post-burst increase all were associated with Event 10, indicating that it is, otherwise, a classic two-stage burst. Event 2, 1969 February 27, is classified as a non-periodic event by Lipa (1978), but was accompanied by a type II burst.

Analysis of a larger set of events, with coincident meter-wave coverage, is necessary for further investigation of the requirements and limitations of the betatron-acceleration mechanism.

Hoyng, Brown, and van Beek (1976) performed a dynamic Fourier analysis of the X-ray emission during the August 4 event. They found significant periods in the 41-53 keV flux of approximately 30, 60, and 120 s during the early stages of the X-ray event, with the lowest frequency (~120 s) persisting for about 5 minutes. Fourier analysis of the spectral evolution also revealed similar periodicities in the spectral index, γ. Assuming that the largest period equals the time required for the initiating disturbance to traverse the trap (see Section 5.3), Hoyng (1975) deduced a scale length of $\sim 5 \times 10^5$ km for the August 4 event. In comparison, the largest period found for a two-stage betatron event, 77 s, yields a scale length of $\sim 3 \times 10^5$ km, assuming the same Alfvén speed; the other betatron events exhibit smaller periods, and thus smaller dimensions. The two-stage events are shorter and less intense than the August 4 burst, so it is plausible that the region in which the X-ray-emitting electrons are trapped might be smaller for the two-stage events as well.

Ideally, the periods evident in the hard X-ray time-intensity profiles should be apparent in the (F,γ) plots as well. The scatter inherent in the derived parameters, however, allows gross estimates, at best, of any periodic variation of $F(25)$ and γ during the betatron phase. Because the magnetic-field oscillations may change in amplitude from cycle to cycle, as was found for the August 4 event (Brown and Hoyng 1975), the maximum "excursion" of the (F,γ) points associated with each oscillation also may vary; as a result, the existence of periodic behaviour is obscured further in

the actual (F,γ) plots. Although the (F,γ) plots themselves cannot be used to establish the existence of periodicities in the X-ray parameters, some indication of periodic behaviour can be obtained from plots of the evolution of the individual quantities, F(25) and γ, as a function of time. For the representative events for which such plots were made, visual inspection yields approximate periodicities, in both F(25) and γ, which are consistent with those derived by Lipa (1978) from the X-ray intensity alone.

It must be noted, however, that the presence of periodicities in the X-ray emission does not guarantee the presence of betatron action. Events 4, 11, 13, and 14 do not appear to include betatron phases, yet all were found to exhibit periodic behaviour in their X-ray emission (Lipa 1978). Furthermore, six of the multiply-impulsive bursts listed in Table 5-1 were found to be periodic (Lipa 1978), but do not include betatron stages. It is clear that the relationship between X-ray pulsations and the betatron mechanism is more complex than initially supposed, and cannot be understood thoroughly within the confines of the simple betatron model as originally proposed by Brown and Hoyng. This problem awaits both theoretical and observational efforts to incorporate more realistic physical conditions and effects into the betatron model, and to develop more rigorous criteria for its applicability to relevant solar phenomena.

5.5.2 Temporal Relationships of the Second-stage Emissions

For the 10 two-stage events found to include a betatron stage, Table 5-4 lists the duration of the betatron-acceleration phase, and the difference between the onset of type II emission and the start of the betatron phase, both in minutes. A negative value for this difference indicates that the betatron action began before the appearance of type

II emission. Comparing the betatron-phase durations to the total X-ray-emission durations, and to the durations of the type II emission, yields no correlation between these timescales.

TABLE 5-4

CHARACTERISTICS OF TWO-STAGE BETATRON EVENTS

Event	Start of Betatron Phase - Start of type II (minutes)	Duration of Betatron Phase (minutes)
1	1.6	4.9
2	0.1	4.1
3	0.5	1.7
5	~0	5.0
6	0.4	2.0
7	---	2.0
8	---	2.7
9	-0.7	3.6
10	(11.4?)	5.4
12	0.8	2.4

The distribution of betatron-phase durations supports the contention, originally suggested in Section 5.2, that the X-ray event must last at least 2 minutes to be identifiable by the present means of analysis. The shortest betatron stage lasted for 1.7 minutes (Event 3), perhaps implying that an event of shorter duration might not be capable of sustaining any betatron action. The longest betatron-stage duration, 5.4 min(Event 10), provides a measure of the lifetime of the trapped electrons, because the lowest-energy particles must remain in the trap as long as the betatron phase is observed to last. The assumption of a collisionally-dominated lifetime for the trapped electrons gives an upper limit on the trap density (*cf.* Hoyng 1975); for a 30-keV electron, the betatron-phase duration of 320 s yields a trap density

of $n_e \leq 2 \times 10^8$ cm^{-3}. In comparison, the densities derived for the single-spike impulsive events by Crannell et al. (1978) range from 2×10^8 to 5×10^9 cm^{-3}, indicating that the single-spike bursts originate in somewhat denser loops than do the two-stage betatron events. A possible explanation for this difference is that the single-spike bursts are located lower in the corona than the two-stage betatron events, since a higher density generally implies greater depth in the solar atmosphere. On the other hand, the spike-burst sources might be denser loops which coexist at comparable heights with the less dense loops of the betatron events. Coincident analysis of hard X-ray and microwave emission provided density estimates for the simple spike bursts studied by Crannell et al. (1978). The application of their technique to several multiply-impulsive events (i.e., of Table 5-1) indicates that the component spikes of the multiple bursts originate in regions whose densities are comparable to those found for the single-spike events. For the two-stage event of 1969 April 26, on the other hand, the densities derived for the sources of the impulsive peaks are consistent with the upper limit on the density of the second-stage source region, according to the aforementioned collision-time argument. The difference in density thus provides a possible explanation for the the apparent restriction of the betatron process to the two-stage bursts alone: the greater densities found for the multiple-spike bursts may prohibit the formation and maintenance of the betatron-acceleration mechanism, within the appropriate source regions.

For the August 4 flare, Brown and Hoyng (1975) found that the betatron phase lasted for nearly the entire event, ~20 min, and that this duration implies a trap density of $n_e \leq 4 \times 10^7$ cm^{-3}. The limited evidence available on large, behind-the-limb flares suggests that the X-ray emission

during intense, long-enduring bursts originates at coronal heights of 25,000 km or more above the photosphere (Kane and Donnelly 1971; Roy and Datlowe 1975; Hudson 1978). Thus, the low upper limit on the trap density, indicating an unusually great height for the X-ray source region, is consistent with the large magnitude, overall, of the August 4 flare.

The betatron model can be evaluated in the context of other physical processes in flares, on the basis of the relationship between the onset of type II emission and the start of the betatron phase. However, some caution must be exercised in interpreting the values listed in Tables 5-3 and 5-4 for the betatron-phase start times and durations. The actual start time of the betatron stage often was difficult to determine, so that the reported value may be inaccurate by as much as 30 seconds. The start times reported for type II bursts also are uncertain by a comparable amount, for the following reasons. The quoted type-II start times always depend on the highest frequency of observation; for example, the Culgoora observatory generally reported start times at $\leq$200 MHz, while the Fort Davis coverage yielded start times at $\leq$580 MHz. Furthermore, certain observatories report start times only to the nearest minute, for publication in the Solar-Geophysical Data Reports. Sensitivity limits also compound the difficulty of quantitatively associating type II bursts with other flare emissions (see, e.g., Smerd and Dulk 1971); a weak type II burst may not be detected at all (perhaps, e.g., the 1970 July 20 event), or, if the intensity of the meter-wave emission increases with time, the event may not appear in the dynamic-spectral records until well after the actual start time.

Adopting the mean value, 0.4 min, as a typical interval between the onset of type II emission and the start of the betatron phase, for the two-stage betatron events, three possible physical pictures emerge:

1) If the type II burst and the oscillation causing the betatron acceleration stem from a common shock front, then the shock wave first sets off the type II emission, travels for ~24 s, then initiates the magnetic-field oscillations responsible for accelerating the trapped electrons in the X-ray source. If the shock travels at the Alfvén speed, $\sim 5 \times 10^3$ km s^{-1}, then the type II burst and the betatron-phase X-ray emission originate approximately 10^5 km apart. The different durations of the interval between the type II onset and the betatron-phase onset thus would indicate a corresponding range in distances between the region in which type II emission first occurs and the X-ray source.

2) If the type II burst and the magnetic perturbation of the loop originate simultaneously, then the 0.4-minute interval between the start of the type II burst and the onset of the betatron phase would correspond to the duration required for the betatron action to significantly affect the character of the observed X-ray emission.

3) The shock wave and the loop oscillations could be caused by <u>different</u> impulses, but related by a common origin. An analogous situation apparently exists for many events with which both type II and type IV emissions are associated: the type II and type IV bursts often travel at significantly different speeds and are located at widely-separated locations, yet both meter-wave phenomena seem to have been initiated by the same flare event (Riddle 1970; Stewart and Sheridan 1970; Robinson 1978). As applied to the betatron model, this hypothesis implies that the main flare triggers

both a shock wave, which initiates the type II burst upon achieving the requisite height, and a slower-moving disturbance (e.g., an Alfven wave) which is responsible for the oscillations of the loop containing the X-ray-emitting electrons.

The limited sensitivity and temporal resolution of the available meter-wave data does not allow a definitive conclusion as to which explanation is most consistent with observations. We note, however, that the observed spread in durations of the interval between start times is interpreted most easily in terms of the third hypothesis.

5.5.3 The Roles of the Initial and Final Electron Distributions

For the 10 bursts found to include betatron phases, the best-fit values of the initial transverse electron energy, $W_{\perp 0}$, range from 50 to 100 keV (see Table 5-2). Due to the relative insensitivity of Equation 67 to the value of $W_{\perp 0}$, the uncertainty in the best-fit values of this parameter may be as much as 50% of the quoted figure, particularly for $W_{\perp 0} \sim 100$ keV. According to Hoyng (1975), this parameter denotes the mean kinetic energy associated with the motion of the electrons perpendicular to the magnetic field immediately prior to the betatron phase, possibly resulting from large-scale electric-field acceleration. In other words, $W_{\perp 0}$ represents the mean transverse energy of the electrons accelerated during the impulsive phase, and subsequently "injected" into the trap wherein betatron acceleration occurs. As mentioned in Chapter 3, the hard X-ray emission originates predominately in electrons with energies between 10 and 100 keV. For the impulsive events analyzed in Chapter 4, the peak temperatures, which essentially represent the mean electron energy during the impulsive phase, range from 20 to 70 keV. Thus, the range

of $W_{\perp 0}$ found for the betatron events, 50-100 keV, appears somewhat higher than is typical for the multiply-impulsive events. The aforementioned uncertainty in the values of W estimated for the two-stage events, however, precludes attributing any significance to the apparent disparity between the multiple-spike burst energies and the energy represented, for the two-stage bursts, by $W_{\perp 0}$.

For the August 4 event, Brown and Hoyng (1975) found the best agreement with observations for $W_{\perp 0} = 15$ keV, significantly lower than was found for the two-stage events. This disparity highlights a problem intrinsic to the original betatron model, concerning the interpretation of $W_{\perp 0}$ in the context of the character of the bremsstrahlung-emitting electrons. If, as stated previously, $W_{\perp 0}$ represents the mean value of the transverse electron energy, then the specific anisotropy of the assumed electron distribution guarantees that the total energy of an average electron cannot be less than $W_{\perp 0}$. Because the low-energy cutoff of the electron spectrum was chosen to be 25 keV, values of $W_{\perp 0}$ which exceed this limit by more than a factor of 2 are incompatible with the basic properties of the power-law electron spectrum. For $W_{\perp 0} >> 100$ keV, additional difficulties arise from the implied inclusion of a significant number of relativistic electrons; the non-relativistic bremsstrahlung formulae used in the present analysis would be invalid for such a distribution. Within the confines of the original betatron model, therefore, it is uncertain whether the best-fit values, $W_{\perp 0} = 50$-100 keV, found for the two-stage events accurately reflect the physical characteristics of the injected electron distribution. This uncertainty might be resolved through further reevaluation of the betatron model, a task which is beyond the scope of the present work.

The most conservative non-thermal emission model, the thick-target interpretation, requires that the acceleration mechanism must be very efficient (cf. Section 3.1.2). This constraint limits the possible impulsive-phase acceleration processes to either direct (induced) electric-field acceleration or wave acceleration by a mode which manifests most of its energy in the electric field, such as electron plasma waves (Smith 1980). The pitch-angle distribution of the electrons accelerated by either method generally is expected to be anisotropic, although the plasma turbulence invariably associated with currently-proposed models for the primary energy-release process may induce temporary isotropization (cf. Spicer 1976). Both types of impulsive-stage acceleration mechanisms have been evaluated by Spicer (1980) and Smith (1980), to determine whether the maximum efficiency attainable in either case is sufficient to account for the requirements of non-thermal flare models. It was found that 0.1% or less of the energy released is imparted to energetic electrons, for both direct electric-field and plasma-wave acceleration mechanisms. Thus, non-thermal emission models may be untenable for the impulsive phase, due to the obvious inefficiency of the possible acceleration methods (see also Section 3.1.2, for other problems with non-thermal models). An alternative acceleration process, bulk energization of the ambient electrons, initially yields a predominately isotropic pitch-angle distribution; inevitably, this becomes anisotropic as a result of the loss-cone instability and other plasma effects (Spicer 1976). Within the confines of the original betatron model, it is not feasible to consider the ramifications of the formation and maintenance of a loss cone, because Brown and Hoyng assumed an "ideal" trap without precipitation. It is of interest, nevertheless, to investigate the effects of a different pitch-angle distribution (that is, one other than that specified by

assuming a mean $W_{\perp 0}$ for all injected electrons) on the observable manifestations of the betatron process.

To demonstrate the results obtained for the diametrically opposite situation, a constant value for $W_{\parallel 0}$, representing the mean initial energy of the injected electrons parallel to the magnetic-field direction, is adopted. The derivation of Equations 59 through 67 then is repeated, taking into account the assumption of constant $W_{\parallel 0}$, to arrive at a result which can be compared directly to the original model predictions.

The initial power-law electron spectrum (Equation 58) and the formula for the total energy, per electron, as a function of b and $W_{\parallel 0}$ (Equation 53) yield the following expression for the electron spectrum resulting from the betatron action on the initial electron distribution:

$$f'(W,b) = (\delta_0 - 1)\,(N_0/W_1)\,(b+1)^{\delta_0 - 1}\,[\,(W + bW_{\parallel 0})/W_1\,]^{-\delta_0} \quad , \qquad (68)$$

where the parameters b, δ, N_0, and W_1 remain as defined previously. Thus, after Equation 60,

$$N'(t) = N_0\,(b+1)^{\delta_0 - 1}\,[\,1 + (bW_{\parallel 0}/W_1)\,]^{-\delta_0 + 1} \quad . \qquad (69)$$

It is evident, from Equation 68, that the exponent of the energy-dependent term in the new electron distribution, $f'(W,b)$, is identical to that derived for the original betatron model (Equation 59). Therefore, the same general expression applies for the definition of the effective spectral index, δ, found by approximating the electron spectrum by a power law; that is,

$$\delta(b) = \delta_0 / [\,1 + (bW_{\parallel 0}/E_1)\,] \quad , \qquad (70)$$

where E_1 is the lowest energy of observation, as before. Using Equation 62 and 70, the quantity b is expressed as a function of γ, E_1, and $W_{//0}$, as follows:

$$b = -(\gamma-\gamma_0)\, E_1 / (\gamma-1/2)\, W_{//0} \qquad (71)$$

Note that this expression differs in sign from Equation 65. Equations 64, 69, and 71 thus yield the predicted (F,γ) correlation for the "revised" betatron model, in which the initial electron pitch-angle distribution is peaked in the direction perpendicular to the magnetic field and can be characterized by a fixed $W_{//0}$:

$$\frac{F(W_1)}{F_0(W_1)} = \frac{(\gamma-3/2)}{(\gamma_0-3/2)} \left\{1- \frac{(\gamma-\gamma_0)\, E_1}{(\gamma-1/2)\, W_{//0}}\right\}^{\gamma_0-1/2} \left\{1- \frac{(\gamma-\gamma_0)\, E_1}{(\gamma-1/2)\, W_1}\right\}^{-\gamma_0+3/2} . \qquad (72)$$

Substituting the values E =28 keV and W =25 keV, as before, into Equation 72 provides the following formula for the predicted behaviour of F/F :

$$\frac{F(25)}{F_0(25)} = \frac{(\gamma-3/2)}{(\gamma_0-3/2)} \left\{1- \frac{(\gamma-\gamma_0)\, 28}{(\gamma-1/2)\, W_{//0}}\right\}^{\gamma_0-1/2} \left\{1- \frac{(\gamma-\gamma_0)}{(\gamma-1/2)}(1.12)\right\}^{-\gamma_0+3/2} . \qquad (73)$$

Comparing Equations 67 and 73, we note that the middle terms of the two expressions differ significantly: the γ-dependent portions evince opposite signs, and there is an exponent of $(\gamma_0-1/2)$ in Equation 73 which is absent in Equation 67. The first and last terms of Equations 67 and 73 are identical, however, except for their respective initial parameters, $W_{\perp 0}$ and $W_{//0}$. The constant-$W_{//0}$ version of the betatron model differs from the original version in two crucial aspects: the new correlation curve (Equation 73) defines a path from high values of F(25) and low values of γ

to low F(25) and high γ; and, as the magnetic field increases, the spectral index decreases (Equation 71).

The important question is, of course, which case provides better agreement with the X-ray observations? To investigate this issue, the procedure for determining the applicability of the betatron model to the X-ray data, described in Section 5.2.2, was applied to the 10 betatron events, using Equation 73 instead of Equation 67 to characterize the model predictions. For all 10 events, the original model was found to yield significantly better agreement with the (F,γ) plots derived from observations, regardless of the tested values of $W_{\#0}$. A combination of the two cases cannot be ruled out entirely on the basis of the present analysis, however, and may provide a reasonable fit to the data for some events.

The significance of these analytical manipulations must be evaluated, in the context of the implications for the impulsive-phase acceleration mechanism. As stated above, the spectral behaviour which would result from the injection of an initial, anisotropic pitch-angle distribution characterized by a constant value of $W_{\#0}$ does not agree with the parameters derived from observations, for the two-stage events studied; thus, any acceleration process which injects electrons with a pitch-angle distribution of this type is incompatible with the X-ray observations. This anisotropic distribution also is at variance with present-day attitudes towards theoretical treatments appropriate to the impulsive stage; current models of impulsive-stage acceleration mechanisms generally discount the possibility of producing pitch-angle distributions which are strongly directed perpendicular to the magnetic-field lines. A completely isotropic distribution cannot yield the observed curvilinear correlation of F(25) and γ, because the betatron-

acceleration process merely will change F(25) but not the spectral index. Hence, only the initial electron population characterized by a constant W_{10} yields agreement between the predictions of the betatron model and the derived properties of the observed X-ray emission.

The end of the betatron phase often is delineated, in the (F,γ) plots, as clearly as the onset of the betatron action. This definite change in the observed X-ray characteristics must represent a corresponding change in the emitting electron distribution, due to alterations in the underlying physical process or in the trap environment itself. The evolution of the post-injection electron population can be inferred from the behaviour of F(25) and γ during and after the betatron phase. A gradual trend seen in the (F,γ) plots for several of the two-stage events, comprising a systematic "flattening" of the apparent correlation path during the later portions of the identified betatron phase, thus might be attributable to some progressive and non-reversible change in the trapped electron distribution. This trend generally is followed by a distinct "decay" phase, during which the X-ray intensity decreases monotonically and slowly. In the (F,γ) plane (see Figure 5-5), the decay is delineated by a trend toward lower values of F(25) and higher values of γ. Although this stage is not essential to the main thrust of the present work, it is of interest to speculate briefly on the possible explanations for the observed behaviour. Collisional losses from the trap, overall expansion of the trap, and Fermi acceleration of the trapped electrons all have been shown to induce (F,γ) patterns which differ markedly from the observed decay-phase path (cf. Brown and Hoyng 1975; Brown and McClymont 1976). The only reasonable mechanism which can produce the observed (F,γ) behaviour is continual leakage of the high-energy electrons from the trap, which would cause the total number

of trapped electrons to decrease as the spectrum softens. Within the confines of the present work, the concepts developed above cannot be tested further. However, these ideas provide a foundation for future investigation of the betatron model, particularly for studying the relationship between the impulsive-phase acceleration mechanisms and the ensuing betatron-acceleration process, for those events in which the appropriate physical conditions obtain.

5.6 CONCLUSIONS

Through the analyses presented in Sections 5.3 and 5.4, the association of betatron acceleration with second-stage X-ray emission has been established. As shown by the application of the criteria for the presence of betatron action to a set of multiply-impulsive events, this process is not present in the impulsive stage. The absence of betatron acceleration in the impulsive phase was verified further by the application of a similar test to a set of two-stage events: the impulsive phases of these events showed no signs of betatron acceleration. As a result, the betatron-acceleration mechanism cannot account for the multiply-peaked structure observed in impulsive events.

Conversely, for the majority of the two-stage bursts studied, the second-stage emission includes a phase which is consistent with the predictions of the betatron model. The present study thus provides strong support for the applicability of the betatron model to second-stage acceleration processes. Whereas the original betatron model (Brown and Hoyng 1975) was applied only to a single burst of somewhat anomalous properties, the analysis presented in this chapter has successfully identified the presence of betatron action in a set of 10 hard X-ray events, all classified as two-stage or "extended" (*cf.* Hoyng 1975) bursts. Furthermore, the presence of betatron acceleration

during the first few minutes of the second-stage emission suggests a fundamental association between betatron acceleration and the physics of the second stage. The study of several two-stage bursts, found to be consistent with the betatron model, also enabled the detailed investigation of the nature of the betatron process and related phenomena, as actually occur under solar-flare conditions.

It is to be hoped that the present results will provide the impetus for further investigation of the applicability of betatron acceleration to second-stage phenomena. The recent advent of hard X-ray data with better temporal and spectral resolution than was available during the previous solar maximum, combined with improved radio coverage, enables a more rigorous test of the betatron hypothesis for a larger set of events. Coincident, but independent, estimates of the densities in the sites most likely to contain magnetic traps also would prove invaluable in determining whether conditions in the solar atmosphere actually are favorable for the betatron process. The relationship between the pulsations identified in many of the betatron events and the oscillations required by the betatron-acceleration mechanism also must be established, preferably through analysis of coincident X-ray, microwave, and meter-wave data.

One important aspect of the betatron mechanism was not considered in the original model, and, hence, was neglected in the present work: the effects of the betatron-acceleration process on the second-stage microwave emissions. The nature of the relationship between the associated hard X-ray and microwave bursts is highly controversial, particularly as regards the relative locations of the respective source regions. The ramifications of the betatron mechanism for second-stage

microwave radiation are equally uncertain: if the hard X rays and microwaves originate in a common source region, then one might expect that the betatron action could produce coincident effects (*e.g.*, periodic intensity and spectral variations) on the emissions observed in both wavelength ranges. The hard X rays emanate from lower-energy electrons than do the microwaves (see Section 3.2.3); because the betatron process accelerates the higher-energy electrons proportionately less than those at lower energies, the magnetic oscillations might not yield any measurable effects in the microwave observations. On the other hand, the gyrosynchrotron intensity, itself, is a function of the local magnetic-field strength (see, *e.g.*, Equation 46); consequently, the microwave emission may exhibit periodic or quasi-periodic variations as a direct result of the loop oscillations.

It is clear, from these tentative suggestions, that intensive theoretical research into possible manifestations of the betatron process in second-stage microwave emission is necessary for extended evaluation of the betatron model; comparison of the resultant predictions with high time-resolution microwave data and with simultaneous hard X-ray observations then will allow more rigorous testing of the model for consistency with actual solar events. The second stage of particle acceleration is poorly understood, at present, despite nearly three decades of theoretical and observational research. It is crucial, therefore, that any promising concepts, such as the betatron model, be considered seriously as potential explanations for this complex phenomenon.

Chapter 6

CODA

"The great tragedy of Science -- the slaying of a beautiful hypothesis by an ugly fact."
T.H. Huxley, presidential address, British A.A.S., 1870.

In the present work, as so often occurs in scientific research, new questions have arisen nearly as rapidly as the original questions have been answered. This summary is intended to recapitulate the initial problems and the solutions proposed through the research discussed in Chapters 4 and 5, as well as to outline those new areas of inquiry indicated as promising subjects for future investigations. These remarks particularly attain timely importance in relation to the currently-operating Solar Maximum Mission (SMM) satellite, and the coordinated ground-based observations organized under the aegis of the Solar Maximum Year (SMY).

Two primary questions, of fundamental relevance to impulsive solar phenomena, were addressed in Chapter 4: what are the causes of multiplicity in impulsive emissions; and how do the physical mechanisms responsible for the multiple-spike bursts compare with those associated with their simple counterparts, the single-spike bursts (Crannell *et al.* 1978)? In the context of these questions, the investigation was focussed on the behaviour of the emission sources within a set of impulsive events, selected from the OSO-5 hard X-ray data, with particular attention to potential indications of "elementary" structure or structures (*e.g.*, analogous to the "elementary flare bursts" of van Beek, de Feiter, and de Jager 1974).

As described in Chapter 4, the magnetic-field structure and hence, the spatial structure of impulsive burst sources can be inferred through joint analysis of hard X-ray and microwave emissions. The approach utilized in this work was necessitated by the lack of pertinent observations with any spatial resolution during the previous solar cycle. Two classes of multiply-impulsive events have been identified: events whose component spikes originate in a single location, and events in which groups of component spikes originate in separate locations. For the latter class of events, a prime cause of multiplicity has been established: the separate groups of emission peaks are due to separate source regions, flaring sequentially. For the former class of events, and for each individual group of spikes within the events with multiple sources, however, an additional mechanism is required to explain the observed multiplicity.

In part, the impetus for the analysis described in Chapter 5 was the necessity of finding an alternate process capable of inducing multiply-peaked emissions. In the present work, the betatron-acceleration hypothesis, originally proposed to account for the observed characteristics of the 1972 August 4 event (Brown and Hoyng 1975), was chosen as a promising candidate for explaining multiplicity in those impulsive events without multiple source locations. As stated in Chapter 5, it was found that the betatron model is not consistent with the observed X-ray properties of the multiple-spike bursts, therefore eliminating this mechanism as a viable means for obtaining multiplicity in impulsive X-ray emissions.

The initial questions regarding the nature of multiplicity thus have been answered, in part, and unanswered, in part. By eliminating the betatron hypothesis as a cause of multiple emissions from a single source

region, progress has been made towards identifying the physical processes applicable to the unsolved portion of the initial queries. During the present solar maximum, critical tests of the results of the study presented in Chapter 4, as well as extended investigations of other mechanisms for multiplicity in impulsive emissions, can be performed with greater depth than before. Suggestions for new observations and theoretical approaches for studying burst multiplicity are outlined in the following paragraphs, with particular reference to relevant, recent results from SMM and SMY coverage.

Microwave interferometry now provides the capability to determine the spatial structure of multiply-impulsive events, with arc-second resolution, as well as the evolution of this structure, with at least 10-second time resolution. Preliminary results, presented at the Stanford SERF workshop (August 1980) by G.A. Dulk, G.J. Hurford, and M.R. Kundu, indicate that impulsive microwave events do, indeed, comprise the two categories identified in the present work. Unfortunately, X-ray imaging at energies above 30 keV is not available at present; the hard X-ray imaging spectrometer (HXIS) on board the SMM satellite can obtain burst images over the energy range 3 to 30 keV, but only the most intense events can be detected with certainty at the highest energies.

In a sense, the HXIS observations and coincident microwave interferometric coverage "bracket" the energy range most relevant to the hard X-ray-emitting electrons; spatial information thus can be obtained for the electrons at energies below 30 keV and above 100 keV. Caution must be exercised, however, in naively interpolating between these two sets of positional and spectral data to infer the locations of the associated hard X-ray sources. An

intriguing case, which also illustrates potential pitfalls of such data interpretation, was the subject of lively debates at the recent SERF workshop: an impulsive event, observed with the HXIS instrument and the VLA interferometer, exhibited a single microwave source located between two, widely-separated sources of 3 to 30 keV emission. The source of the associated hard X-ray burst could be co-spatial with the microwave source, with one or both of HXIS sources, or even located separately from both the radio and the softer X-ray sources; the observations simply do not give sufficient direct information to resolve this issue for the event under consideration. The theoretical possibilities are equally confusing: if the microwaves were emitted from the top of a loop, and the 3 to 30 keV X ray from the footpoints thereof, then some mechanism must exist whereby the highest-energy electrons (>100 keV) would be confined strongly to the upper portions of the arch, while the lower-energy electrons would be permitted to stream freely down the legs. Brown, Melrose, and Spicer (1978), however, have shown that the the opposite situation is more feasible: the most energetic electrons will not be trapped, if the initial flare heating occurs at the top of a loop. One must keep in mind, also, that a "typical" flare does not exist, and that it is dangerous to generalize from a single event, as is so frequently done, for example, with the flare of 1972 August 4.

It is evident that the issues of multiple source locations and co-spatiality of impulsive emissions is far from being resolved. The philosophy behind the SMM satellite and associated SMY coverage ideally provides the most productive approach for unravelling the spatial complexities of solar activity. Due to the present lack of solar-dedicated experiments designed to spatially resolve hard X-ray emissions, however, these questions probably will

remain unanswered at the end of the present solar maximum. As pointed out by the Hard X-ray Imaging Facility Definition Team (Cf. Hurford 1977), the technological capability exists, at present, to build instrumentation suitable for monitoring solar flares over the energy range from tens to hundreds of keV, with arc-second spatial resolution and good temporal resolution. It is to be hoped that such experiments will be prime candidates for inclusion in future instrument packages designated for the Space Shuttle program, or even for operations based on orbiting space platforms. Full comprehension of the complex, evolving structure underlying emission structures in flares can be achieved only through coordinated observations over the hard X-ray, microwave, and other pertinent portions of the electromagnetic spectrum, all with comparable spatial and temporal resolution.

The betatron-model analysis of Chapter 5 provided a bridge between the abovementioned issues of impulsive multiplicity and the broader problem of interpreting both impulsive and associated gradual emissions within a self-consistent framework. The betatron-acceleration process is an attractive candidate for application to complex bursts, for two reasons: a mechanism for obtaining periodic, or quasi-periodic, multiple emissions is an integral feature of the model; and, the low-density environment and repeated reaccelerations characteristic of this process provide favorable circumstances for the production of large, long-enduring events. The first feature (i.e., the production of multiplicity) suggested applicability to the multiply-impulsive events; as mentioned previously, however, it was found that the multiplicity of the complex spike bursts cannot be attributed to the betatron process. The second feature (i.e., the capability of supporting extended emissions) yielded more intriguing, and more significant,

results, thus necessitating a shift in the emphasis of the inquiries upon which the model evaluation was focussed.

The following questions, of basic relevance to complex solar bursts, were addressed in Chapter 5: what physical process (or processes) is responsible for the observed properties of the intense, extended, hard X-ray emission characterizing the two-stage events; and is there a relationship between the associated impulsive and gradual emissions, indicating a more fundamental relationship between the physical mechanisms involved in the respective phases? To investigate these issues, the applicability of the betatron-acceleration process to gradual, second-stage hard X-ray emission was tested qualitatively, for several two-stage events observed with OSO-5. As a result of this endeavour, the betatron mechanism has been identified as a viable explanation for second-stage hard X-ray emission, particularly during the initial few minutes of that stage. In general, the distinction between the impulsive and gradual emission stages is delineated quite clearly by the absence or presence, respectively, of this process, thus yielding a classification method which is far more accurate than using morphological criteria alone.

New questions have arisen, as well, in the course of this work. The research described in Chapter 5 was handicapped by the limited coverage and poor (or non-existent) temporal, spatial, and spectral resolution of the observations obtained during the previous solar maximum. These problems have been alleviated greatly by the improved instrumentation now implemented at many ground-based observatories, and by the state-of-the-art instrumentation and pointing capabilities of the SMM experiments and the spacecraft itself. Hence, observations of two-stage events obtained during the present solar maximum will enable a more

comprehensive evaluation of the betatron hypothesis, and more detailed studies of those aspects of the model which could not be investigated thoroughly in the present work. In particular, several vital questions are outlined in the following paragraphs, together with suggestions for timely observational theoretical approaches for attacking these problems.

With the Gamma-Ray Experiment (GRE) on board the SMM satellite, the behaviour of both electrons and ions at energies in the range from 100 keV to tens of MeV can be investigated. Several events which exhibit high-energy "tails" extending into the MeV range have been observed to date (J. Ryan, presented at the Stanford SERF workshop, August 1980); these events are of particular interest to the two-stage issue, because they do not necessarily obey the classical concept of two-stage emission implying two stages of acceleration. The GRE observations thus can provide information crucial to evaluating the connection between betatron acceleration and the elusive second-stage acceleration process, believed to be responsible for the very high-energy interplanetary particles. In the context of the high-energy aspects of the betatron model, it is important to determine the potential effects of the betatron mechanism on the nuclear particles which produce gamma-ray line and continuum emission, and to extend the observational analysis of two-stage betatron and non-betatron events into the gamma-ray range.

The relationship between the betatron-influenced X-ray phase and the associated emissions at other wavelengths, such as extended microwave bursts and type II events, has been treated only briefly in the present work. The existence of a connection between the impulsive and gradual phases of emission, in the context of the initial conditions

of the betatron hypothesis, also remains an open question. The derivation of the betatron model implicitly includes a dependence on the form of the initially-injected electron distribution, thus introducing a dependence on the impulsive-acceleration process into the physics of the second stage. These issues can best be addressed through use of hard X-ray, microwave, and meter-wave coverage of both impulsive and gradual emissions to investigate temporal, spatial, and spectral relationships between the associated radiations, thus obtaining information on possible relationships between the underlying acceleration mechanisms.

The present work provides significant clarification of the physical mechanisms responsible for multiplicity in impulsive emissions, and introduces the betatron-acceleration mechanism as a viable second-stage phenomenon. It is hoped that these results will provide both a stimulus and a useful foundation for future research into the fascinating physics of complex solar-flare emissions, during the current solar maximum and beyond.

Appendix A

A LISTING OF THE PROGRAM USED TO CALCULATE F(25) AND

```
C********THE PROGRAM "CALGAMA" CALCULATES THE INSTANTANEOUS*********
C******VALUES OF THE SPECTRAL INDEX,GAM, THE ELECTRON PRODUCTION***
C******RATE,F(E,T), AND THE ENERGY DEPOSITION RATE,R(E,T),DURING*****
C*****************A HARD X-RAY EVENT.*************************************
      REAL*4 LT
      DIMENSION N(9),DCB(9),CB(9),C(9),CAL(9),E(9),P(9)
      DIMENSION GAMMA(9),DG(9),AL(9),DC(9)
C     NOTE: THE FOLLOWING VALUES OF CAL ARE FOR EVENTS
C       BEFORE 26 OCT 69 ONLY!
C       DATA CAL/0.097,0.00119,7.42E-4,6.34E-4,0.00060,6.96E-4,6.41E-4,
C      X8.94E-4,8.23E-4/
C     NOTE: THE FOLLOWING VALUES OF CAL ARE FOR EVENTS
C       AFTER 26 OCT 69 ONLY!
      DATA CAL/0.371,0.00131,7.42E-4,6.34E-4,0.00060,6.96E-4,6.41E-4,
     X8.94E-4,8.23E-4/
      DATA ASTR/'*'/
      READ(5,4) HEND,MEND,SEND
    4 FORMAT(2I2,F5.2)
      WRITE(6,1) HEND,MEND,SEND
    1 FORMAT(' ',2I2,F5.2)
C   THE PREFIX "D" DENOTES THE UNCERTAINTY IN A VARIABLE.
C     CB(J)=BACKGROUND IN PHOTONS/CM2-SEC-KEV PER CHANNEL J
C     N(J),P(J) = COUNTS PER CHANNEL J
C     C(J)=EVENT COUNTS PER CHANNEL J(ABOVE BKGD.)
C     Q,LT=LIVE TIME IN MILLISECONDS,SECONDS
      READ(5,5) (CB(J),J=1,9)
    5 FORMAT(9(F7.5,1X))
      WRITE(6,2) (CB(J),J=1,9)
    2 FORMAT(' ',9(F7.5,1X))
      READ(5,6) (DCB(J),J=1,9)
    6 FORMAT(9(F6.0,1X))
      WRITE(6,3) (DCB(J),J=1,9)
    3 FORMAT(' ',9(E7.2,1X))
      GF=0.35
      GF1=GF+1.
    7 WRITE(6,990)
  990 FORMAT(1H0)
   11 READ(2,10,END=33) HOUR,MIN,SEC,PARAM,Q,(N(J),J=1,9)
   10 FORMAT(8X,I3,I2,F5.2,7X,A1,8X,F4.0,4X,3I4,2I3,4I2)
      IF(MIN.NE.MEND) GO TO 31
      IF(SEC.GE.SEND) GO TO 33
   31 CONTINUE
      IF(PARAM.EQ.ASTR) GO TO 11
      WRITE(6,40) HOUR,MIN,SEC,PARAM,Q,(N(J),J=1,9)
   40 FORMAT(1H0,8X,I3,I2,F5.2,7X,A1,8X,F4.0,4X,3I4,2I3,4I2)
      IF(N(3).GT.N(2)) GO TO 7
      DO 12 J=1,9
   12 P(J)=FLOAT(N(J))
      LT=Q*.001
      TEST=CB(2)+DCB(2)*5.
      Z=(P(2)/LT)*CAL(2)
      IF(TEST.GT.Z) GO TO 7
      JMAX=1
      DO 14 J=1,9
      DC(J)=SQRT(P(J))/LT*CAL(J)
      DC(J)=SQRT(DC(J)**2+DCB(J)**2)
      C(J)=(P(J)/LT)*CAL(J)-CB(J)
      IF(J.EQ.1) GO TO 15
      IF(C(J)-DC(J)) 16,16,15
   16 IF(JMAX.NE.1) GO TO 15
      JMAX=J-1
```

```
      GO TO 14
   15 DC(J)=DC(J)/C(J)
      IF(JMAX.EQ.1.AND.J.EQ.9) JMAX=9
   14 CONTINUE
      WRITE(6,140) JMAX
  140 FORMAT(1H ,'JMAX=',I2)
      WRITE(6,69)  (C(J),J=1,9)
      WRITE(6,69)  (DC(J),J=1,9)
   69 FORMAT(1H ,9F10.4)
      IF(JMAX.LT.3) GO TO 7
      E(1)=22.
      E(2)=38.
      E(3)=65.
      E(4)=93.
      E(5)=122.
      E(6)=151.
      E(7)=179.
      E(8)=210.
      E(9)=236.
C  CALCULATE THE INSTANTANEOUS" MEAN SPECTRAL INDEX,GAM.
C   USING ONLY CHANNELS 3 AND 4.
      IF(JMAX.GT.3) JMAX=4
      DO 63 J=3,JMAX
      ALE=ALOG(E(2)/E(J))
      GAMMA(J)=ALOG(C(J)/C(2))/ALE
      DG(J)=ABS(1.0/ALE*DC(J))
   63 CONTINUE
      GAM=0.0
      GGM=0.0
      DO 64 J=3,JMAX
      GG=1.0/DG(J)**2
      GAM=GAM+GAMMA(J)*GG
      GGM=GGM+GG
   64 CONTINUE
      GAM=GAM/GGM
      CALL GMMMA(0.5,GX,IER)
      X=GX
      CALL GMMMA(GAM,GX1,IER1)
      Y=GAM-.5
      CALL GMMMA(Y,GX2,IER2)
      WRITE(6,330) GAM,GX1,IER1,GX2,IER2
  330 FORMAT(1H ,5E10.4)
      BETA=X*GX2/GX1
  331 FORMAT(1H ,'  BETA=',F10.4)
      WRITE(6,331)  BETA
      A=C(2)*(E(2)**GAM)
      F=2.0E+33*A*BETA*((GAM-1.)**2)/(25.**GAM)
      R=4.0E-9*GAM*F/(GAM-1.)
      WRITE(6,70)  (E(J),J=1,9)
      WRITE(6,71)  A
   71 FORMAT(1H ,'  A=',E10.3)
   70 FORMAT(1H ,'MIDPOINT ENERGIES=',9F9.2)
C  CALCULATE THE DEGREES OF FREEDOM,NFRE, AND CHI**2 VALUES
C  FOR THE MEAN TEMPERATURE AND MEAN SPECTRAL INDEX.
      NFRE=JMAX-3
      CHI2G=0.
      CHI2=0.
      IF(NFRE.EQ.0) GO TO 29
      DO 28 J=3,JMAX
      WRITE(6,27) J,GAMMA(J),DG(J)
   27 FORMAT(' ','GAMMA(',I1,')=',F6.2,1X,'+/- ',F5.2)
   28 CHI2G=CHI2G + (GAM-GAMMA(J))**2/NFRE/DG(J)**
   30 FORMAT(1H0,'   GAM =',F8.2,5X,' CHI2G=',F8.2)
   29 CONTINUE
      WRITE(6,30) GAM,CHI2G
      WRITE(6,332)  F,R
  332 FORMAT(1H0,' F(E,T)=',E9.2,5X,'R(E,T)=',E9.2)
      GO TO 7
   33 CONTINUE
      STOP
      END
```

REFERENCES

Acton, L.W. 1964, Nature, 204, 64.

Alissandrakis, C.E. and Kundu, M.R. 1975, Solar Phys., 41, 119.

Anderson, J.A. and Mahoney, M.A. 1974, Solar Phys., 32, 419.

Anderson, K.A. and Winckler, J.R. 1962, J.G.R., 67, 4103.

Arnoldy, R.L., Kane, S.R., and Winckler, J.R. 1968, Ap. J., 151, 711.

Bai, T. and Ramaty, R. 1978, Ap. J., 219, 705.

Baum, P.J. and Bratenahl, A. 1976, Solar Phys., 47, 331.

Beigman, I.L., Grineva, Yu.I., Mandel'stam, S.L., Vainstein, L.A., and Zithik, I.A. 1969, Solar Phys., 9, 160.

Bekefi, G. 1966, Radiation Processes in Plasmas (New York: J. Wiley and Sons).

Bhatia, V.B. and Tandon, J.N. 1970, Ap. Letters, 6, 113.

Böhme, A., Fürstenberg, F., Hildebrandt, J., Saal, C., Krüger, A., Hoyng, P., and Stevens, G.A. 1977, Solar Phys., 53, 139.

Brown, J.C. 1971, Solar Phys., 18, 489.

_____ 1972, Solar Phys., 26, 441.

_____ 1973, Solar Phys., 32, 227.

_____ 1974, in Coronal Disturbances, IAU Symposium No.57, ed. G. Newkirk, Jr. (Dordrecht:Reidel), p.395.

_____ 1975, in Solar Gamma-, X-, and EUV Radiation, IAU Symposium No.68, ed. S.R. Kane (Dordrecht:Reidel), p.245.

_____ 1976, Phil.Trans.R.Soc.London A, 281, 473.

Brown, J.C. and Hoyng, P. 1975, Ap. J., 200, 734.

Brown, J.C. and McClymont, A.N. 1975, Solar Phys., 41, 135.

_____ 1976, Solar Phys., 49, 329.

Brown, J.C., Craig, I.J.D., and Karpen, J.T. 1980, scheduled for publication in Solar Physics.

Brown, J.C., Melrose, D.B., and Spicer, D.S. 1979, Ap. J., 228, 592.

Carrington, R. C. 1859, M.N.R.A.S., 20, 13.

Castelli, J.P., Guidice, D.A., Forrest, D.J., and Babcock, K.A. 1974, J. G. R., 79, 889.

Chubb, T.A. 1972, in Solar-Terrestrial Physics/1970: Part I, Ap. and Space Sci. Library, 29, ed. E.R. Dyer (Dordrecht:Reidel), p.99.

Chubb, T.A., Friedman, H., and Kreplin, R.W. 1960, J.G.R., 65, 1831.

Chubb, T.A., Kreplin, R.W., and Friedman, H. 1966, J.G.R., 71, 3611.

Covington, A.E. 1948, Proc. IRE, 36, 454.

_____ 1951, J. Roy. Astron. Soc. Canada, 45, 157.

Crannell, C.J., Frost, K.J., Mätzler, C.M., Ohki, K., and Saba, J.L. 1978, Ap. J., 223, 620.

Crannell, C.J., Kurz, R.J., and Viehmann, W. 1974, Nucl. Instr. and Meth., 115, 253.

de Feiter, L.D. 1975, in Solar Gamma-, X-, and EUV Radiation, IAU Symposium No.68, ed. S.R. Kane (Dordrecht:Reidel), p.283.

de Feiter, L.D. 1974, Space Sci. Rev., 16, 3.

de Jager, C. 1969, in Solar Flares and Space Research, ed. C. de Jager and Z. Svestka (Amsterdam: North Holland), p. 1.

de Jager, C. and de Jonge, G. 1978, Solar Phys., 58, 127.

de Jager, C. and Kundu, M.R. 1963, Space Res., 3, 836.

Dennis, B.R., Suri, A.N., and Frost, K.J. 1973, Ap. J., 186, 97.

Doschek, G.A. and Feldman, U. 1979, NRL Report No. 8307 (Washington, D.C.: Naval Research Laboratory).

Drummond, W.E. and Rosenbluth, M.N. 1963, Phys. Fluids, 6, 276.

Dulk, G.A., Melrose, D.B., and White, S.M. 1979, Ap. J., 234, 1137.

Elcan, M.J. 1978, Ap. J. Letters, 226, L99.

Elwert, G. and Haug, E. 1970, Solar Phys., 15, 234.

Emslie, A.G., McCaig, M.G. and Brown, J.C. 1979, preprint.

Frost, K.J. 1964, in AAS-NASA Symposium on the Physics of Solar Flares, ed. W.N. Hess (NASA SP 50), p. 139.

_____ 1969, Ap. J. Letters, 158, L159.

Frost, K.J. and Dennis, B.R. 1971, Ap. J., 165, 655.

Frost, K.J., Dennis, B.R., and Lencho, R.J. 1971, in New Techniques in Space Astronomy, ed. F. Labuhn and R. Lüst (Dordrecht: Reidel), p. 185.

Ginzburg, V.L. and Syrovatskii, S.I. 1965, Ann. Rev. Astron. Ap., 3, 297.

Goodman, N.B. 1976, Space Sci. Instr., 2, 425.

Gordon, I.M. 1960, Soviet Astron.-A.J., 4, 874.

Gorenstein, P., Gursky, H., and Garmire, G., 1968, Ap. J., 153, 885.

Guidice, D.A. and Castelli, J.P. 1975, Solar Phys., 44, 155.

Guseinov, R.E. 1963, Soviet Astron.-A.J., 7, 444.

Hachenberg, O. 1959, Rendiconti S.I.F., 12, 245.

Hachenberg, O. and Wallis, Z. 1961, Z. Ap., 52, 42.

Hagen, J.P. and Neidig, D.F. 1971, Solar Phys., 18, 305.

Harvey, K.L. and Harvey, J.W. 1976, Solar Phys., 47, 233.

Harvey, K.L., Martin, S.F., and Riddle, A.C. 1974, Solar Phys., 36, 151.

Haug, E. 1972, Solar Phys., 25, 425.

Hirshfield, J.L. and Brown, S.C. 1961, Phys. Rev., 122, 719.

Hirshfield, J.L., Baldwin, D.E., and Brown, S.C. 1961, Phys. Fluids, 4, 198.

Hobbs, A.W., Jordan, S.D., Maran, S., Caulk, H.M., and Webster, W.J. 1973, Ap. Letters, 15, 193.

Hodgson, R. 1859, M.N.R.A.S., 20, 15.

Holt, S.S. and Ramaty, R. 1969, Solar Phys., 8, 119.

Howard, R. and Babcock, H.W. 1960, Ap. J., 132, 218.

Howard, R. and Severny, A. 1962, Ap. J., 137, 1242.

Hoyng, P. 1975, Ph. D. thesis (University of Utrecht).

Hoyng, P., Brown, J.C., and van Beek, H.F. 1976, Solar Phys., 48, 197.

Hudson, H.S. 1972, Solar Phys., 24, 414.

_____ 1973, in High-Energy Phenomena on the Sun, ed. R. Ramaty and R.G. Stone (NASA SP-342), p.207.

_____ 1978, Ap. J., 224, 235.

Hurford, G.J. 1977, in X-ray Imaging, SPIE Vol. 106, p. 163.

Jackson, J.D. 1962, Classical Electrodynamics (New York: J. Wiley and Sons).

Kane, S.R. 1974, in Coronal Disturbances, IAU Symposium No.57, ed. G. Newkirk, Jr. (Dordrecht: Reidel), p. 105.

Kane, S.R. and Anderson, K.A. 1970, Ap. J., 162, 1003.

Kane, S.R., and Donnelly, R.F. 1971, Ap. J., 164, 151.

Kane, S.R., Anderson, K.A., Evans, W.D., Klebesadel, R.W., and Laros, J.G. 1980, preprint.

Karzas, W. and Latter, R. 1961, Ap. J. Suppl., 6, 167.

Koch, H.W. and Motz, J.W. 1959, Rev. Mod. Phys., 31, 920.

Korchak, K.K. 1967, Soviet Astron.-A.J., 11, 258.

Kosugi, T. 1980, submitted to Solar Physics (preprint).

Kovalev, V.A. and Korolev, O.S. 1976, Soviet Astron.-A.J., 20, 69.

Krall, N.A. and Trivelpiece, A.W. 1973, Principles of Plasma Physics, (New York: McGraw-Hill).

Kundu, M.R. 1959, Ann. d'Astrophys., 22, 1.

_____ 1961, J.G.R., 66, 4308.

_____ 1965, Solar Radio Astronomy (New York: Interscience).

Kundu, M.R. and Vlahos, L. 1979, Ap. J., 232, 595.

Langer, S.H. and Petrosian, V. 1977, Ap. J., 215, 666.

Lipa, B. 1978, Solar Phys., 57, 191.

Magun, A. and Mätzler, C. 1973, Solar Phys., 30, 489.

Marsh, K.A., and Hurford, G.J. 1980, BBSO No. 0191 (California Institute of Technology), preprint.

Marsh, K.A., Hurford, G.J., Zirin, H., and Hjellming, R.M. 1980, BBSO No. 0187 (California Institute of Technology), preprint.

Marsh, K.A., Zirin, H., and Hurford, G.J. 1979, Ap. J., 228, 610.

Mätzler, C. 1976, Solar Phys., 48, 117.

_____ 1978, Astron. Ap., 70, 181.

Mätzler, C., Bai, T., Crannell, C.J., and Frost, K.J. 1978, Ap. J., 223, 1058.

Maxwell, A. and Fitzwilliam, J. 1973, Ap. Letters, 13, 237.

McLean, D.J., Sheridan, K.V., Stewart, R.T., and Wild, J.P. 1971, Nature, 234, 140.

Melrose, D.B. and Brown, J.C. 1976, M.N.R.A.S., 176, 15.

Michard, R. 1971, in Solar Magnetic Fields, IAU Symposium No. 43, ed. R. Howard (Dordrecht: Reidel), p. 359.

Moreton, G.E. 1964, in AAS-NASA Symposium on the Physics of Solar Flares, ed. W.N. Hess (NASA SP 50), p. 209.

Peterson, L.E. and Winckler, J.R. 1958, Phys.Rev. Letters, 1, 205.

_____ 1959, J.G.R., 64, 697.

Petrosian, V. 1973, Ap. J., 186, 291.

_____ 1975, Ap. J., 197, 235.

Ramaty, R. 1968, J. G. R., 73, 3573.

_____ 1969, Ap. J., 158, 753.

Ramaty, R. and Lingenfelter, R.E. 1967, J. G. R., 72, 879.

Ramaty, R. and Petrosian, V. 1972, Ap. J., 178, 241.

Report UAG-72, 1979, Energy Release in Solar Flares, Proceedings of the Workshop on Energy Release in Flares, 26 February - 1 March 1979, Cambridge, Massachusetts U.S.A., ed. L.M. Rust and A.G. Emslie (Boulder, CO: U.S. Department of Commerce, NOAA).

Riddle, A.C. 1970, Solar Phys. 13, 448.

Robinson, R.D. 1978, Solar Phys., 60, 383.

Roy, J.-R., and Datlowe, D.W. 1975, Solar Phys., 40, 165.

Rust, D.M. 1976a, Phil.Trans.R.A.S.London,A,281, 427.

_____ 1976b, Solar Phys., 47, 211.

_____ 1977, "Solar Flares", to be published in Solar System Plasma Physics.

Schmahl, E.J. 1973, Austral. Jl. Phys. Suppl., 29, S28.

Schöechlin, W. and Magun, A. 1979, Solar Phys., 64, 349.

Shklovskii, I.S. 1964, Nature, 202, 275.

_____ 1965, Soviet Astron.-A.J., 8, 538.

Schnack, D. and Killeen, J. 1977, UCRL preprint No. 79261.

Severny, A. 1969, in Solar Flares and Space Research, ed. C. de Jager and Z. Svestka (Amsterdam: North Holland), p. 38.

Shukla, P.K. and Singh, K.P. 1972, Physica Scripta, 5, 217.

Slish, V.I. 1963, Nature, 199, 682.

Smerd, S.F. and Dulk, G.A. 1971, in Solar Magnetic Fields, I.A.U. Symposium No. 43, ed. R. Howard (Dordrecht: Reidel), p. 616.

Smith, D.F. 1980, Solar Phys., 66, 135.

Smith, D.F. and Lilliequist, C.G. 1979, Ap. J., 232, 582.

Solar-Geophysical Data, 1969 March-1972 February, Nos. 296-330 (Boulder, CO: U.S. Department of Commerce, NOAA).

Spicer, D.S. 1976, NRL Report No. 8036 (Washington, D.C.: Naval Research Laboratory).

_____ 1977, Solar Phys., 53, 249.

_____ 1978, NRL Memorandum Report, No. 3749.

_____ 1980, scheduled for publication in Solar Physics.

Stein, W.A. and Ney, E.P. 1963, J.G.R., 68, 65.

Stewart, R.T., and Sheridan, K.V. 1970, Solar Phys., 12, 229.

Svestka, Z. 1976, Solar Flares (Dordrecht: Reidel).

Takakura, T. 1959, in Paris Symposium on Radio Astronomy, ed. R.N. Bracewell (Stanford: Stanford University Press), p. 562.

_____ 1960, Pub. Astron. Soc. Japan, 12, 55.

_____ 1967, Solar Phys., 1, 304.

_____ 1972, Solar Phys., 26, 151.

Takakura, T. and Scalise, E. Jr. 1970, Solar Phys., 11, 434.

Tarnstrom, G.L. 1976, Astron. Ap., 49, 31.

_____ 1977, Astron. Ap., 58, 181.

Tucker, W.H. 1975, Radiation Processes in Astrophysics (Cambridge: MIT Press).

Trubnikov, B.A. 1961, Phys. Fluids, 4, 195.

Trulsen, J. and Fejer, J.A. 1970, J. Plasma Phys., 4, 825.

Van Beek, H.F., de Feiter, L.D., and de Jager, C. 1974, Space Res., 14, 447.

Vette, J.I. and Casal, F.G. 1961, Phys.Rev. Letters, 6, 334.

Vlahos, L. 1979, Ph.D. thesis (University of Maryland).

Vlahos, L. and Papadopoulos, K., 1979, Ap. J., 233, 717.

Vorpahl, J.A. 1976, Ap. J., 205, 868.

Wiehl, H. 1979, in preparation.

Wild, J.P. and Hill, E.R. 1971, Australian J. Phys., 24, 43.

Wild, J.P. and Smerd, S.F. 1972, Ann. Rev. Astron. Ap., 10, 159.

Wild, J.P., Smerd, S.F., and Weiss, A.A. 1963, Ann. Rev. Astron. Ap., 1, 291.

Winckler, J.R., May, T.C., and Masley, A.J. 1961, J.G.R., 66, 316.

Zheleznyakov, V.V. 1965, Soviet Astron.-A.J., 9, 73.

Zirin, H. 1978, Solar Phys., 48, 95.

Zirin, H. and Tanaka, K. 1973, Solar Phys., 32, 173.